A Gas Chromatographic Microsystem for Volatile Organic Compounds: Critical Components, Chemometric Algorithms, and a Laboratory Prototype for Workplace Exposure Monitoring

by

Jonathan Bryant-Genevier

A dissertation submitted in partial fulfillment
of the requirements for the degree of
Doctor of Philosophy
(Environmental Health Sciences)
in the University of Michigan
2016

Doctoral Committee:

Professor Edward T. Zellers, Chair
Professor Robert Kennedy
Professor John Meeker
Associate Professor Chuanwu Xi

Dedication

I dedicate this work to my father, who has always encouraged me to remain curious.

Acknowledgements

I would first and foremost like to thank the current and former members of the Zellers research group, as well as the numerous collaborators, who made particular contributions to this work: Dr. Sun Kyu Kim and Dr. Hungwei Chang for their patient training of this author during the field deployment of the SPIRON instrument, Dr. Dave Burris and Jim Resinger for their help and encouragement during the field deployment, Ms. Katharine Beach for fabrication of the Gen-1 devices used in SPIRON and several of the projects presented here, Dr. Lindsay K. Wright and Dr. Chengyi Zhang for preparing the MPN films and coating sensor arrays, Dr. Kee Scholten for his effort and insight in interpreting sensor array chemometric data as well as fabrication of the Gen-2 sensor array devices, Dr. Gustavo Serrano and William Collin for their chromatography expertise and for coating µcolumns, Nicolas Nuñovero for his significant work on the design and implementation of the electronic software and hardware used for all the projects presented here (particularly for the PEMM systems, which would not have been possible without his contributions), Junqi Wang for his tireless efforts in Gen-1.5 PEMM system testing, Dr. Robert Nidetz for fabricating the µPCF and µcolumn devices used in the PEMM systems as well as providing valuable insight into the design of the next-generation PEMM components, Sanketh Buggaveeti for his work optimizing the design of the µPCF heaters, Dr. Katsuo Kurabayashi for providing valuable guidance on the design and fabrication of PEMM devices, and Changhua (Henry) Zhan for fabricating Gen-2 sensor array devices. I would like to thank my committee members and my advisor for their support and patience throughout the course of my time at Michigan; your commentary and insight were instrumental to my scientific training.

I would also like to sincerely thank my friends and family who have supported me (and entertained my curiosity) over the past several years! A special thanks goes out to all the current and former residents of the Pauline house, who certainly helped share the mental and emotional burden of scientific exploration.

This work was supported in part by the Department of Defense, ESTCP Grant ER-200702 through a subcontract with Integrated Science and Technology, Inc.; by the Department of Homeland Security, Science and Technology Directorate Cooperative Agreement No. 06-G-024; by the National Science Foundation Grant ECCS 1128157; and by the National Institute for Occupational Safety and Health (NIOSH) Grant 1-R01-OH-010297. The author was supported by the Training Grant T42-OH008455 from NIOSH. These sponsoring organizations had no role in the design or conduct of this research or in the decision to pursue publication. Devices were fabricated in the Lurie Nanofabrication Facility, a member of the National Nanotechnology Infrastructure Network. The Zellers research group is a member of University of Michigan’s Center for Wireless Integrated MicroSensing and Systems (WIMS2) Environmental Sensing and Systems Thrust.

Table of Contents

LIST OF FIGURES

LIST OF TABLES

Chapter 1

Introduction

1.1 Dissertation Overview

This dissertation describes a series of projects related to the development of a gas chromatographic microsystem for the determination of exposures to mixtures of airborne volatile organic compounds (VOCs). The primary application of this instrument was quantitatively analyze the individual components of complex VOC mixtures typical of workplace exposures. The primary focus is on the design, development and characterization of the Personal Exposure Monitoring Microsystem (PEMM), a portable micro-scale gas chromatograph (μGC), as well as accompanying chemometric algorithms for improving sensitivity and selectivity.

In this chapter, background knowledge relevant to the research presented in this dissertation will be discussed, as well as an overview of the previous μGC system development efforts from the Zellers research group, from which this work drew heavily. The significance of this work will also be presented. Specifically, a review of traditional and portable sampling and analytical methods for volatile organic compounds (VOCs) in the workplace is presented, followed by a showcase of the field testing of the SPIRON μGC to assess vapor intrusion of trichloroethylene (TCE) in homes near Hill Air Force Base (AFB). Next, a series of discussions on the 1) factors affecting preconcentration of VOCs on graphitized carbon adsorbents and the design of micro-scale preconcentrators, 2) the variables governing the performance of gas chromatographic systems, and 3) principles and governing assumptions of bilinear chemometric algorithms, most notably evolving factor analysis (EFA) and alternating least squares (ALS) are presented. Chapter 2 describes research performed in the development and application of a chemometric algorithm employing EFA-ALS to chromatograms from a micro-chemiresistor (μCR) array detector. A significant portion of the work presented in Chapter 2 has been published in the journal *Sensors and Actuators B: Chemical*. Chapter 3 presents research on the characterization and optimization of a micro-fabricated dual adsorbent preconcentration and injection device for use with the Personal Exposure Monitoring Microsystem (PEMM) μGC. This work has been submitted for publication in the *Journal of Chromatography A*. Chapter 4 discusses the design, integration, and validation of the PEMM for analysis of VOCs in the workplace. This work is being prepared for publication.

In summary, this dissertation entails several independent yet interrelated projects directed towards the development of μGC technology for applications in industrial hygiene and exposure assessment.

1.2 Background and significance

1.2.1 Volatile organic compounds and their health effects

The Agency for Toxic Substances and Disease Registry broadly defines volatile organic compounds as a “class of chemicals that evaporate easily and contain carbon atoms.” VOCs are ubiquitous, arising both naturally and anthropogenically, and are constituents in nearly all manufactured products, including solvents, lubricants, inks, constituents for chemical/pharmaceutical manufacturing, fuel, food additives, and cleaning supplies, among many others.[1] However, without proper monitoring and regulation, these substances can have severe consequences, disrupting both the environment and human health.[1-3]

The types and severity of health effects resulting from exposure to VOCs vary widely, from skin and respiratory tract irritation in the case of relatively innocuous compounds such as acetone, to central nervous system impairment, reproductive damage and cancer from more hazardous substances such as trichloroethylene, benzene or methanol.[2-5] Health effects are generally classified as acute or chronic, with hazards resulting from either short term exposures (minutes-hours) or continuous exposure over a prolonged period (months to years), though substances often elicit both. The concentrations (doses) of these compounds that present a risk also varies; occupational exposure limits (OELs) range from the low ppb to the high ppm, spanning roughly 4 orders of magnitude.[6-7] While there may exist several tens of thousands of different VOCs in use today, less than a thousand are currently regulated and/or monitored in the United States.[2-4] Furthermore, the majority of toxicological evidence used to establish OELs is based on exposures to single compounds alone whereas the majority of real-life exposures are to mixtures of compounds; relatively little is understood about how concurrent vapor exposures may change the health outcomes or “at risk” concentrations.[2-4]

1.2.2 Traditional sampling methods

The quantitative assessment of personal exposures to mixtures of airborne volatile organic compounds (VOCs) in working environments remains a particularly challenging problem. Classical sampling and analytical methods entail the collection of breathing-zone air samples, typically over several hours, followed by analysis at an off-site laboratory.[4,6-8] The National Institute for Occupational Safety and Health (NIOSH), the Occupational Safety and

Health Administration (OSHA), and the Environmental Protection Agency are responsible for designing, evaluating and publishing analytical methods for all regulated VOCs, including details of the sampling procedure (adsorbent material, sampling flow rates, duration of sampling), desorption procedure (solvent vs. thermal), and conditions for the downstream analytical instrumentation.[6-8]

The most common route of exposure to VOCs is inhalation; as such, nearly all regulatory/compliance based exposure assessment techniques rely on determining the concentrations of these hazards in the air. Personal samples are collected by passing workplace air in the worker's personal breathing zone (PBZ) through an adsorbent-packed tube designed to exhaustively capture/preconcentrate VOCs in the sample.[2-4] The sampling method (adsorbent material, air volume, duration of sampling) is often dependent on the physical properties of the analyte (vapor pressure, polarity, stability), the nature of the health outcome (acute vs. chronic), the purpose of monitoring (screening vs. compliance), and/or the detection limit of the analytical method used downstream (LODs), ranging from 15 minutes in the case of grab samples or compliance with short term exposure limits (STELs), to 8 hours in the case of full work-shift time weighted averages (TWAs).[6-8]

After sampling, tubes are typically transported off-site for analysis by conventional bench-scale instrumentation, which, in the vast majority of cases, employ gas chromatography (GC) with either flame ionization (FID), electron capture (ECD), or mass spectrometry (MS) detection.[6,7] GC is immensely popular due to its versatility, as well as its ability to separate the components of a mixture in space/time, such that each VOC can be analyzed in a reproducible and consistent manner. Although reliable, these methods are capital and labor intensive and generally provide only long-term (e.g. daily) average measures of exposure. Overall, the inability to elucidate exposure dynamics throughout a work-shift, and the higher cost-per-sample associated with these methods can result in a reduction in the quantity, quality, and frequency of worker exposure data. Performing measurements with a direct reading instrument mounted on the worker could improve the quality of data gathered by capturing exposure dynamics within a work shift.

It is important to note here, however, that one of the classic challenges facing the occupational hygienist/exposure scientist is that in order to select the appropriate method for a given exposure assessment scenario, it is necessary to have a general concept of the composition of the environment, including rough estimates of the anticipated targets and interferences, as well as their concentrations.

1.2.3 Portable analytical instrumentation

VOC analyzers can be classified by their selectivity.[9,10] The first class is the universal or total VOC detectors, which respond indescriminently to all VOCs, providing a general measure of overall quantity. Examples of these include photoionization detectors (PID) such as the handheld MiniRAE 300[11] from RAE Systems and flame ionization detectors (FID) such as the MicroFID II[12] from Inficon, among others. These detectors are universal because their transduction methods (ionization or thermal conductivity for example) respond to all vapors in an air sample in the same manner. While these devices are generally quite accurate for single analytes, they provide little to no selectivity on their own, and are either used in scenarios where such selectivity is unnecessary, or in conjunction with other analytical tools. These analyzers are the lowest cost option, are widely available and quite useful for measuring total VOCs or for leak detection; they do, however, provide the lowest quality data with respect to selectivity.

The second class of VOC analyzers is the partially selective detectors, which are generally capable of distinguishing between groups of compounds, typically by crudely comparing the response patterns, differences in which are dependent on the chemical properties or functional groups of vapors within the samples.[13-19] This class is mostly comprised of sensor arrays, commonly referred to as "electronic noses." These instruments operate via a sort of "machine olfaction" in which multi-dimensional data generated from the array is analyzed by pattern recognition and matching algorithms to differentiate groups of vapors exhibiting a particular "scent." Examples include instruments developed by Alpha MOS (FOX and GEMINI electronic noses), and products from Cyrano Sciences, among others.[18,19] These instruments are often subject to false positives and negatives (i.e. incorrect classification of vapor groups) due to competing interactions from interfering VOCs, which can generate similar responses. As such, these instruments require careful calibration for each specific application prior to use. It is generally accepted that these instruments are incapable of identifying the individual components of a mixture.

The third class of VOC analyzers, of which there are only three types, is the chromatographic and spectrometric systems, which offer sufficient selectivity to accurately quantify the individual components of VOC mixtures. These include infrared spectrophotometry (IR), mass spectrometry (MS), and gas chromatography (GC). IR systems, such as the portable single beam Miran SapphIRe,[20] operate by examining the absorption of infrared light at set wavelengths, a process governed by the chemical functional groups and bond types present in the molecule, allowing for analysis of single components, one at a time, at ppm levels. With portable Fourier transform IR instruments, such as the Gasmet DX4030,[21] entire IR spectrums can be collected within a few seconds, allowing for multiple compounds to be analyzed simultaneously.

However, since the sensitivity of these instruments is dependent on path length, it is difficult to adapt them for ppb-level applications, or shrink the instruments to a wearable size. MS systems ionize analytes and then separate them based on their mass to charge ratios using electromagnetic fields, identifying compounds via their molecular weight and fragmentation pattern, the latter of which is often indicative of molecular structure motifs, by comparison with vast chemical libraries. Since the time necessary to collect a full spectrum depends only on the scan rate of the electromagnets, these instruments are capable of extremely fast analyses. As a stand-alone instrument, MS has been used to analyze complex environmental mixtures, however it can also be coupled with chromatographic methods to achieve even greater selectivity. Examples of portable MS instruments include the Griffin 824 from FLIR, the M908 by 908 devices, and the Mini 10 developed at Purdue University.[11-23] Examples of portable GC-MS instruments include the HAPSITE from Inficon, and the Tridion-9 from Torion.[24,25]

Gas chromatographic techniques, which will be discussed in greater detail in Section 1.8, operate by separating individual compounds in space as they travel through a column, permitting their detection one at a time. The beauty of this technique is its versatility; retention times can be adjusted by changing the composition of the stationary and mobile phases, the length of the separation column, or the temperature of the system. Furthermore, an enormous variety of detectors are amenable to integration with GC. Over the last four decades, significant advances in this technology have been made in the realm of portable GC. Commercial examples of GC field portable instruments include the 3000 MicroGC from Inficon,[26] which uses a micro thermal conductivity detector, and the EW-4400 GC from EWAI, which uses a photoionization detector.[27] The DPS Companion 600 GC and the SRI Model 310 GC each offer several detector choices though require AC power and are significantly larger/heavier than previous examples, and are thus designated as only transportable.[28,29] Field-portable GC-MS instruments, as mentioned above, have also grown in popularity. Unfortunately, the current portable direct-reading VOC-monitoring instruments capable of quantitative multi-VOC determinations, which employ gas chromatographic (GC) separations and/or spectrometric detectors, remain too large, complex, and expensive for routine deployment as personal exposure monitors.

1.2.4 Fundamentals of micro-scale vapor preconcentration

The preconcentrator of a portable system provides the means to trap VOCs from an air sample, often by adsorption on a granular solid, and then to thermally desorb and inject them as a focused band for subsequent separation and detection. The dual nature demanded of this component is reflected in the term “micropreconcentrator-focuser” (μPCF),[32] and the range of μPCF designs, adsorbent materials, and operating features reported over the past decade reflect the challenges to optimizing performance and minimizing power dissipation (see for example, refs. 30-45). Photographs of a subset of these devices are presented in Figure 1.1. In most reported μPCF devices, only a fraction of the mass of any targeted VOC(s) in the air passing through the device is captured and subsequently desorbed for analysis. As with classical solid-phase microextraction (SPME) techniques,[46-47] these devices rely on the equilibrium that can be established between the VOC air concentration and the VOC surface concentration to relate the former to the latter for quantification. Complementing such *equilibrium* dependent μPCFs, another class of devices captures the entire mass of any targeted VOC(s) in the air sample, making the relationship between VOC air concentrations and analyzed quantities of VOCs more direct.[30-32,34,37,39,42,43] Despite their larger size and consequently greater heating power dissipation, these so-called *exhaustive* μPCFs yield much larger preconcentration factors

(PF).[30,31,48,49] In contrast, although sensitivity enhancement is achieved with *equilibrium* μPCF devices,[35,37] since mass is not conserved, bonafide PF values are indeterminate.[45-46]

The design and operation of exhaustive μPCF devices, which may have single-bed or multi-bed adsorbents, are subject to several constraints. A certain minimum sample volume is required to ensure that the mass of analyte(s) collected exceeds the limit of detection (LOD) of the downstream microsensor(s), while the maximum sample volume is constrained by the inherently low capacity of the small quantities and finite surface areas of adsorbent materials used in these micro-scale devices. Flow rate, bed residence time, temperature, ambient water vapor and background VOC concentrations, adsorbent mass and specific surface area, and analyte volatility and functionality are all factors affecting capacity. Many of these same factors also affect the efficiency of thermal desorption and the minimum injection band width achievable. Thus, several aspects of μGC system performance are contingent upon the performance of the μPCF component. The modified Wheeler model, an empirically derived model originally developed to determine the lifetimes of respirator cartridges,[48,49] has been used to relate the factors governing exhaustive preconcentration of VOCs on graphitized carbon adsorbents. The equations for both breakthrough volume in liters (V_b) and breakthrough time (t_b) in minutes are listed below:

$$V_b = \frac{W_e W_b}{C_0}\left[1 - \frac{1}{k_v \tau} ln\left(\frac{C_0}{C_x}\right)\right] \qquad \text{(Eq. 1.1)}$$

$$t_b = \frac{\rho_b W_e}{C_0}\left[\tau - \frac{1}{k_v} ln\left(\frac{C_0}{C_x}\right)\right] \qquad \text{(Eq. 1.2)}$$

where W_e is the adsorption capacity (ratio of adsorbate mass to adsorbent mass, unitless), W_b is the bed mass (g), C_0 is the inlet or sample concentration (upstream of the bed, g/mL), C_x is the outlet or effluent concentration (downstream of the bed, g/mL), ρ_b is the adsorbent bed density (g/mL), k_v is the kinetic rate constant (min^{-1}), and the bed residence time (τ, min) is defined by:

$$\tau = \frac{W_b}{(\rho_b Q)} \qquad \text{(Eq. 1.3)}$$

where Q is the volumetric flow rate (mL/min). The variables W_e and k_v are unique to the compound/analyte in question, W_b and ρ are specific to the preconcentration device, and C_0, C_x and Q are specific to the scenario or conditions of the exposure (for the case of exhaustive preconcentrators, C_x is typically 10% or less of C_0). A diagram of breakthrough of a vapor through a packed adsorbent bed, taken from reference 48, is shown in Figure 1.2. As the sample passes through the bed, vapors in the contaminated air condense onto the adsorbent material, reducing the air concentration of analyte, creating a concentration gradient (dubbed the Adsorption zone in Figure 1.2) or moving "plug." At a certain point, the leading edge of the plug reaches the end of the bed, resulting in breakthrough. Figure 1.3 shows an idealized example breakthrough curve, taken from reference 51, highlighting the breakthrough concentration (as a fraction of the challenge concentration) as a function of time. This figure also highlights several key features of a typical breakthrough curve, including the allowable breakthrough fraction. This model, however, is only applicable to single analyte exposures, where W_e and k_v are constants that can be determined empirically. In the case of mixtures, the equation does not directly apply, however is still useful for understanding the parameters governing breakthrough.

The first term in Equation 1.1, $W_e W_b C_0^{-1}$, is called the absolute equilibrium capacity, with units of mL, and corresponds to the breakthrough volume in the idealized case where the rate constant is infinitely large (i.e. when the second term in brackets approaches unity). The second term, $[1-(1/k_v\tau)ln(C_0/C_x)]$, called the adsorption efficiency, is typically less than unity such that V_b is less than the absolute equilibrium capacity. We can infer from Equation 1.1 that V_b decreases as C_0 increases, as τ decreases, and as W_b decreases. Logically, these relationships make sense; as the challenge concentration increases, the adsorption sites will become saturated sooner. Similarly, as bed residence time decreases (as flow rate increases), the time available to reach equilibrium (for the analytes to find and fill available adsorption sites) necessarily decreases. Lastly, as the mass of adsorbent (and therefore volume of the adsorbent trap) decreases, there are fewer available adsorption sites.

Applying this equation to the performance of micro-scale adsorbent beds has been an on-going focus of the Zellers research group for more than a decade. Using the modified Wheeler model as a guide, Lu and Zellers established relationships between the breakthrough volume (V_b), adsorbent bed mass, bed residence time (τ), and challenge concentration in their studies of small single- and multi-adsorbent capillary-style PCF devices intended for use in portable GC instruments.[26,27] Systematic tests of capacity and desorption bandwidths for individual VOCs and VOC mixtures were performed with a selected set of adsorbents to establish the minimum required adsorbent masses and maximum allowable flow rates for exhaustive trapping and efficient desorption. These studies provided the basis for the adsorbent masses used in the first-generation μPCF devices of the early μGC systems developed in our group (see Section 1.2.5).

Later work by Sukaew, et al., examined in greater detail the relationships between values of V_b and τ of individual VOCs for a series of capillary-style PCFs and next generation μPCFs packed with the graphitized carbon Carbopack X.[43] They showed that below a minimum "safe" bed residence time, τ_{safe}, the dependence of the breakthrough volume on flow rate was extremely sharp and therefore unstable, and they recommended as a generic guideline operating at flow rates that would maintain $\tau > \tau_{\text{safe}}$. In light of such considerations, the operating conditions of μPCF devices for two application-specific μGC systems were carefully established: one designed for the determination of trichloroethylene in homes impacted by vapor intrusion from contaminated groundwater,[39] and the other designed for screening of three specific explosive marker compounds at security checkpoints.[42] The approaches taken to μPCF development and validation in these studies highlighted the importance of both fundamental design issues and application-specific variables in optimizing performance.

There exist numerous co-dependencies within these equations, such as dependence of W_e on C_0 and the relationship between k_v and τ, both of which are beyond the scope of this dissertation. For more information on the details of the Wheeler model, see references 48-52, and the dissertations of former group members Dr. Thitiporn Sukaew and Dr. Chia-Jung Lu.

Chapter 3 of this dissertation describes work performed on the development and characterization of a μPCF for use, ultimately, in the wearable PEMM μGC system, with an emphases on assessing and reconciling the tradeoffs and constraints placed on the μPCF by the nature of the vapor mixtures of interest, the separation efficiency of the μcolumns, and the sensitivities of the microsensor array to be employed, each of which required careful consideration to achieve satisfactory system-level performance.

1.2.5 Principles of gas chromatography

Chromatographic techniques operate by separating individual compounds in space as they travel through a column based on their relative affinities for the stationary phase (in capillary gas chromatography the stationary phase is typically a polymer coating along the interior walls of the separation column). Samples are discretely injected at the front end of the column and are separated as they flow through via differential partitioning. The efficiency of a separation column is defined by *N*, the number of theoretical plates:

$$N = \frac{L}{H} \tag{Eq. 1.4}$$

where *L* is the length of the separation column and *H* is the height equivalent of a theoretical plate, a common metric of column performance.[56,57] *H* can further be described by the van Deemter equation, a form of which specific to capillary partition chromatography is shown below:

$$H = \frac{B}{v} + C_m v + C_S v \tag{Eq. 1.5}$$

where *v* is the linear velocity, and *B* (longitudinal molecular diffusion term), C_m (sorption-desorption term) and C_s (mobile phase diffusion term) are given by:

$$B = 2D_m \tag{Eq. 1.6}$$

$$C_m = \frac{(6R^2 - 16R + 11) r_c^2}{24 D_m} \tag{Eq. 1.7}$$

$$C_S = \frac{qR(1-R)d^2}{D_S} \tag{Eq. 1.8}$$

where D_m is the coefficient for longitudinal diffusion in the mobile phase in units of cm^2/s, *R* is the retention ratio (speed of a zone/band relative to the speed of the mobile phase, unitless), r_c is the radius of the separation column in cm, *q* is the volumetric flow rate in units of mL/sec, *d* is the thickness of the stationary phase in units of cm, and D_s is the coefficient for diffusion in the stationary phase in units of cm^2/s.[53] D_m, rc, q, d and D_s are all column or condition specific variables, i.e. they affect all compounds on a column the same way. R on the other hand is compound specific; each analyte has a slightly different value for R, which effectively permits their separation (note: if R values are identical, then no separation is possible for that stationary phase). The graphical relationship between H and v is represented by the van Deemter plot, shown in Figure 1.4a.

In order to maintain efficient separations, H must be minimized. For very small values of v, the first term, B/v, the longitudinal molecular diffusion term, is large relative to the mass transfer terms. This means that at slow linear velocities, longitudinal (along the length of the column) diffusion is the primary factor governing H.[56,57] For larger values of v, competition between the mass transfer terms, C_m and C_s, will dominate H. [56,57] These trends are evident from Figure 1.4a, which highlights that in order to minimize H, a compromise must be made. D_m is dependent on the viscosity and diffusion rates of the gas used for the mobile phase, again evident from Figure 1.4b, which shows the differing dependencies of H on carrier gas velociites for two common carrier gasses, nitrogen and helium. While nitrogen offers the lowest possible H, this occurs at an extremely small value of v. For higher v, hydrogen and helium are better options as the rate of increase in H is more gradual than for nitrogen due to increases in D_m for these gases. In chapters 3 and 4, the influence of carrier gas and flow (D_m and τ) on chromatographic performance in the context of µGC system development is explored.

The ultimate indicator of chromatographic performance is resolution, defined $R_s = \Delta t_R\ [2*(\sigma_a+\sigma_b)]^{-1}$, where Δt_R is the difference in retention time of two analytes, and σ_a and σ_b are the standard deviations (in time) of the Gaussian peaks of the two analytes.[52,53] In most cases, the peak width and retention time of a given analyte are related; compounds with longer retention times spend more time on column (in the stationary phase), and thus tend to have wider peaks. Effectively, resolution is a measure of the degree of separation between two adjacently eluting analytes, and is dependent on numerous factors beyond the plate count (N) of the column, including the analytes being separated, the injection bandwidth, the temperature of thee separation column, the flow rate, and the detector. As such, resolution can be used to describe the chromatographic performance of a system from a more holistic perspective, instead of focusing simply on the column of that system.

When applying these principles to micro-columns, it is important to take note of a few key practical changes to the introductory theory presented above. Firstly, the vast majority of micro-columns (all those fabricated using dry reactive ion etching, DRIE), have rectangular cross sections, not circular.[58-62] Figure 1.5 shows several notable examples of recently reported µGC columns. Most have a nearly square cross section to mimic the performance of cylindrical fused silica columns, however a variety of other layouts are possible with DRIE, which affect chromatographic performance in different ways.[58] For rectangular cross-section columns, unlike for open tubular columns with circular cross sections, the distances from the center of mass of a moving band to the adjacent column walls are not always identical. As such, resistance to mass transfer in the mobile phase is governed primarily by the smaller of the two rectangular dimensions (shortest diffusion distance). High aspect ratio columns have been investigated in an effort to demonstrate this point, effectively reducing *r* from Equation 1.7 while maintaining sufficient stationary phase thickness *d* from Equation 1.8 to keep column capacity up, in an effort to maintain chromatographic performance at higher volumetric flow rates. For a more thorough discussion of this concept, see G. E. Spangler’s 1998 article, reference #58. Semi packed columns have also been explored as a potential alternative, using DRIE to form pillars in the flow path on which stationary phase is coated.[61] Unfortunately, the rectangular cross-sections created by DRIE often cause the liquid polymers typically used as stationary phases to pool at the corners during coating, resulting in non-uniform stationary phase thicknesses. Alternatives such as monolayer protected gold nanoparticle films have been proposed, however research on these remains inconclusive.[64] Second, due to the limited real-estate on a typical Si wafer, column lengths are limited. In order to fit sufficiently long fluidic channels on a chip, the channels must have sharp turns, which can, in extreme circumstances, disrupt the laminar flow through the channel and hamper chromatographic performance.[60] The radius of curvature of a turn and the number of turns in a column are additional factors that require attention when designing micro-columns.

It is important to note here that these variables only describe the factors arising only from the separation columns, and do not consider sources of extra-column band broadening, i.e. factors from other fluidic compounds contributing to reduced chromatographic performance, a necessary consideration in the design of full chromatographic systems. The injection source, detector, and fluidic transfer lines of a system all contribute, to various extents, to reductions in chromatographic efficiency (increases in band broadening), each sharing a different relationship with linear velocity through the system. Determining the precise contributions of band broadening can be quite difficult. Extra-column band broadening is typically evaluated empirically by removing the column from the chromatographic system, and measuring the bandwidth of components using the remaining fluidic components of the system. Details of characterizing extra-column band broadening and chromatographic performance at the system level will be discussed in Chapters 3 and 4.

The versatility of gas chromatography is due to the fact that retention times can be adjusted by changing the composition of the stationary and/or mobile phases, the length of the separation column, or the temperature of the system (which affects R), which can theoretically introduce analytes one at a time. Gas chromatography is also amenable to miniaturization, as several of the parameters controlling separation efficiency favor narrower flow paths and thinner stationary phases (H is proportional to r_c and d, thus as columns shrink in diameter and reduce their stationary phase thickness, H decreases). Furthermore, the versatility and design freedom possible with micro-fabrication allows for tailored, application specific separation columns to be made to fit the needs of a specific user.

1.2.6 Bilinear chemometrics

Bilinear chemometric methods are commonly used to analyze data from hybrid chromatographic or spectrometric methods of complex mixtures to improve selectivity, especially in cases where the signals of individual components overlap. These methods also offer a more refined alternative to the analysis overlapping peaks in GC-microsensor array data, where the crude spectra provided by the arrays provide the second dimension to the data.[13-17,19] The goal of chemometrics is to provide a means of distinguishing individual chemical signatures from overlapping composite signals generated from hyphenated or multidimensional methods, such as GC×MS or GC×GC, through the use of the information from both the affinity based separations of chromatographic methods with the structure based identification of spectrometric methods. Sensor arrays, by contrast, generate much lower dimensionality data than spectrometric detectors, however have been used to differentiate components of binary and ternary mixtures by employing simple linear chemometric algorithms such as principal component analysis (PCA) and extended disjoint principal component regression (EDPCR).[13-17,67-71] These algorithms are used to determine the composition of an unknown composite signal through linear combinations of known individual signals, however do not make full use the time-resolved chromatographic portion of the data, relying instead solely on response patterns.

Multivariate curve resolution methods take this concept a step further by taking full advantage of the bilinear data, specifically the additional information provided by the time (or mass/charge ratio in the case of MS data) resolution. These methods can be used to determine the number of components in overlapped chromatographic peak composites and to then extract the spectrum and concentration/elution profile of each component without prior knowledge of the mixture composition.[71-76] Extracted spectra can be matched to those in a library to aid in the identification of the individual analytes, beyond simple retention times, and the recovered profiles can yield the mass or concentration by reference to calibration data. Methods have been developed for a wide variety of hybrid instrumentation techniques; examples of the algorithms applied to data from hyphenated chromatographic-spectrometric systems include evolving factor analysis (EFA)[71,72,74,75], SIMPLISMA,[79] PARAFAC,[780] alternating least squares (ALS)[76-78,82-85], and derivatives or combinations thereof.[73,85] The topic has been the subject of a recent review.[86]

In EFA, singular value decompositions are performed progressively over sequential time segments of a composite peak profile, in both forward and reverse directions. Assuming that sufficient spectrometric discrimination of the partially resolved peak components is provided by the detector and that the responses from the components add linearly, then the rank of the data matrix should equal the number of analytes in the composite peak.[71,72] By following EFA with ALS, iterative refinements are made to the initially extracted elution profiles and spectra to improve accuracy and efficiency.[73] It is also common to incorporate *a priori* problem-specific information in ALS to constrain the calculation and thereby further reduce the error in the final solution.[74,84]

Chemometric algorithms offer the potential to solve a fundamental problem of many portable GC or μGC systems: the poor resolution of short separation columns typically used in such systems. By incorporating sensor arrays whose response pattern to a vapor phase analyte is analogous to a spectrum, these instruments effectively become multidimensional, allowing for the use of chemometrics to improve selectivity. The primary difference between this and conventional hyphenated techniques is the amount of independent information about the analytes that can be derived from the detector output, which is much less for a microsensor array than for a spectrometer; when operated alone, the composite pattern of responses from a mixture of three or more vapors typically cannot be reliably differentiated from those of the individual components or their lower-order mixtures using sensors of this type.[88]

Mathematically, the raw chromatographic data matrix Y, which consists of the collection of responses from each sensor (columns) at each value of time (rows), can be decomposed as follows:

$$Y = CS + E \qquad \text{(Eq. 1.9)}$$

where C is the concentration matrix, the rows of which are the points in time and the columns of which are the concentrations of each component, and S is the sensor sensitivity matrix, the rows of which are the sensitivity pattern of the eluting components and the columns of which are the sensors in the array.[87] An example deconvolution is shown in Figure 1.5. To remove the influence of concentration, sensitivity patterns can be normalized (e.g., by constraining the range of sensitivities from 0 to 1). Residual errors are relegated to the error matrix *E*.

Initial estimates of *C* and *S* are generated by EFA, which assumes that there are selective elution regions of each component, such that the first peak to start eluting is also the first peak to finish eluting. These estimates are subsequently refined using ALS, which employs the following iterative calculations, given *Y***:**

$$C = YS'(SS')^{-1} \tag{Eq. 1.10}$$

$$S' = (C'C)^{-1}C'Y \tag{Eq. 1.11}$$

Equation 1.10 is the least squares solution of eq. 1.9 with respect to *C*, assuming that *S* is known, and Equation 1.11 is the least squares solution of the same equation assuming ***C*** is known. In practice, neither *C* nor *S* is known *a priori*, but by iterating between eq. 2 and 3, starting from the initial estimates of *C* and *S* generated by EFA, one approaches an optimized solution for *Y*. Optimization can be facilitated by applying constraints, such as non-negativity (all values must be greater than zero) and unimodality (concentration profiles can only have one maxima), or by substituting calibration responses for EFA estimates, in situations where it is justified.[74] The ALS algorithm stops iteration at a preset convergence in the residual error matrix *E*.

In a previous study from our laboratory, the application of EFA-ALS to *simulated data* from an array of microsensors used as the detector in a GC was explored.[87] Using sensitivities from an array of 4 chemiresistors coated with thiolate-monolayer-protected Au nanoparticles (MPNs) having different thiolate functionalities, Monte Carlo simulations were used to investigate whether EFA-ALS could detect and then recover the response patterns of the peak components from binary composites with high fidelity. Although experimental sensitivity values were employed, the overlaps and relative responses were simulated assuming idealized Gaussian peaks, and the (5%) random error superimposed on the sensor responses was also assumed to be Gaussian for the Monte Carlo simulations. Overall, the performance of the method and the array was quite good for the synthetic cases considered. Quantification accuracy was not explored.

Chapter 2 presents the results of a study conducted to evaluate the performance of such a hybrid EFA-ALS curve resolution algorithm with *experimental data* from a chemiresistor sensor array used as a μGC detector. Using the framework of the previous study from our laboratory,[87] the capability to determine the number of components (i.e., the chemical rank) in each composite peak and to extract the pattern and concentration of each component is evaluated over a range of chromatographic resolution and relative response ratio values for pairs of vapors with different (Pearson) correlation coefficients.

1.2.7 Micro-analytical systems for VOC monitoring

In attempts to address some of the shortcomings of conventional portable GC instrumentation, a significant amount of research over the past four decades has been devoted to developing GC microsystems (μGC) constructed from Si-microfabricated components, with steady progress being made toward smaller packages with lower power dissipation and greater analytical capabilities.[88-109] This technology offers the potential advantages of smaller overall system footprints, integrated on-chip fluidics, and low power operation in comparison with their conventional portable GC counterparts. The earliest progenitors of this technology were the members of Professor James Angell’s research group at Stanford University, who began this work in the late 1970s. Considered by many to be the father of silicon micromachining, Angell, along with one of his graduate students Stephen Terry and Hal Jermann, built the first μGC, which included a loop injector, a separation column, and a micro-thermal conductivity detector all integrated on a single 2-inch Si wafer.[89] Since then, numerous examples of microelectromechanical (MEMS) μGC components and systems have been reported, primarily from current and/or former researchers from: Stanford University (e.g. Dr. Kensall Wise),[89,93] the University of Michigan's Center for Wireless Integrated MicroSystems (e.g. Dr. Richard Sacks, Dr. Yogesh Gianchandani, Dr. Edward Zellers, Dr. Katuso Kurabayashi, Dr. Sherman Fan, Dr. Masoud Agah -now at Virginia Tech University),[91,93,97-100,105,106] Sandia National Laboratories (e.g. Dr. Gregory Frye-Mason, Dr. Ronald Manginell, Dr. Patrick Lewis),[91,94] the University of Catania's Institute for Microelectronics and Microsystems (e.g. Dr. Stefano Zampolli, Dr. Ivan Elmi),[96] the University of Illinois at Urbana-Champaign (e.g. Dr. Richard Masel and Dr. Mark Shannon) and the Louisiana Tech University (e.g. Dr. Edward Overton, Dr. Adarsh Radadia).[61,62] Each of these groups has focused on somewhat different aspects of μGC development, from optimizing individual components, to exploring novel fabrication and design features, and to full system integration.

Most μGC systems contain a micropreconcentrator or other on-board injection device, one or more separation microcolumns, and a microsensor or microsensor array detector, along with the necessary auxiliary hardware and software for stand-alone or computer-controlled operation. A plethora of microfabricated detectors amenable to incorporation into μGC systems have also been developed under this umbrella, including surface acoustic wave devices,[111] metal oxide semiconductors,[112] chemiresistors,[113,114] photoionization detectors,[115] and quartz crystal microbalances.[116] A few examples of commercial instruments employing microfabricated components (often erroneously called “µGCs,” a term reserved for instruments with all microfabricated fluidic components) have also appeared on the market, including the GCM 5000 from SLS Micro-Technology,[106] the TOCAM from Defiant Technologies,[109] the GCAP from APIX Analytics (currently under development, not yet on the market),[110] and the 3000 Micro GC/Fusion from Inficon.[26] However, these instruments have not been designed with personalized real-time exposure assessment in mind, and none of them are of wearable size.

1.2.8 SPIRON µGC

Much of the foundation for the research presented here was the result of prior work in our laboratory on the development of SPIRON, a complete field-deployable µGC designed to assess low- to sub-ppb concentrations of TCE in vapor-intrusion[1] impacted homes. The instrument included a pre-trap and partially selective high-volume sampler of conventional design for selective preconcentration, a micromachined-Si focuser for injection, dual 3-m micromachined-Si columns for separation, and an integrated array of four microscale chemiresistors (µCR) with thiolated gold nanoparticle (MPN) interface films for multichannel detection.[98-100] Scrubbed ambient air was used as the carrier gas. Figure 1.6 shows a block diagram of the fluidic system and photograph of the instrument, taken from reference 98. Figure 1.7 shows a cartoon diagram of the MPN coated µCR used in this system. The µCR operates by measuring changes in the resistance of the MPN film induced by reversible absorption of vapors, which cause the film to swell (Figure 1.7d). Responses are rapid, and sensitivities are governed by the strength of intermolecular attraction between vapors and the MPN film. Selectivity is achieved by probing a variety of intermolecular interactive forces (e.g. van der Waals, dipole-dipole, Lewis acid/base

---

[1] Vapor-intrusion is a phenomena whereby volatile pollutants from contaminated ground water evaporate up through the foundations of buildings, presenting an exposure hazard to residents.

interactions, etc…) through the use of different MPN sensor coatings with a variety of functional groups. A list of the MPN coatings used in this research is presented in Figure 1.7c.

As part of the field characterization, the system was brought to a house located near Hill AFB, above a contaminated ground water plume. Over the course of several weeks, concentrations of TCE arising from either vapor intrusion from the contaminated ground water or point sources intentionally placed within the house were monitored in the presence of normal indoor air contaminants. Field-generated calibration curves were linear for injected TCE masses of 26−414 ng (4.8−77 ppb·L) and the projected single sensor detection limit was 0.052 ppb for an 8-L air sample collected and analyzed in 20 min.[98,99] The two prototypes tested had consistent performance and good medium-term stability. Above the mitigation action level (MAL) of 2.3 ppb for the field-test site, μGC TCE determinations fell within ±25% of those from the reference method for 21 of 26 measurements, in the presence of up to 37 documented background VOCs.[98,99] Below the MAL, positive biases were consistently observed, which were attributable to background VOCs that were unresolvable chromatographically or by analysis of the sensor-array response patterns. Overall, results from the study demonstrated that this type of μGC instrument could serve the need for routine TCE determinations in VI-related assessment and mitigation efforts. Other studies, such as that conducted by Zampolli et. al. (reference #96) and Jian et. al. (reference #103), have also demonstrated the successful field deployment of μGC prototypes for other environmental applications.

Several key design issues unique to μGC were uncovered during this project. First, due to the extraordinarily low concentrations encountered (typical of IAQ applications), a large conventional high-volume sampler was required to exhaustively preconcentrate TCE from the 8-20 L air samples necessary to capture sufficient mass for CR array detection.[37] This system component required large amounts of power to heat. However, it was hypothesized that in occupational settings, where exposure concentrations are typically several orders of magnitude higher, a single micro-fabricated component could serve as both a sampling and injection device, greatly reducing the power demand and size of the system, opening the door to personal exposure monitoring.

Second, interfering vapors often co-eluted with the target VOC, reducing the accuracy of both identification and quantification. Several potential solutions beyond simply increasing the length of the separation column (which would require increasing the length of the separation columns, and therefore the size and power demand of the system as well as the time per analysis) were suggested to improve the chromatographic performance: 1) given the response patterns generated by the sensor array, it was hypothesized that a chemometrics algorithm could provide a means of improving resolution and quantification accuracy, and 2) reducing the injection bandwidth of the µPCF could reduce the degree of extra column band broadening in the system, increasing the chromatographic efficiency.

Thirdly, from a system integration/engineering point of view, numerous issues were raised: 1) careful monitoring and control of the instrument’s internal temperature was vital to achieving reproducible identification and quantification, as thermal fluctuations resulted in drifting sensor baselines, changes in CR sensitivity, and inconsistent temperature programs caused variations in retention times, 2) poor system layout caused excessive physical strain on the fluidic devices and their interconnecting capillary, resulting in frequent device failures, and 3) un-optimized electronic circuitry for processing µCR signals reduced the sensitivity, dynamic range, and reproducibility of the arrays.

1.2.9 Personal exposure monitoring microsystem (PEMM) μGC

One of the broad goals of this dissertation is to develop a wearable μGC for near-real-time analysis of VOCs typically found in occupational exposure scenarios. This system, whose architecture is based on that of SPIRON, is designed to operate autonomously (i.e. with embedded control rather than laptop control, and be battery powered), permitting identification and quantification of individual components of moderately complex vapor mixtures every 8-10 minutes. Chapter 4 of this dissertation describes the development of the AC-powered laptop-operated laboratory prototype, dubbed the Gen-1.5 PEMM, which employs a combination of SPIRON (Gen1) μcolumns and novel PEMM μPCF (from results of Chapter 3) and μCR. This project is to be followed by the development of the aforementioned pre-commercial battery-powered micro-controller operated field prototype, dubbed the Gen-2 PEMM, employing the same μPCF and μCR, but with a new single chip 6-m μcolumn. A block diagram of the Gen-1.5 PEMM fluidic layout is presented in Figure 1.7. The primary analytical/fluidic components were fabricated on discrete Si chips and consist of a dual-cavity (dual-adsorbent) μPCF, two series-coupled separation μcolumns (each 3 m long, similar to those described in Section 1.2.5), and an integrated array of chemiresistor μsensors. Commercial valves and pumps are used along with a carrier gas of helium from an on-board canister. A section of PDMS-coated mega-bore capillary positioned at the inlet is used as a pre-trap to remove low-volatility interferences. Again, unlike the SPIRON instrument, the PEMM has no high-volume sampler module. In operation, the on-board mini-pump would draw an air sample of a pre-set volume through the pre-trap and μPCF so that VOCs in the specified p_v range would be captured on the μPCF. Then, the appropriate valves would be thrown, passing carrier gas through the μPCF as it is rapidly, resistively heated to backflush the desorbed VOCs in a focused injection plug to the head of the first μcolumn for temperature-programmed separation, followed by subsequent identification and quantification by the CR array.

This project is a collaborative effort between the Zellers and Kurabayashi research groups, and VGC Chromatography, a commercial partner responsible for assembling the Gen-2 PEMM prototypes based on jointly determined specifications. The author of this dissertation has been the primary graduate student researcher on the development of the Gen-1.5 instrument, tasked with evaluating the fluidic performance of the preconcentrator/focuser (described in Chapter 3) as well as optimizing the fully integrated and operational system (described in Chapter 4). The purpose of development and characterization of Gen-1.5 PEMM is to optimize the performance of the fluidic system holistically, whereby components are examined individually and in concert with one another with the focus lying on system integration (a unique approach to μGC system development) prior to development of the pre-commercial Gen-2 PEMM.

To date, there has been no portable or micro-scale GC suitable for routine and continuous personal exposure monitoring, either due to a lack of performance capabilities or to prohibitive size. Furthermore, because the current analytical methods for demonstrating compliance with established exposure regulations (see Section 1.1.2) rely on traditional instrumentation, micro-scale instrumentation has not yet been adopted on a large commercial scale. The intricacies and difficulties inherent in developing micro-scale instrumentation suitable for analyzing diverse ranges of complex analyte mixtures remain significant unmet challenges.

Figure 1.8 shows a set of chromatograms for a 14-VOC mixture, using the micro-components of the SPIRON field prototype with scrubbed ambient air as the carrier gas, generated as a proof of concept for the PEMM system. Each trace is labeled with the acronym used for the MPN coating material used on the sensor. Headspace samples were loaded onto a SPIRON µPCF via a tee union fitting with a septum port, mimicking the operational conditions of the PEMM system in which the µPCF also acts as the sampling device. The flow direction was then reversed and the µPCF heated to inject the mixture into the µcolumns. The µcolumns were individually ramped from 25 and 30 to 80 and 85 ^{0}C, respectively, at different rates over the course of 3 min. The peaks correspond to masses of analyte ranging from 0.04 to 1 µg, for the least to most volatile compounds in the mixture, respectively. Based on conservative estimates, from a sampling volume of 20 mL, this this corresponds to individual LODs ranging from 2.1 (cumene) to 68 (hexane) ppb. The LOD for benzene is 2.2 ppb. Although most of the peaks are at least partially resolved chromatographically, and the separation is complete within 2.5 min, the peaks are quite broad, with full-width-at-half-maximum (FWHM) values ranging from 1.8 to 4.3 sec. Since real-world environments would have interferences present that need to be resolved from these targets, the peaks need to be much sharper in the ultimate instrument.

In order to improve upon the performance of the SPIRON system, the PEMM will incorporate a number of revisions to the devices, architecture, software and hardware. The system will employ a stacked architecture, with the manifold and electronic boards located beneath the fluidic components. This will improve ventilation in the system and permit more effect cooling of the fluidic components. Fluidic micro-components will be redesigned for lower-power, faster heating ramps to permit sharper injection pulses and greater control over temperature programming. A multi-mode injection system will be incorporated to provide optional split-injection for further reductions in injection bandwidth. The 6-m PEMM µcolumns will be divided into 3 independently heated 2-m segments, all integrated onto a single wafer to reduce cold-spots from interconnections. Helium from a small on-board canister will be used as the carrier gas to improve chromatographic performance. Alternative materials will be explored for the manifold to reduce the weight of the system without compromising the inertness of the fluidic pathways.

1.3 References

[1] An Introduction to Indoor Air Quality Volatile Organic Compounds, Environmental Protection Agency, available at http://www.epa.gov/iaq/voc.html, (accessed July 2015).

[2] J. S. Ignatio, W. H. Bullock, Eds., *A Strategy for Assessing and Managing Occupational Exposures*, 3rd Ed., AIHA Press, Fairfield, VA, 2006.

[3] J. L. Perkins, Modern Industrial Hygiene - Vol. 1. Recognition and Evaluation of Chemical Agents, 2nd Ed., ACGIH, Cincinnati, OH, 2008.

[4] D. H. Anna, Ed., *The Occupational Environment: Its Evaluation, Control, and Management*, 3rd Ed., Vol. 1, AIHA, Fairfax VA, 2011.

[5] ACGIH, Threshold Limit Values for Chemical Substances and Physical Agents & Biological Exposure Indices for 2015, ACGIH, Cincinnati, OH, 2015.

[6] National Institute for Occupational Safety and Health, *NIOSH Manual of Analytical Methods*, http://www.cdc.gov/niosh/docs/2003-154/ (accessed May 2015).

[7] Occupational Safety and Health Administration, *Sampling and Analytical Methods*, https://www.osha.gov/dts/sltc/methods/ (accessed May 2015).

[8] Environmental Protection Agency, *Index to EPA Test Methods*, http://www.epa.gov/region1/info/testmethods/pdfs/testmeth.pdf (accessed August 2015)

[9] D. A. Skoog, F. J. Holler, S. R. Crouch, *Principles of Instrumental Analysis*, 6th Ed., Thomson Brooks/Cole, Belmont CA, 2007.

[10] D. C. Harris, *Quantitative Chemical Analysis*, 6th Ed., W.H. Freeman and Company, New York NY, 2003.

[11] MiniRAE 3000, RAE Systems, available at http://www.raesystems.com/products/minirae-3000, (accessed May 2015).

[12] MicroFID II Portable flame ionization detector, Inficon Technologies, available at http://products.inficon.com/en-us/nav-products/Product/Detail/MicroFID-II-Portable-Flame-Ionization-Detector?path=Products%2Fpg-ChemicalDetection, accessed July 2015.

[13] C. Jin, P. Kurzawski, A. Hierlemann, E. T. Zellers, Evaluation of multitransducer arrays for the determination of organic vapor mixtures, *Anal. Chem.* 80 (2008) 227-236.

[14] J. Park, W. A. Groves, E. T. Zellers, Vapor recognition with small arrays of polymer-coated microsensors: a comprehensive analysis, *Anal. Chem*. 71 (1999) 3877-3886.

[15] M. D. Hsieh, E. T. Zellers, Limits of recognition for simple vapor mixtures determined with a microsensor array, *Anal. Chem.* 76 (2004) 1885-1895.

[16] M. D. Hsieh, E. T. Zellers, Adaptation and evaluation of a personal electronic nose for selective multivapor analysis, *J. Occup. Environ. Hyg.* 1 (2004) 149-160.

[17] M. Li, E.B. Myers, H.X. Tang, S.J. Aldridge, H.C. McCaig, J. J. Whiting, R. J. Simonson, N. S. Lewis, M. L. Roukes, Nanoelectromechanical resonator arrays for ultrafast, gas-phase chromatographic chemical analysis, *Nano Lett.* 10 (2010) 3899-903.

[18] FOX and GEMINI Electronic Noses, Alpha M.O.S., available at http://www.alpha-mos.com/analytical-instruments/fox-gemini-electronic-noses.php (accessed August 2015)

[19] M. D. Woodka, B. S. Brunschwig, N. S. Lewis, Use of spatiotemporal response information from sorption-based sensor arrays to identify and quantify the composition of analyte mixtures, *Langmuir*, 23, 13232-13241, 2007.

[20] MIRAN SapphIRe Portable Analyzer, Thermo Scientific, available at http://www.thermoscientific.com/content/tfs/en/product/miran-sapphire-portable-ambient-analyzers-1.html, (accessed July 2015).

[21] Gasmet DX4040, Gasmet Technologies, available at http://www.gasmet.com/products/portable-gas-analyzers (accessed May 2015).

[22] Griffin 824, FLIR, available at http://www.flir.com/threatDetection/ display/?id=63268, (accessed August 2015)

[23] M908, 908 Devices, available at http://908devices.com/products/, (accessed July 2015).

[24] HAPSITE ER, Inficon, available at http://products.inficon.com/en-us/nav-products (accessed May 2015).

[25] Tridion™-9 GC-MS, Torion, available at http://www.torion.com/products (accessed May 2015).

[26] 3000 Micro GC Gas Analyzer, Inficon, available at http://products.inficon.com/en-us/nav-products/Product/Detail/3000-Micro-GC-Gas-Analyzer?path=Products%2Fpg-ChemicalDetection (accessed July 2015).

[27] EW-4400 Portable Photoionization Gas Chromatograph, EWAI, available at http://www.ewai-group.com/index.php?m=content&c=index&a=show&catid, (accessed July 2015).

[28] DPS Companion 600 GC, DPS Instruments, available at http://www.dps-instruments.com/DPS%20Companion%201%20Brochure.pdf (accessed July 2015).

[29] Model 310 Gas Chromatograph, SRI instruments, available at http://www.srigc.com/2005catalog/cat41.htm, (accessed July 2015).

[30] C-J Lu, E. T. Zellers, A dual-adsorbent preconcentrator for a portable indoor-VOC microsensor system *Anal. Chem.*, 73, 3449-3457, 2001.

[31] C-J. Lu, E. T. Zellers, Multi-adsorbent preconcentration/focusing module for portable-GC/microsensor-array analysis of complex vapor mixtures, *Analyst*, 127, 1061-10I change68, 2002.

[32] W-C. Tian, S. Pang, C-J Lu, E. T. Zellers, Microfabricated preconcentrator-focuser for a microscale gas chromatograph, *J. Microelectromech. Syst.*, 12, 264-272, 2003.

[33] W-C. Tian, H. K. L. Chan, C-J. Lu, S. W. Pang, E. T. Zellers, Microfabricated multi-stage preconcentrator-focuser for a micro gas chromatograph, *J. Microelectromech. Syst.*, 14, 498-507, 2005.

[34] M. Kim, S. Mitra A microfabricated microconcentrator for sensors and gas chromatography *J. Chrom. A*, 996, 1-11, 2003.

[35] R. P. Manginell, D. Adkins, M. W. Moorman, R. Hadizadeh, D. Copic, D. A. Porter, J. M. Anderson, V. M. Hietala, J. R. Bryan, D. R. Wheeler, K. B. Pfeifer, A. Rumpf, Mass sensitive microfabricated chemical preconcentrator *J. Microelectromech. Syst.*, 17 (6), 1396-1407, 2008.

[36] C. M. Hussain, C. Saridara, S. Mitra, Carbon nanotubes as sorbents for the gas phase preconcentration of semivolatile organics in a microtrap *Analyst*, 133, 1076-1082, 2008.

[37] Gracia, P. Ivanov, F. Blanco, N. Sabate, X. Vilanova, X. Correig, L. Fonseca, E. Figueras, J. Santander, C. Cane Sub-ppm gas sensor detection via spiral µ-preconcentrator *Sens. Actuator, B: Chemical*, 132, 149-154, 2008.

[38] B. Alfeeli, M. Agah, MEMS-based selective preconcentration of trace level breath analytes *IEEE Sensors J.,* 9, 1068-1075, 2009.

[39] T. Sukaew, H. Chang, G. Serrano, E. T. Zellers, Multi-stage preconcentrator/focuser module designed to enable trace level determinations of trichloroethylene in indoor air with a microfabricated gas chromatograph *Analyst*, 136, 1664-1674, 2011.

[40] W-C. Tian, T. H. Wu, C-J Lu, W. R. Chen, H. J. Sheen, A novel micropreconcentrator employing a laminar flow patterned heater for micro gas chromatography *J. Microelectromech. Syst.*, 22 (6), 1-8, 2012.

[41] M. Y. Wong, W. R. Cheng, M. H. Liu, W. C. Tian, C. J. Lu, A preconcentrator chip employing μSPME array coated with in-situ-synthesized carbon adsorbent film for VOCs analysis, *Talanta*, 101, 307-313, 2012.

[42] G. Serrano, T. Sukaew, E. T. Zellers, Hybrid preconcentration/focuser module for determinations of explosive marker compounds with a micro-scale gas chromatograph *J. Chrom. A*, 1279, 76-85, 2013.

[43] T. Sukaew, E. T. Zellers, Evaluating the dynamic retention capacities of microfabricated vapor preconcentrators as a function of flow rate *Sens. Actuators B: Chemical,* 183, 163-171, 2013.

[44] J. H. Seo, S. K. Kim, E. T. Zellers, K. Kurabayashi, Microfabricated passive vapor preconcentrator/injector designed for micro gas chromatography *Lab Chip*, 12 (4),717-724, 2012.

[45] Lahlou, H.; X. Vilanova, X. Correig, Gas phase micro-preconcentrators for benzene monitoring: a review *Sens. Actuators, B: Chemical*, 176, 198-210, 2013.

[46] H. Lord, J. Pawliszyn, Evolution of solid-phase microextraction technology, *J. Chrom. A.*, 885(1-2), 153-193, 2000.

[47] M. Chai, J. Pawlinszyn, Analysis of environmental air samples by solid-phase microextraction and gas-chromatography ion-trap mass-spectrometry, *Env. Sci. and Tech.*, 29 (3), 693-701, 1995.

[48] M. W. Ackley, Residence time model for respirator sorbent beds *Am. Ind. Hyg. Assoc. J.* 46 (11), 679-689, 1985.

[49] G. Wood, E. S. Moyer, A review of the wheeler equation and comparison of its applications to organic vapor respirator cartridge breakthrough data *Am. Ind. Hyg. Assoc. J.* 50 (8), 400-407, 1989.

[50] M. Harper, Evaluation of solid sorbent sampling methods by breakthrough volume studies, *Ann. Occup. Hyg.*, 37 1 (1993) 65-88.

[51] G. O. Wood, A review of the effects of covapors on adsorption rate coefficients of organic vapors adsorbed onto activated carbon from flowing gases, *Carbon*, 40 (2002) 685-694.

[52] C. Zhou, Y. Jin, H. Xu, S. Feng, G. Zhou, J. Liang, J. Xu, Use of wheeler-jonas equation to explain xenon dynamic adsorption breakthrough curve on granular activated carbon *J. Radioanal. Nucl. Chem.*, 288, 251-256, 2011.

[53] International Union of Pure and Applied Chemistry, Compendium of chemical terminology gold book, 2.3.3, 1174-1175, 2004, available at goldbook.iupac.org/P04804 (accessed May 2015).

[54] J. Namieśnik, Preconcentration of gaseous organic pollutants in the atmosphere *Talanta*, 35(7) 567-587, 1988.

[55] J. Whiting, R. Sacks, Evaluation of split/splitless operation and rapid heating of a multi-bed sorption trap used for gas chromatography analysis of large-volume air samples *J. Sep. Sci.*, 29, 218-227, 2006.

[56] R. L. Grob, E. F. Barry, *Modern practice of gas chromatography*, 4th edition, Wiley Interscience, Hoboken, NJ, 2004, pp. 114-115.
[57] J. C. Giddings, *Unified Separation Science*, Wiley-Interscience, New York NY, 1991.
[58] G. E. Spangler Height equivalent to a theoretical plate theory for rectangular gc columns, *Anal. Chem.*, 70, 4805-4816, 1998.
[59] G. R. Lambertus, C. S. Fix, S. M. Reidy, R. A. Miller, D. Wheeler, E. Nazarov, R. Sacks, Silicon microfabricated column with microfabricated differential mobility spectrometer for gc analysis of volatile organic compounds, *Anal. Chem.*, 77, 7563-7571, 2005.
[60] C. Lewis, J. F. Hamilton, C. N. Rhodes, J. Halliday, K. D. Bartle, P. Homewood, R. J. P. Grenfell, B. Goody, A. M. Harling, P. Brewer, G. Vargha, M. J. T. Milton, Microfabricated planar glass gas chromatography with photoionization detection, *J. Chrom. A*, 1217, 768-774, 2010.
[61] D. Radadia, R. D. Morgan, R. I. Masel, M. A. Shannon, Partially buried microcolumns for micro gas analyzers, *Anal. Chem.*, 81, 3471-3477, 2009.
[62] D. Radadia, A. Salehi-Khojin, R. I. Masel, M. A. Shannon, The effect of microcolumn geometry on the performance of micro-gas chromatography columns for chip scale gas analyzers, *Sens. Actuators, B Chemical*¸ 150, 456-464, 2010.
[63] S. Ali, M. Ashraf-Khorassani, L. T. Taylor, M. Agah, MEMS-based semi-packed gas chromatography columns, *Sens. Actuators, B Chemical*, 141, 309-315, 2009.
[64] M. A. Zareian-Jahromi, M. Agah, Microfabricated gas chromatography columns with monolayer-protected gold stationary phases, *J. Microelectromech. Syst.*, 19 (2), 294-304, 2010.
[65] J. V. Hinshaw, Anatomy of a peak, *LCGC Europe*, 17 (2004) 216-223.
[66] L. M. Blumberg, *Temperature-programmed gas chromatography*, Wiley-VCH, Weinheim, Germany, p. 69, 2010.
[67] E. Covington, F. I. Bohrer, C. Xu, E. T. Zellers, Ç. Kurdak, Densely integrated array of chemiresistor vapor sensors with electron beam patterned monolayer-protected gold nanoparticle interface films, *Lab Chip* 10 (2010) 3058-3060.
[68] E. Garcia-Berrios, T. Gao, J. C. Theriot, M. D. Woodka, B. S. Brunschwig, N. S. Lewis, Response and discrimination performance of arrays of organothio-capped au nanoparticle chemiresistive vapor sensors, *J. Phys. Chem.*, 115, 6208-6217, 2011.
[69] K. Scholten, F. I. Bohrer, E. Dattoli, W. Lu, E. T. Zellers, Organic vapor discrimination with chemiresistor arrays of temperature modulated tin-oxide nanowires and thiolate-monolayer-protected gold nanoparticles, *Nanotechnology*, 22, 1-7, 2011.
[70] R.-S. Jian, R.-X. Huang, C.-J. Lu, A micro gc detector array based on chemiresistors employing various surface functionalized monolayer-protected gold nanoparticles, *Talanta*, 88, 160-167, 2012.
[71] M. Maeder, Evolving factor analysis for the resolution of overlapping chromatographic peaks, *Anal. Chem.* 59 (1987) 527–530.
[72] H. R. Keller, D. L. Massart, Evolving factor analysis, *Chemometr. Intell. Lab.* 1991, 12, 209-224.
[73] R. Tauler, Multivariate curve resolution applied to second order data, *Chemometr. Intell. Lab. Sys.* 30 (1995) 133– 146.
[74] R. Manne, On the resolution problem in hyphenated chromatography, *Chemometr. Intell. Lab. Sys.* 27 (1995) 89-93.

[75] R. Tauler, A.K. Smilde, B. J. Kowalski, Local rank, three-way data analysis and ambiguity in multivariate curve resolution, *J. Chemometr.* 9 (1995), 31– 58.

[76] de Juan, R. Tauler, Chemometrics applied to unravel multicomponent processes and mixtures, revisiting latest trends in multivariate resolution, *Anal. Chim. Acta* 500 (2003) 195-210.

[77] E. Pére-Trepat, S. Lacorte, R. Tauler, Solving liquid chromatography mass spectrometry co-elution problems in the analysis of environmental samples by multivariate curve resolution, *J. Chromatogr. A* 1096 (2005) 111-122.

[78] J. Jaumot, R. Gargallo, A. de Juan, R. Tauler, A graphical user-friendly interface for MCR-ALS: a new tool for multivariate curve resolution in MATLAB, *Chemometr. Intell. Lab. Sys.* 76 (2005) 101-110.

[79] W. Windig, N. B. Gallagher, J. M. Shaver, B. M. Wise, A new approach for interactive self-modeling mixture analysis, *Chemometr. Intell. Lab. Sys.* 77 (2005) 85-96.

[80] J. C. Hoggard, R. E. Synovec, Parallel factor analysis (PARAFAC) of target analytes in GC × GC-TOFMS data: automated selection of a model with an appropriate number of factors, *Anal. Chem.* 79 (2007) 1611-1619.

[81] de Juan, R. Tauler, Factor analysis of hyphenated chromatographic data: exploration, resolution and quantification of multicomponent systems, *J. Chromatogr. A* 1158 (2007) 184–195.

[82] J. S. Nadeau, B. W. Wright, R. E. Synovec, Chemometric analysis of gas chromatography–mass spectrometry data using fast retention time alignment via a total ion current shift function, *Talanta* 81 (2010) 120-128.

[83] S. Mas, A. de Juan, R. Tauler, A. C. Olivieri, G. M. Escandar, Application of chemometric methods to environmental analysis of organic pollutants: a review, *Talanta* 80 (2010) 1052-1067.

[84] J. Kuligowski, G. Quintás, R. Tauler, B. Lendl, M. Guardia, Background correction and multivariate curve resolution of online liquid chromatography with infrared spectrometric detection, *Anal. Chem.* 83 (2011) 4855-4862.

[85] H. Abdollahi, R. Tauler, Uniqueness and rotation ambiguities in multivariate curve resolution methods, *Chemometr. Intell. Lab. Sys.*108 (2011) 100-111.

[86] L. W. Hantao, H. G. Aleme, M. P. Pedroso, G. P. Sabin, R. J. Poppi, F. Augusto, Multivariate curve resolution combined with gas chromatography to enhance analytical separation in complex samples: a review, *Anal. Chim. Acta* 731 (2012) 11-23.

[87] Jin, E. T. Zellers, Chemometric analysis of gas chromatographic peaks measured with a microsensor array: methodology and performance assessment, *Sensor Actuat. B-Chem.* 139 (2009) 548-556.

[88] Jin, P. Kurzawski, A. Hierlemann, E. T. Zellers, Evaluation of multitransducer arrays for the determination of organic vapor mixtures, *Anal. Chem.*, 80, 227-236, 2008.

[89] S.C. Terry, H. Jermann, J. Angel, A gas chromatograph air analyzer fabricated on a silicon wafer, *IEEE Trans. Electron Dev.,* 26, 1880-1887, 1979.

[90] S. Kolesar, R. R. Reston, Review and summary of a silicon micromachined gas chromatography system, *Proc. IEEE Trans. Comp. Packag. Manufact. Technol. B*, 21, 324-328, 1998.

[91] G. Frye-Mason, R. Kottenstette, P. Lewis, E. Heller, R. Manginell, D. Adkins, G. Dulleck, D. Martinez, D. Sasaki, C. Mowry, C. Matzke, L. Anderson, Hand-held miniature chemical analysis system (μChemLab) for detection of trace concentrations of

gas phase analytes, *Proc. Micro Total Analysis Systems Workshop*, Enschede, Netherlands, May, 229-232, 2000.

[92] J. Lu, J. Whiting, R. D. Sacks, E. T. Zellers, Portable gas chromatograph with tunable retention and sensor array detection for determination of complex vapor mixtures, *Anal. Chem.* 75 (2003) 1400-1409.

[93] C-J. Lu, W.H. Steinecker, W-C. Tian, M.C. Oborny, J.M. Nichols, M. Agah, J.A. Potkay, H.K.L. Chan, J. Driscoll, R.D. Sacks, K.D. Wise, S. W. Pang, E.T. Zellers, First-generation hybrid MEMS gas chromatograph, *Lab Chip*, 5, 1123-1131, 2005.

[94] P.R. Lewis, R.P. Manginell, D.R. Adkins, R.J. Kottenstette, D.R. Wheeler, S.S. Sokolowski, D.E. Trudell, J.E. Bymes, M. Okandan, J.M. Bauer, R.G. Manley, G.C. Frye-Mason, Recent advancements in the gas-phase µChem Lab, *IEEE Sensors J.*, 6, 784-795, 2006.

[95] P. J. Chapman, F. Vogt, P. Dutta, P. G. Datskos, G. L. Devault, M. J. Sepaniak, Facile hyphenation of gas chromatography and a microcantilever array sensor for enhanced selectivity, *Anal. Chem.* 79 (2007) 364-370.

[96] S. Zampolli, I. Elmi, F. Mancarella, P. Betti, E. Dalcanale, G. C. Cardinali and M. Severi, Real-time monitoring of sub-ppb concentrations of aromatic volatiles with a MEMS-enabled miniaturized gas-chromatograph, *Sens. Actuator, B Chemical.*, 141, 322-328, 2009.

[97] Q. Zhong, W. Steinecker, E. T. Zellers, Characterization of a high-performance portable GC with a chemiresistor array detector, *Analyst* 134 (2009) 283-293.

[98] S. K. Kim, H. Chang, E. T Zellers, Microfabricated gas chromatograph for selective determination of trichloroethylene at sub-parts-per-billion concentrations in complex mixtures, *Anal. Chem.* 83, 7198-7206, 2011.

[99] S. K. Kim, D. R. Burris, H. Chang, J. Bryant-Genevier, and E. T. Zellers, Microfabricated gas chromatograph for on-site determinations of trichloroethylene in indoor air arising from vapor intrusion, part 1: field evaluation, *Env. Sci. and Tech.*, 46, 6065-6072, 2012.

[100] S. K. Kim, D. R. Burris, J. Bryant-Genevier, K. A. Gorder, E. M. Dettenmaier, E. T. Zellers, Microfabricated gas chromatograph for on-site determinations of trichloroethylene in indoor air arising from vapor intrusion, part 2: spatial/temporal monitoring, , *Env. Sci. and Tech.*, 46, 6073-6080, 2012.

[101] J. Liu, J. H. Seo, Y. B. Li, D. Chen, K. Kurabayashi, X. D. Fan, Smart multi-channel two-dimensional micro-gas chromatography for rapid workplace hazardous volatile organic compounds measurement, *Lab Chip*, 13 (5), 818-825, 2013.

[102] X. Chen, T. Y. Hung, R. S. Jian, C-J. Lu, A multidimensional micro gas chromatograph employing a parallel separation multi-column chip and stop-flow µGC × µGCs configuration, *Lab Chip*, 13 (7), 1333-1341, 2013.

[103] R.-S. Jian, Y.-S. Huang, S.-L. Lai, L.-Y. Sung, C.-J. Lu, Compact instrumentation of a µ-gc for real time analysis of sub-ppb VOC mixtures, *Microchemical Journal,* 108, 161-167, 2013.

[104] Y. T. Qin, Y. B. Gianchandani, iGC1: An integrated fluidic system for gas chromatography including knudsen pump, preconcentrator, column, and detector microfabricated by a three-mask process, *J. Microelectromech. Syst.*, 23 (4), 980-990, 2014.

[105] W. R. Collin, G. Serrano, L. K. Wright, H. Chang, N. Nuñovero, E. T. Zellers, Microfabricated gas chromatograph for rapid, trace-level determinations of gas phase explosive marker compounds, *Anal. Chem*., 86, 655-663, 2014. (sensor photo ref, Fig 2.1)

[106] W. Collin, A. Bondy, D. Paul, K. Kurabayashi, E. T. Zellers, μGC × μGC: comprehensive two-dimensional gas chromatographic separations with microfabricated components, Anal. Chem., 87 (3), 1630-1637, 2015.

[107] Garg, M. Akbar, E. Vejerano, S. Narayanan, L. Nazhandali, L. C. Marr, M. Agah, Zebra GC: A mini gas chromatography system for trace-level determination of hazardous pollutants, *Sens. Actuator, B: Chemical*, 212, 145-154, 2015.

[108] GCM 5000 GC-Module, SLS Micro Technology, available at http://www.speciation.net/Database/Instruments/SLS-MICRO-TECHNOLOGY/GCM-5000--GCModule-;i2337, (accessed July 2015).

[109] TOCAM, Defiant Technologies, available at www.defiant-tech.com/TOCAM.php, (accessed July 2015).

[110] GCAP, APIX analytics, available at http://www.apixanalytics.com/gcap/, (accessed July 2015).

[111] J. W. Grate, Acoustic wave microsensor arrays for vapor sensing, *Chem. Rev.*, 100, 2627-2648, 2000.

[112] M. Batzill, U. Diobold, The surface and materials science of tin oxide, *Progress in Polymer Science*, 79 (2-4), 47-154, 2005.

[113] B. Adhikari, S. Majumdar, Polymers in sensor applications, *Progress in Polymer Science*, 29 (7), 699-766, 2004.

[114] M. E. Franke, T. J. Koplin, U. Simon, Metal and metal oxide nanoparticles in chemiresistors: does the nanoscale matter?, *Small*, 2 (1), 36-50, 2006.

[115] H.B. Zhu, R. Nidetz, M. L. Zhou, J. Lee, S. Buggaveeti, K. Kurabayashi, X. D. Fan, Flow-through microfluidic photoionization detectors for rapid and highly sensitive vapor detection, *Lab on a Chip*, 15 (14), 3021-3029, 2015.

[116] A. Buttry, M. D. Ward, Measurement of interfacial processes at electrode surfaces with the electrochemical quartz crystal microbalance, *Chem. Rev.*, 92 (6), 1355-1379, 1992.

[117] G. Serrano, S. Reidy, E. T. Zellers, Assessing the reliability of wall-coated microfabricated gas chromatographic separation columns, *Sensors and Actuators: B Chemical*, 141, 217-226,2009.

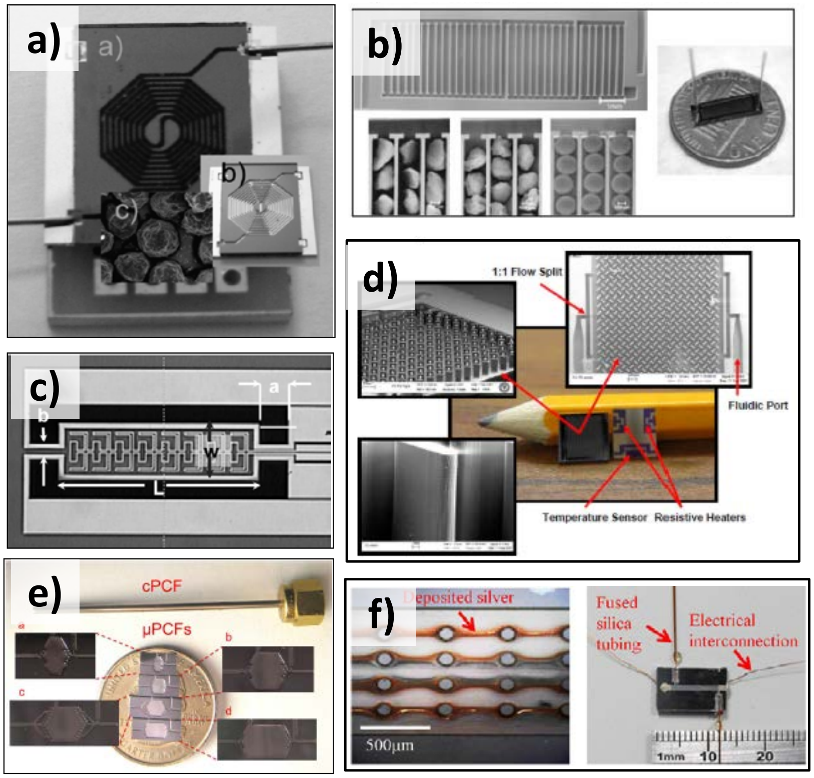

Figure 1.1 Photographs of reported microfabricated vapor preconcentrators; a) from Garcia et. al., reference #37, b) from Tian et. al., reference #93, c) from Manginell et. al., reference #35, d) from Alfeeli et. al., reference #38, e) from Sukaew et. al., reference #43, and f) from Tian et. al, reference #40.

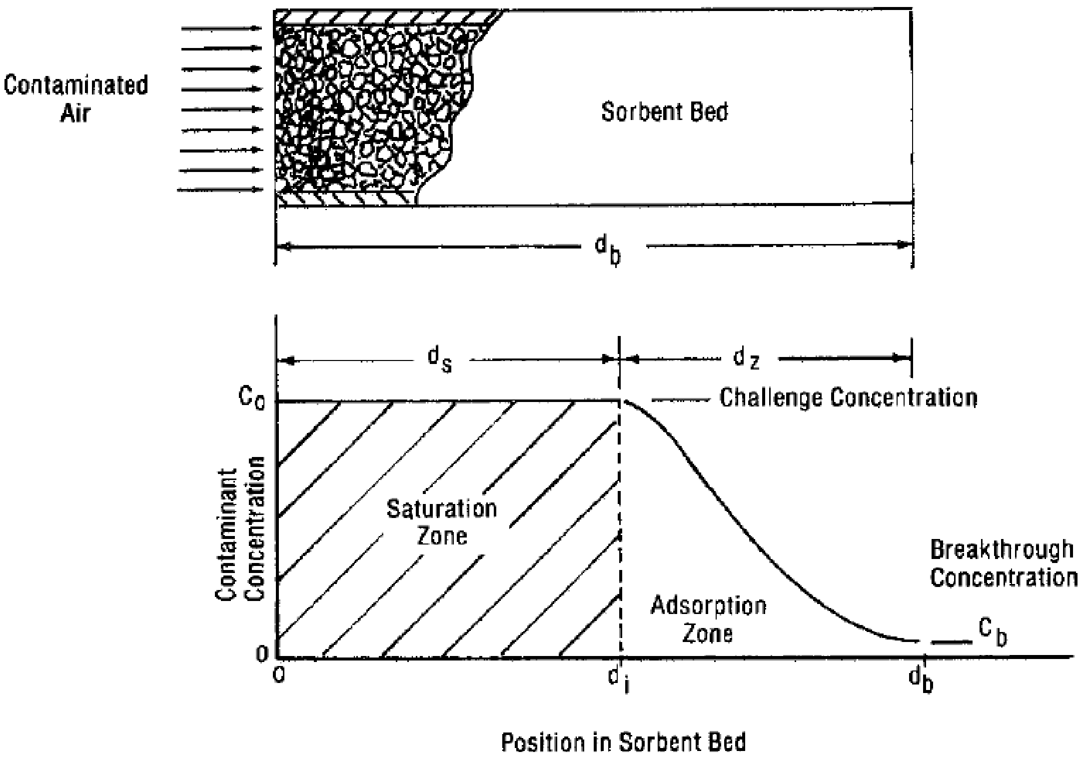

Figure 1.2 Diagram of the concentration profile of an analyte (contaminated air here) being sampled through a packed adsorbent bed, taken from reference #49.

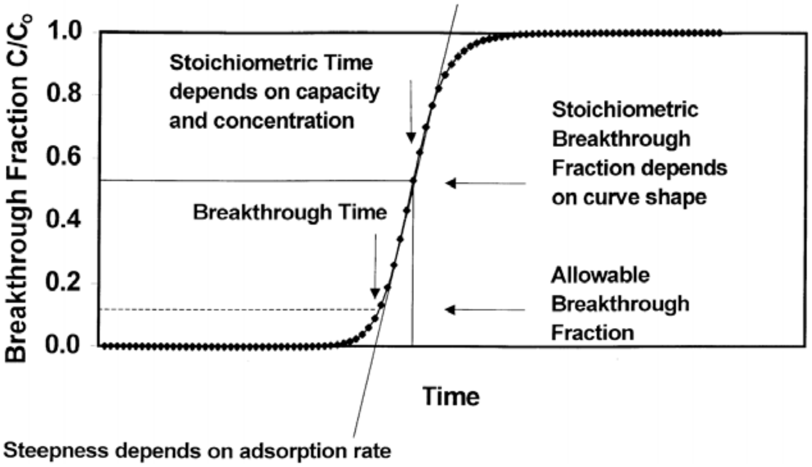

Figure 1.3 Example breakthrough curve with key characteristics explained, taken from reference #48.

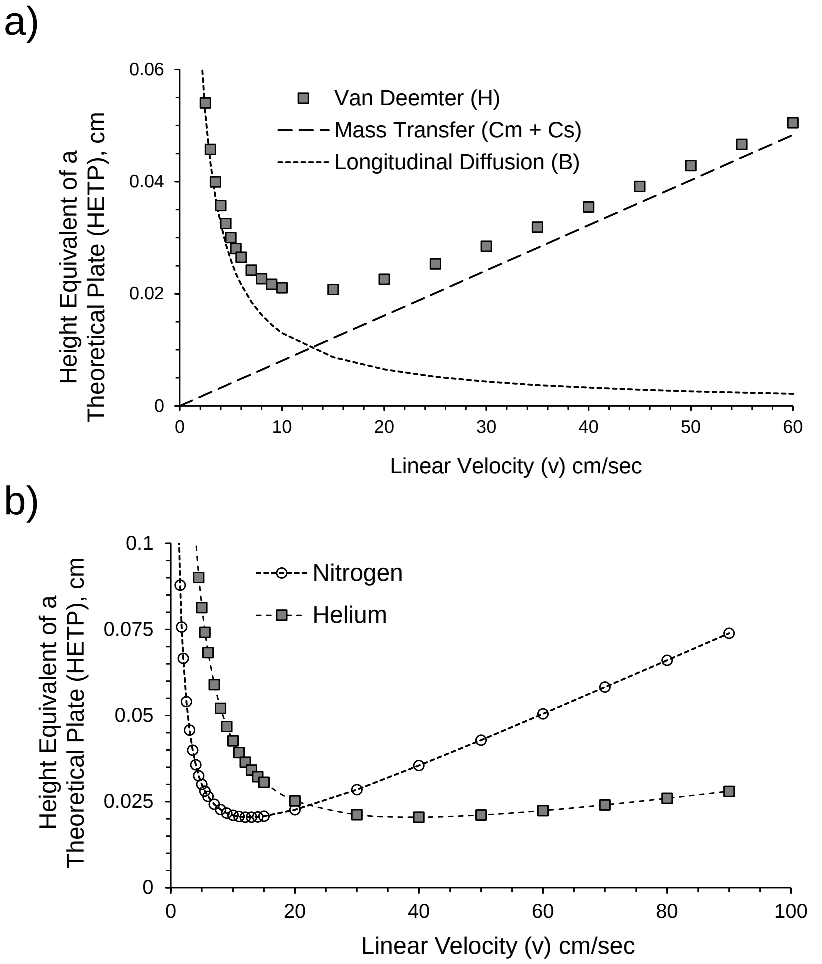

Figure 1.4 Example van Deemter plots for a hypothetical analyte; a) height equivalent of a theoretical plate (HETP) as a function of linear velocity of the mobile phase, in this case nitrogen (filled squares), with contributions from longitudinal diffusion and mass transfer shown as dotted lines (for reference: R = 0.2, D_s = 0.00277 cm^2/s, R_c = 0.0125 cm, d = 0.000025 cm, D_m for nitrogen = 0.065 cm^2/s. b) Comparison in HETP for nitrogen (open circles) and helium (filled squares) carrier gases (for reference: D_m for helium = 0.2).

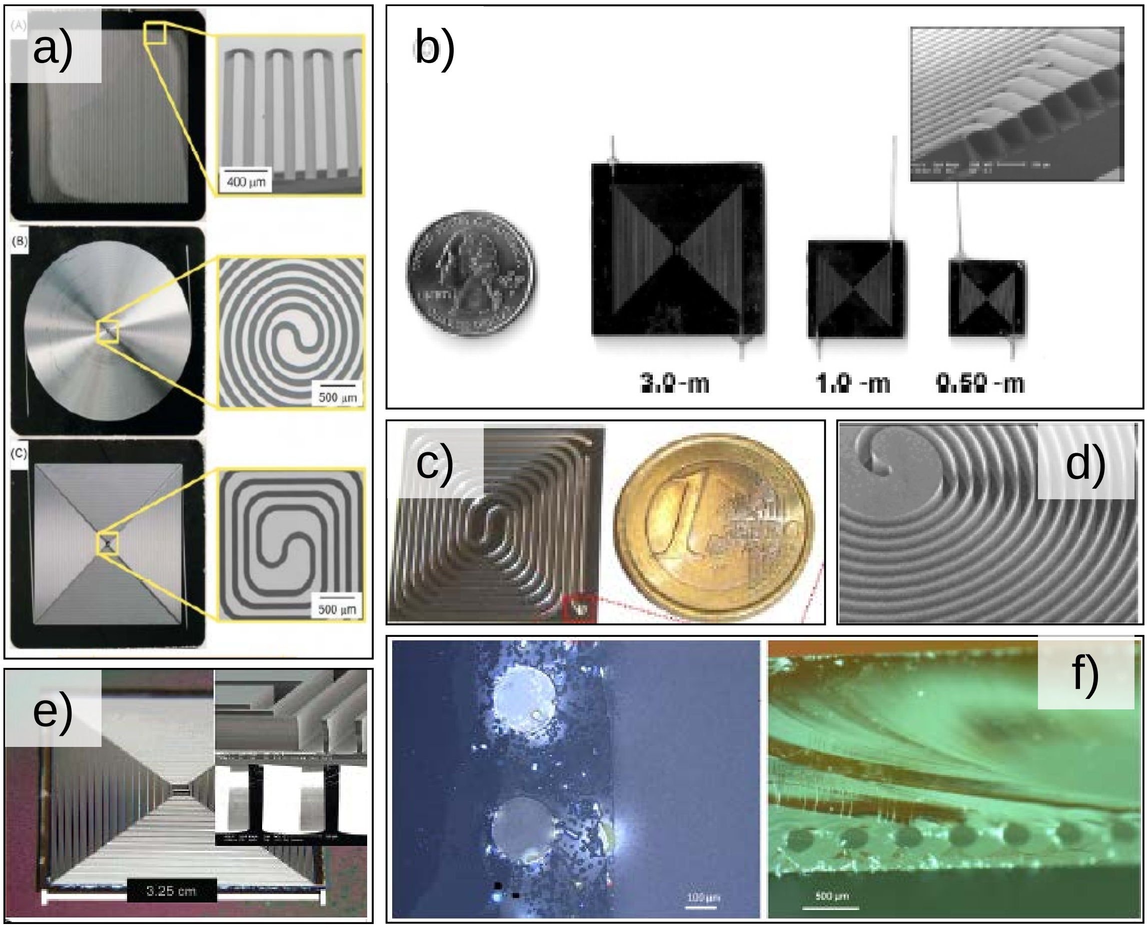

Figure 1.5 Photographs of reported microfabricated gas chromatography separation columns; a) from Radadia et. al., reference #62, exploring the effects of column geometry, b) from Serrano et. al., reference #117, c) from Zampolli et. al., reference #96, d) from P. Lewis et. al. , reference #94, e) from Lambertus et. al., reference #59, and f) from A. Lewis et. al, reference #60, developing a method for creating circular cross-sectional area column in glass.

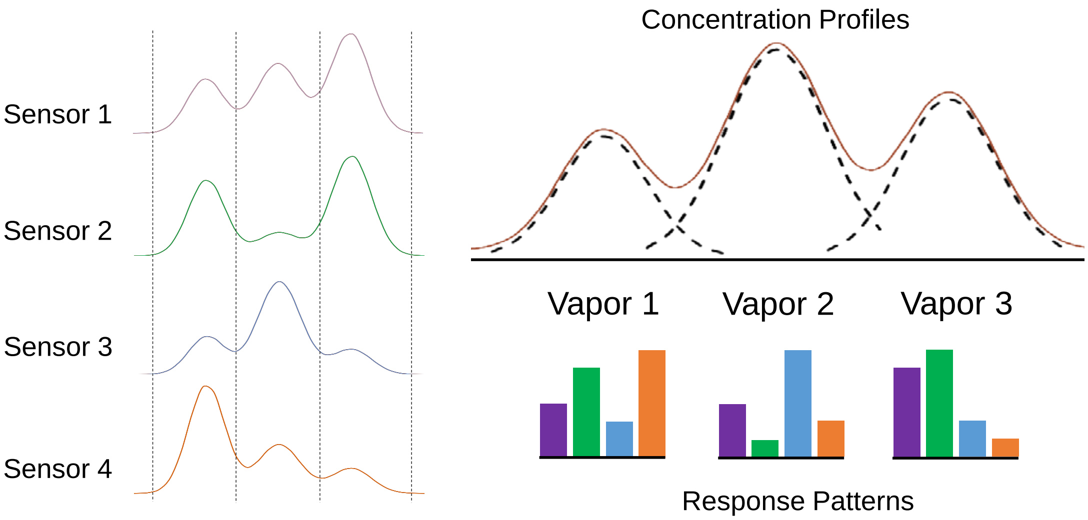

Figure 1.6 Deconvolution of overlapping chromatographic peaks. Raw chromatograms from four sensors of three co-eluting vapors are shown at left. Analysis by evolving factor analysis and alternating least squares solves for the best fit bilinear combination of concentration profiles and response patterns of each vapor, shown at right. Each bar in the bar charts correspond to normalized sensitivities from each sensor in the array.

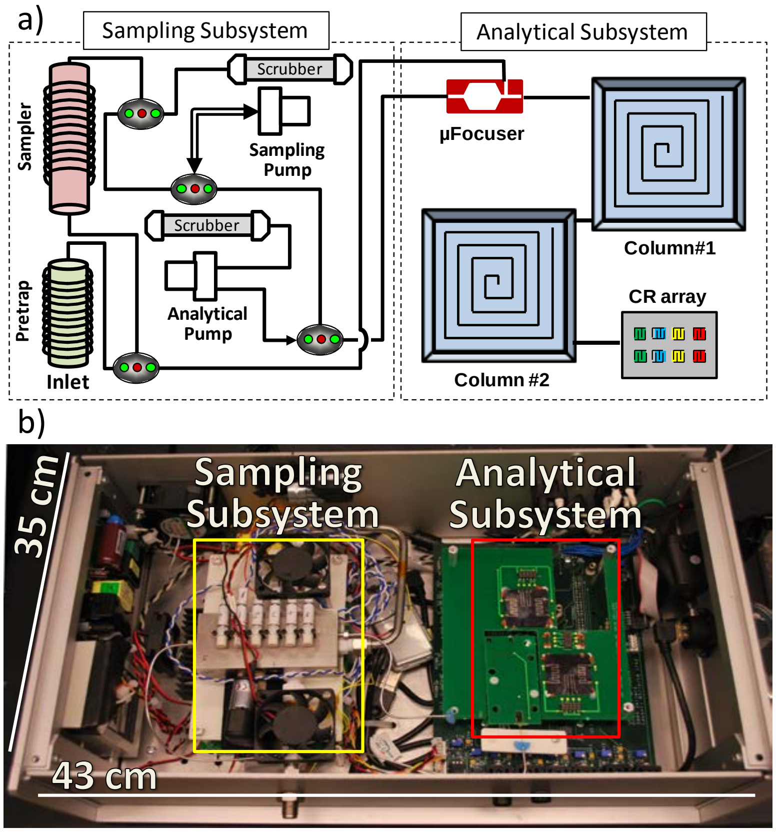

Figure 1.7 a) Schematic diagram/layout of the sampling and analytical subsystems of the SPIRON μGC, b) Photograph of the field prototype, from reference #98.

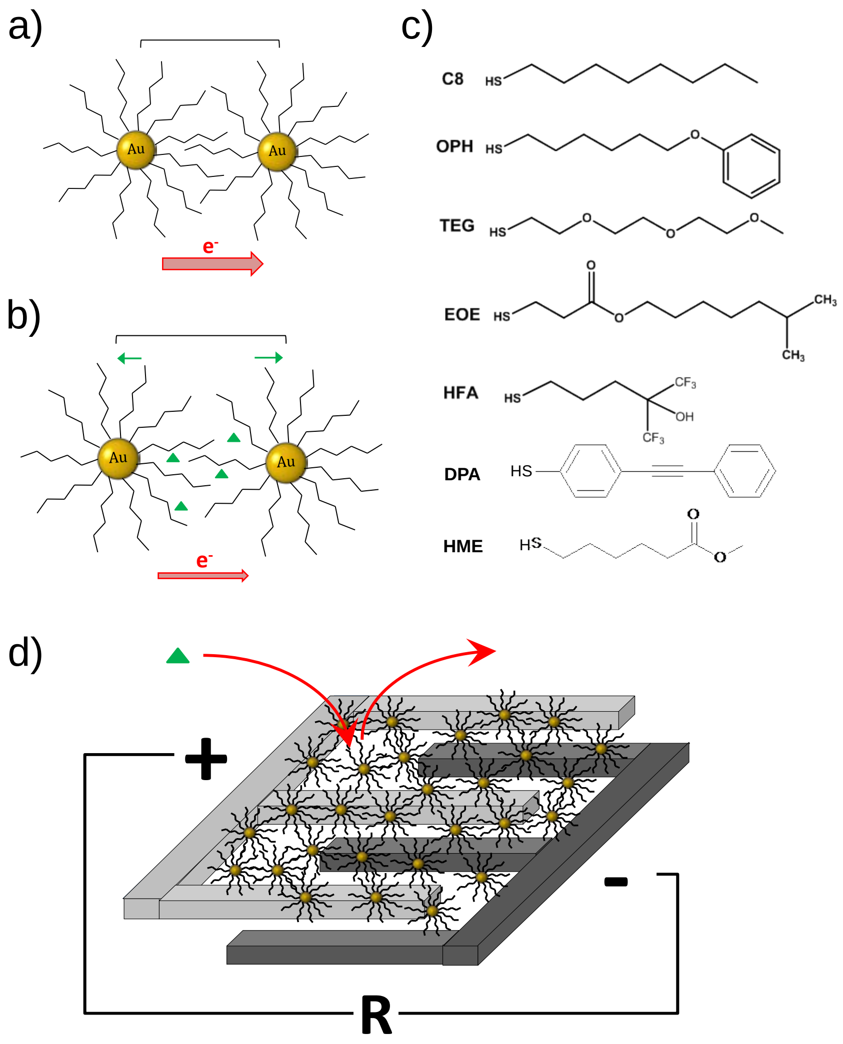

Figure 1.8 Cartoon diagram of a monolayer protected gold nanoparticle (MPN) film chemiresistor vapor transducer (CR), with a) and b) showing the primary mechanism of response, in which nanoparticle core spacing increases as vapors (green triangles) absorb into the MPN film, causing an increase in the film's resistance. c) List of thiol ligands used in the CRs presented in this thesis, d) schematic cartoon of the interdigitated electrodes with the MPN film deposited above for interaction with vapors.

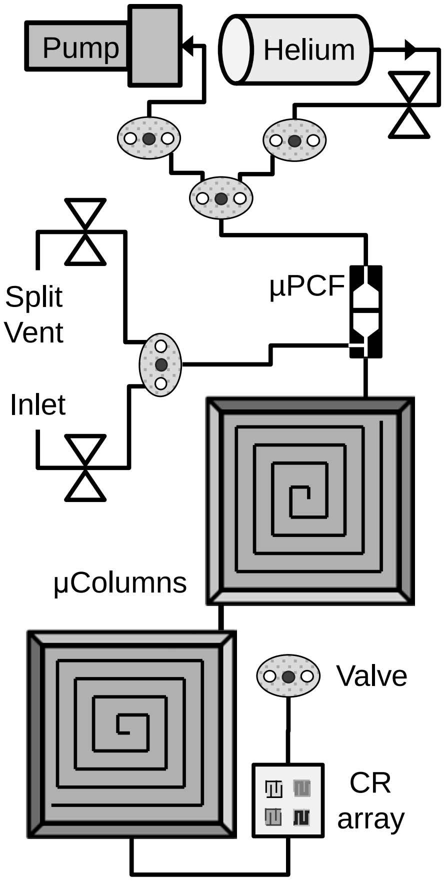

Figure 1.9 Fluidic layout of the Gen-1.5 PEMM µGC. VOCs from air samples are drawn through the inlet by the on-board mini-pump and captured in the µPCF, and then thermally desorbed and backflushed into the first of two identical 3-m separation µcolumns on a background of He gas. Detection is via an array of MPN coated chemiresistor sensors.

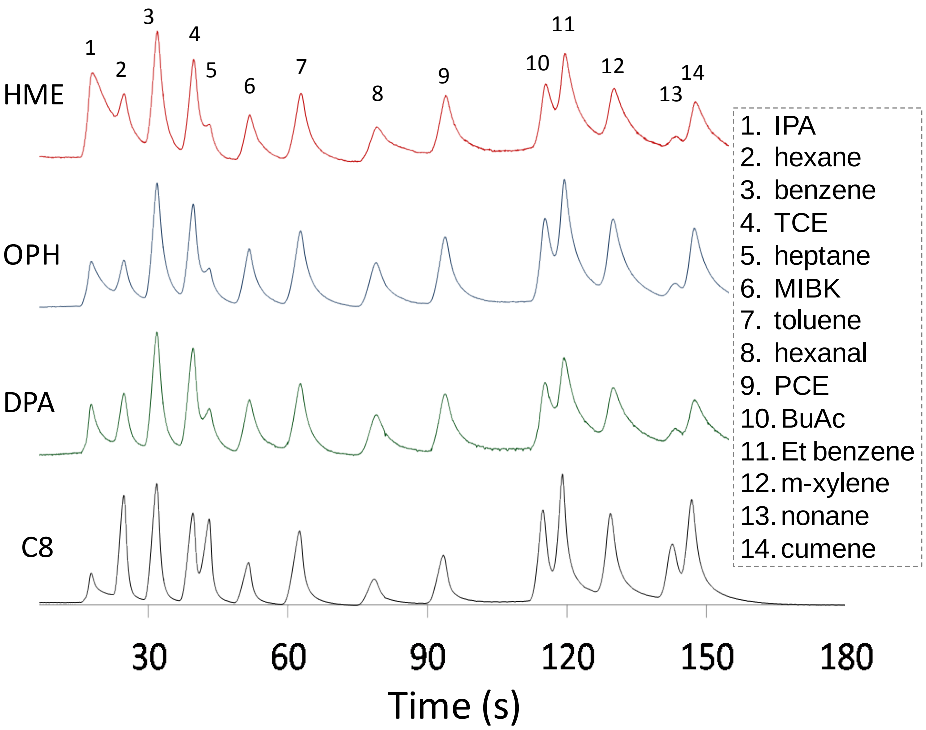

Figure 1.10 Chromatogram generated using a “micro-components only” version of the SPIRON field prototype. The peaks correspond to masses of analyte ranging from 0.04 to 1.0 µg, for the least to most volatile compounds in the mixture, respectively.

Chapter 2

Multivariate Curve Resolution of Co-Eluting Vapors from a Gas Chromatograph with Microsensor Array Detector

2.1 Introduction

The use of microsensor arrays with sorptive interface layers for the quantitative analysis of mixtures of volatile organic compounds (VOC) generally requires upstream gas chromatographic (GC) separation because the diversity of responses achievable with stand-alone arrays of this type is severely limited; the composite pattern of responses from a mixture of three or more vapors typically cannot be reliably differentiated from those of the individual components or their lower-order mixtures.[1-4] The temporal separation provided by GC can alleviate this problem, but as GC systems continue to be miniaturized and analysis times are reduced, chromatographic resolution invariably decreases, which raises the likelihood of overlapping peaks among the mixture components.[5,6]

Although several reports have appeared on the use of hyphenated (μ)GC-microsensor array instrumentation for VOC mixture analysis the chemometric analysis of data derived from such systems has not been studied extensively.[6-13] In earlier explorations of this topic, we applied classification models derived from extended disjoint principal component regression (EDPCR) to assign identities to chromatographically resolved peaks corresponding to individual vapors and to composite peaks corresponding to unresolved or partially resolved binary mixtures, on the basis of the array response patterns derived from the corresponding peak areas.[1-3,8,12] If two peaks overlapped at all, then they were treated as an unresolved binary mixture, ignoring the potential value of partial chromatographic resolution.

Since the response pattern produced by a microsensor array exposed to a vapor phase analyte is analogous to a spectrum produced by a spectrometer, multivariate curve resolution (MCR) methods should be readily applicable to microsensor arrays used as GC detectors. The primary difference is the amount of independent information about the analytes that can be derived from the detector output, which is expected to be much less for a microsensor array than for a spectrometer.

The purpose of the current study was to evaluate the performance of a hybrid evolving factor analysis and alternative least squares (EFA-ALS) curve resolution algorithm with *experimental data* from an MPN-coated chemiresistor (CR) array used as a GC detector. Using the framework of our previous study discussed in Chapter 1,[14] the capability to determine the number of components (i.e., the chemical rank) in each composite peak and to extract the pattern and concentration of each component were evaluated over a range of chromatographic resolution, R_s, and relative response ratio, *RRR*, values for pairs of vapors with different (Pearson) correlation coefficients, ρ.

After describing our methodology and various aspects of the individual and collective array responses for the three pairs of vapors tested, we present an assessment of the additivity of responses from the sensors in the binary composite peaks. The preprocessing steps required to address differences in retention time, t_R, and peak asymmetry among the sensors are then described. This is followed by an evaluation of rank determinations by EFA. The fidelity of the response patterns recovered by EFA-ALS to those in the calibration library, and the accuracy of quantification, are examined as a function of R_s, RRR, ρ, using two different “modes” (i.e., blind mode and informed mode) that differ in terms of the amount of *a priori* information used in the ALS step. Results are compared to those obtained using EDPCR, which ignores the partial chromatographic resolution of the components in the composite peaks.

2.2 Experimental and chemometric methods

2.2.1 Materials

All test compounds were purchased from Sigma-Aldrich/Fluka (Milwaukee, WI) or Acros/Fisher (Pittsburgh, PA) in >98% purity and were used as received. MPNs having monolayers derived from the following thiols were taken from existing supplies synthesized by a previously reported method:[15] n-octanethiol (C8), 6-phenoxyhexane-1-thiol (OPH), 4-(phenylethynyl)-benzenethiol (DPA), and methyl-6-mercaptohexanoate (HME). Average Au core diameters were ~ 4 nm. The thiolate monolayers on these MPNs span a sufficiently wide range of structures and vapor affinities to afford reasonably high selectivity among different VOCs, from the non-polar C8 to the more strongly dipolar HME.[10,15,16]

2.2.2 Microsensor array

The CR array chip (2.0 × 1.2 cm) is the same as that discussed in chapter 1 and used in several previous studies from this laboratory; a photograph is shown in Figure 2.1 [taken from ref 12].[9,10,12,] deposited by drop casting from solution to create multilayer films with baseline resistance values, R_b, of 0.48, 1.0, 4.4, and 7.8 MΩ, for C8, DPA, OPH, HME, respectively (note: only one of each pair of similarly coated sensors was used). Film thicknesses were not measured, but previous work suggests that this method produces non-uniform films with average thicknesses in the range of 100 to 400 nm.[16,17]

A Macor lid was sealed to the substrate at the periphery of the array using a self-adhesive VHB-tape gasket (3M, St. Paul, MN) and thin film of silicone putty (Duraseal, 1531 Cotronics, Brooklyn, N.Y.), creating a detector cell volume of 1.6 μL. Deactivated fused-silica capillaries (0.25 mm i.d., 0.32 mm o.d., Restek Corp., Belafonte, PA) were inserted into drilled inlet/outlet holes in the lid and sealed with epoxy (Hysol Epoxy Patch 1C, Henkel Corp., Rocky Hill, C.T.). Header pins were soldered to the contact pads, bent to a 90° angle, and inserted into a socket mounted on a printed circuit board (PCB).

Each CR was connected to a parallel matching reference resistor to create a voltage divider circuit, and the voltage across the CR sensor was amplified. A constant potential of 3V from a CR2032 battery was applied to each CR circuit. The output voltage was collected at 20 Hz from each sensor, before and after amplification, and passed via a DAQ card to a laptop computer where the data were logged as a function of time. Changes in MPN film resistance, normalized to the baseline resistance (i.e., $\Delta R/R_b$) were calculated from the corresponding voltages by the data management software.

2.2.3 Testing configuration

The test set-up is shown in Figure 2.2. The CR array was connected to the distal end of a conventional capillary column (6-m long, 250-μm i.d., 0.25-μm thick PDMS phase, Supelco, Belafonte, PA). The column was located inside the oven of a bench-scale GC (Model 7890, Agilent Technologies, Palo Alto, CA) and the PCB-mounted CR array was placed on the bench beside the GC. Fluidic connections to the capillary column and FID inside the GC were made with press-tight fittings using ~10-cm segments of deactivated fused-silica capillary fed through the oven-door seal. The stability of the sensor temperatures during temperature programming of the column in the oven was inferred by the lack of any baseline drift in the sensor outputs.

Samples from test atmospheres generated in N_2 in Supel Inert® gas sampling bags (Supelco) were drawn through a 25-µL gas sampling loop by a commercial mini-pump, and injected into the column via a 6-port valve under a flow of N_2 carrier gas. All chromatograms were run isothermally. Injected masses of each test compound were confirmed by an FID downstream from the CR array, which had been previously calibrated with solutions of the test compounds in CS_2. The carrier gas flow rate was 1.0 mL/min for all trials, as measured by a downstream bubble flow meter. Individual chromatograms were analyzed using GRAMS 32 (Thermo Fisher Scientific, Waltham, MA) and any shift in pre- and post-peak baselines were corrected by linear interpolation prior to further analyses of the peaks.

2.2.4 Screening tests and selection of vapor pairs

A set of 25 compounds, spanning a range of retention times from 40 to 210 s when run isothermally at 30 °C, was screened to find appropriate pairs for evaluating the EFA-ALS method. Two criteria were applied: the members of a pair had to have retention times similar enough to allow R_s to be adjusted over the desired range (0.1 to 1.0) with moderate changes in column temperature; and the value of ρ between the responses to the members of a pair had to be such that among the three pairs chosen there was a wide enough range of ρ values to permit the effect of pattern similarity on the performance of the EFA-ALS analyses to be assessed (see below for metrics). For assessing pattern similarity, the peak-maxima sensor sensitivities ($\Delta R/R_b$/ng) for each vapor were normalized by dividing by that of the most sensitive sensor in the array (MSS) for that vapor, and the normalized sensitivities from each of the four sensors for one member of a pair were regressed onto those for the other member (Figure 2.3). The resulting values of ρ were calculated. Similar analyses were performed on the peak-area sensitivities.

The following three pairs were selected: methyl isobutyl ketone + toluene (MIBK+TOL; $\rho = 0.85$), 1-octene + n-butyl acetate (OCN+BAC; $\rho = 0.59$), and nitroethane + cyclohexane (NET+CHX; $\rho = -0.57$) (see Table 2.1). The corresponding Euclidean distances (*ED*) between the vectors for each vapor in the pair, also calculated from the normalized sensitivities, were 0.33, 0.79, and 1.28 (Table 2.1). For reference, the maximum possible *ED* value for the normalized data is 2.0, as there are 4 sensors, each of which has a sensitivity of 0 to 1; thus, the maximum *ED* separating two vapors is $4^{1/2} = 2$.

2.2.5 Calibration, test conditions, preprocessing

Calibrations were performed with the individual test compounds by injecting discrete samples from bag test-atmospheres at 6 or 7 concentrations through the 6-port valve and sampling loop. The calibration spanned ≥10-fold range of masses between 20 to 600 ng for any compound. The mass range exceeded the range used for subsequent tests of binary mixtures. Plotting the $\Delta R/R_b$ values derived from the baseline-corrected peak maxima vs. injected mass with forced zero y-intercept yielded a linear calibration curve ($r^2 > 0.979$) the slope of which comprised the sensitivity for a given sensor-vapor combination **(**Figure 2.4).

For testing, seven static test-atmospheres of each binary mixture were generated and analyzed. Concentrations were adjusted to give average *RRRs* of approximately 1:10, 1:5, 1:2.5, 1:1, 2.5:1, 5:1, and 10:1, respectively, for the members of a given pair. Actual *RRR*s may have differed by 10-20% from the target values. For NET+CHX, *RRR* values of 1:20 and 20:1 were used instead of 2.5:1 and 1:2.5 to examine the performance of EFA-ALS for the least correlated pair under more challenging conditions. Figure 2.5 provides some examples of Gaussian peaks from a hypothetical single-channel detector for selected combinations of R_s and *RRR*, which illustrate the nature of the composite peaks addressed here.

The minimum injected mass was greater than 5 times the limit of detection (LOD) for the least sensitive sensor in the array for all but one of the binary mixture cases (the exception was > 3×LOD). A single test was run at each value of R_s and *RRR*. All tests with a given vapor pair were conducted within a three day period, during which sensitivities remained quite stable. At the lowest oven temperature, the peaks for the members of any pair were fully resolved (i.e., $R_s > 4$). The areas of the fully resolved peaks were used as reference values for assessing the additivity of responses for the overlapped cases, and the peak maxima were used for assessing the accuracy of quantification of the profiles estimated by EFA-ALS.

Values of R_s were determined on the basis of the downstream FID traces using the following equation: $R_s = 0.59\Delta t_r/W_{1/2}$, where $W_{1/2}$ is the average full-width-at-half-maximum of the two peaks and Δt_r is the difference in retention time).[18] The net change in oven (column) temperature required to span R_s values of 0.1, 0.5, and 1.0 was roughly 35°C in all cases, and the specific temperature required to achieve each R_s value was determined using the test atmosphere corresponding to an (average) *RRR* = 1:1. Since the peaks measured with the CR sensors were generally wider and less symmetric than those from the downstream FID, and the degree of asymmetry differed among the sensors (see below), the actual (i.e., sensor-wise) R_s values were always less than the stated (FID-wise) values. Prior to EFA-ALS analyses, it was necessary to correct for slight differences in retention times among the sensors and for differences in peak tailing among the sensors for a given vapor (described further below). Note that the *RRR* values are averaged over all sensors for each member of a pair/mixture. The range of individual *RRR* values spans a much larger range due to individual differences in sensitivity. For example, an *RRR* of 10:1 for the NET+CHX pair corresponds to a range of sensor-specific *RRR* values between 80:1 and 2:1, respectively.

2.2.6 EFA and ALS

Details of the generic EFA and ALS algorithms used here are discussed in Chapter 1. The EFA algorithm developed by the Tauler group and made available on their website was used to determine the rank of each composite peak (after pre-processing; see below) using MatLab.[19] EFA was performed on the submatrices of $\boldsymbol{Y}_i$ from equation 1.9 in Chapter 1 (i.e., each row in the matrix $\boldsymbol{Y}$ consisting of the set of sensor responses) to calculate the eigenvalues of the response vector for each retention time, increasing the window by 0.05 sec for each evolution based on the frequency of data sampling from the detector (20 Hz). This was done initially in the forward direction (i.e., increasing elution time). Retention times where sharp increases in the magnitude of the eigenvalues occur reveal when a compound begins to elute. A single noise threshold, established by analyzing single component chromatograms of each vapor, was applied to samples of all three mixtures to determine rank. EFA performed in the reverse direction, with respect to time, revealed the end of the eluting peak, and the elution range of each compound was determined by merging the results of the forward EFA and backward EFA.[20]

Code written in-house in MatLab was used for generating initial estimates of concentration profiles and response patterns by EFA. ALS was performed using the algorithm developed by the Lin group,[21,22] with the constraint that all values in both the concentration and pattern matrices had to be positive.

EFA-ALS was performed in two modes. In “blind” mode, the estimates of normalized response patterns and concentration profiles used for ALS were taken directly from the output of EFA. In “informed” mode, the normalized library patterns for the pair members were used for ALS instead of the EFA-generated estimates. The latter was rationalized on the basis of the fact that the identities of the binary composite peaks would be known *a priori*. EFA-generated estimates of the concentration profiles were used for both blind-mode and informed-mode analyses. The convergence of the ALS algorithm was denoted by the point at which further iteration changed the residual error matrix ***E*,** from equation 1.9 in Chapter 1, by $\leq 10^{-6}$.

2.2.7 Extracted pattern fidelity, vapor recognition, and quantification

Extracted response pattern for each mixture component was compared to the library patterns for the two components comprising the composite peak. Analyte masses were estimated by comparing the peak maxima of the reconstructed chromatogram from the most sensitive sensor in the array (vapor specific) to the appropriate calibration curve.

Pattern fidelity testing was performed in two stages using the *ED* as the metric of pattern fidelity. First, if the *ED* between the extracted and correct library vectors (i.e., patterns) was smaller than that between the extracted and alternative-vapor library patterns, then the vapor was considered to have been correctly recognized. If this “*ED*-proximity” criterion was met, then a more rigorous test of fidelity was applied by placing a limit on the value of the *ED* between the extracted and library patterns. An *ED* limit of 0.20 was established by calculating the 99% confidence interval around the largest standard deviation of replicate normalized response patterns created from the maxima of the fully resolved (reference) chromatograms. We refer to this in the discussion below as the “*ED*-threshold” criterion.

2.3 Results and discussion

2.3.1 General features of the data set

Calibration curves, derived from (baseline corrected) peak maxima or peak areas, were linear for all vapors and sensors, with forced-zero regression r^2 values > 0.98 in all cases. The former (Figure 2.3) were used for quantification of the EFA-ALS extracted response profiles. The slopes (i.e., sensitivities) for a given vapor among the sensors in the array differed by as much as 11-fold (for CHX) and by as little as 3.3-fold (for NET).

Although most of the relative sensitivities are in accordance with what would be expected on the basis of vapor-MPN affinities, several exceptions were noted. For example, although the C8-coated sensor had the expected higher sensitivity toward the non-polar alkane and alkene vapors, it also had higher sensitivity toward the polar MIBK and BAC vapors than did the (polar) HME-coated sensor. In addition, the moderately polar OPH-coated sensor had higher peak-maxima sensitivity toward NET than did the HME sensor. In contrast, for the peak area data, the relative sensitivities are in accordance with what would be expected on the basis of vapor-MPN affinities; the C8 sensor retains its higher sensitivity for the non-polar vapors, and the HME sensor shows the highest sensitivity for the more polar MIBK, BAC, and NET vapors.

The differences in relative sensitivities between peak maxima and peak areas arise from the dependence of the sensor responses on the rates of sorption or desorption of the vapors into or out of the MPN films, particularly for the polar vapors in the polar HME film.[16] Differences in the extent of tailing in the peaks among the sensors (discussed below) are also ascribable to this factor, and may have been enhanced by differences in film thickness, which were not well controlled during deposition. Sorption/desorption rates for vapors in C8 were apparently more rapid, resulting in less tailing than with sensors coated with other MPNs. The bar charts presented in Figure 2.6 reveal some differences in the pair-specific correlations of the normalized response patterns from peak-maxima and peak-area sensitivities. Normalized peak-maxima sensitivities were used to construct a PC score plot for qualitatively assessing the diversity of the array responses among these six vapor pairs. This is presented in Figure 2.7. As shown, the projected vectors of all three of the paired vapors considered are well separated, and the inter-vapor distances are consistent with the values of ρ and *ED* given in Table 2.1 and Figure 2.6.

Within each vapor pair, the elution order remained the same under all conditions: MIBK, OCN and NET were always the first to elute. All sensors exhibited tailing peak profiles for all vapors. To quantify the extent of tailing, the asymmetry factors (AF) presented in Table 2.2 were calculated for each vapor-sensor combination. The HME sensor, with AF values ranging from 2.1 to 4.1, consistently exhibited the most tailing, and the C8 sensor, with AF values from 1.1 to 1.5, consistently exhibited the least tailing. For reference, the AF values for the FID (also shown) ranged from 0.9 to only 1.2, despite being downstream from the array. Tailing was the greatest for the polar vapors MIBK and NET for all sensors. Note that reversing the position of the sensors in the flow path had no effect on tailing, which indicates that it was not due to any mixing anomalies in the detector cell. The larger AF values for the HME sensor may be due, in part, to its having a thicker coating film, but it appears that the affinity for polar vapors also contributes.

Of greater importance than the extent of tailing, however, was the *difference* in the extent of tailing among the sensors for a given vapor; ratios of AF values were as high as 2.9 and as small as 1.8 among the sensors for a given vapor. This, in turn, results in a change in the response pattern across the span of a peak, as discussed in more detail further below.

One additional factor is embedding of one peak entirely within the profile of another, which would violate the assumption in EFA that the first compound to elute is also the first to finish eluting. For Gaussian peaks, embedding should not occur for R_s = 1.0 or 0.5 under any of the *RRR* conditions considered here, whereas for R_s = 0.1, embedding would be expected at an *RRR* ≤ 1:5 for the first eluting component and *RRR* ≥ 5:1 for the second eluting compound. Clearly, embedding would be more prevalent at a given nominal R_s value in cases where the first peak tails significantly. Thus, embedding of TOL (in MIBK) and CHX (in NET) would occur when these were the minority components of a composite peak at R_s = 0.1 and *RRR* > 2.5:1, and embedding of BAC (in OCN) would occur at R_s = 0.1 and *RRR* > 5:1.

2.3.2 Additivity of responses for composite peaks

In all MCR methods it is assumed that the response to the two vapors in a composite peak is equivalent to what the sum of the responses to each vapor would have been if measured individually. To test for response additivity, for each test atmosphere containing a binary mixture, the peak areas obtained from the mixture components at the lowest elution temperature, at which they were completely resolved (i.e., R_s > 4), were summed and used as reference values. The composite peak areas from subsequent analyses of the same test atmosphere in which the peaks overlapped to varying extents (i.e., R_s = 0.1, 0.5, 1.0) were then compared to these reference values for each sensor. A focus was placed on the binary mixtures at *RRR* = 1:1 because samples at this value of *RRR* would be the most sensitive to any fractional deviations from additivity. To account for variations in the injected mass of replicate samples taken from a given test atmosphere, each sensor peak area value was divided by the corresponding FID peak area value for that sample and then multiplied by the average FID peak area for all samples from a given bag. Results are summarized in Table 2.3. The average difference in peak areas among all sensors was 0.8% and the range of individual differences spanned from only -4.1 to 4.6% for the 36 cases considered. This confirms that the presence of a second vapor does not affect the response to another vapor over the ranges of sorbed masses under consideration. To our knowledge, this is the first systematic testing of response additivity for this class of sensors.

2.3.3 Intra-peak pattern fidelity

EFA entails a series of progressive (evolving) analyses across the span of each peak and implicitly assumes that response patterns remain constant. In light of the differential tailing discussed above, the extent of pattern distortion arising from differences in t_R and *AF* among the sensors for a given analyte peak was evaluated. A representative analysis is summarized in Figure 2.8a, which shows the superimposed traces from all four sensors for a 200-ng injection of NET prior to any processing (other than baseline correction). There are small differences in t_R (0.05-0.5 sec) and rather large differences in tailing (HME>DPA>OPH>C8; see Table 2.2). As shown by the bar chart patterns and accompanying values of ρ and *ED* generated at the indicated locations across the peak in Figure 2.8a, the pattern is fairly stable over the first half of the peak. Beyond the maximum, however, the differential tailing leads to progressively greater pattern distortion. The C8 and DPA sensors return to baseline well before the OPH and HME sensors. Using the pattern from the (aligned) peak maxima as the reference, ρ decreases from 1 to 0.63 and *ED* increases from 0.03 to 0.98 among the instantaneous patterns in the right-hand portion of the peak.

The extent to which patterns were distorted among all six vapors can be summarized in terms of the average *ED* values across the entire span of a peak, which were 0.96, 0.85, 0.99, 0.83, 0.85, and 1.04 for MIBK, TOL, OCN, BAC, NET, and CHX, respectively, for representative injection masses of each. Note that these *ED* values approach or exceed the *ED* values separating the normalized patterns (derived from the aligned and preprocessed peak maxima) of the members of a pair (Table 2.1). Although most of the intra-peak distortion occurs in the latter part of the peak (~40% of the area) and the pattern extracted by EFA is a weighted average of the instantaneous patterns across the entire span of the peak, this is clearly an unstable and undesirable situation.

To address this problem, t_R values were adjusted to align the four peak maxima and then a boundary was placed on the retention time interval at the point where the sensor giving the least tailing (i.e., C8) returned to baseline. For the other three sensors a new baseline was established by connecting the start of the peak with the point on the tail corresponding to this interval boundary. These initial and final time points were set to zero for each trace to establish a new baseline. The peak maxima and area were then recalculated on the basis of the new (common) baseline.

Figure 2.8b shows the result of performing these pre-processing steps for NET. As shown, this greatly reduced, but did not eliminate, the extent of pattern distortion across the peak. Applying these preprocessing steps to all of the individual-vapor profiles, the *ED* between (aligned) peak-maxima sensitivity pattern and the average of the normalized response patterns determined across the span of the peak dropped from 0.96 to 0.24 for MIBK, from 0.85 to 0.35 for TOL, from 0.99 to 0.31 for OCN, from 0.83 to 0.27 for BAC, from 0.85 to 0.28 for NET, and from 1.04 to 0.35 for CHX. The reduction in pattern distortion is similar among all of the test vapors, but is a bit less for CHX, OCN and TOL because the influence of the tailing HME sensor remained relatively high for these vapors.

A dilemma arises for the composite binary peaks: it is not possible to specify the point at which the first peaks finish eluting in order to truncate the peaks as done in the individual-vapor cases discussed above, because it would depend on the degree of resolution and the relative contribution of the first peak to the overall pattern. An approximate solution was required. The approach taken was to adjust the baselines in the same manner as done with the individual-vapor peaks but for the composite peak as a whole. Thus, the end of the composite peak was truncated at the t_R value corresponding to the end of the most symmetric peak (i.e., C8) and a new baseline was drawn from the start of the peaks to this point on the trailing side of the composite. After this adjustment, the peaks all had the same starting and ending t_R values, and the degree of pattern distortion was minimized.

2.3.4 Rank determinations

In most spectrometric detectors, the number of wavelengths or fragments used far exceeds the number of components being analyzed, and noise levels are minimized by averaging over many effective measurements. In contrast, with a 4-sensor array, the number of sensors barely exceeds the number of components being discriminated, and noise levels are averaged over a relatively small number of effective measurements. Differentiating the net signal from the noise with such a sensor array for the purpose of rank analysis is therefore more challenging; there are relatively few outputs upon which to establish an eigenvalue noise threshold (note also that, with a 4-sensor array, the maximum possible rank is mathematically limited to four). To address this, analyses of the individual-component (calibration) chromatograms were performed to empirically establish an eigenvalue noise threshold above which the change in log (eigenvalue) was attributable to a bonafide peak.

From the plots of log (eigenvalue) vs. t_R for all six vapors, a common noise threshold of 1.25 was established. By use of this threshold, the ranks of the binary composite peak profiles were determined, as shown in Table 2.4. At R_s = 0.1 the rank was correctly determined in 17 of the 21 (81%) composite peaks, and at R_s = 0.5 or 1.0 the correct rank was found for 40 of the 42 composite peaks (95%). Results at R_s = 0.5 and 1.0 were identical. All of the errors led to a rank of one, most (4 out of 6) occurred for MIBK+TOL, and most (4 out of 6) were for R_s = 0.1. For MIBK+TOL at *RRR* = 1:1 and R_s = 1.0 and 0.5, the second log (eigenvalue) traces fell only slightly below the threshold and visual inspection of the composite peak profile clearly indicated more than one chemical component. For the other rank errors, the determinations were unequivocal and were most likely due to pattern similarity for the remaining MIBK+TOL cases and to embedding of the minority component for the two NET+CHX cases.

2.3.5 Fidelity of extracted patterns

Notwithstanding the errors in rank determinations, initial EFA estimates of concentration profiles and response patterns assumed a rank of two. An example of the output from the EFA-ALS algorithm is shown in Figure 2.9 for NET+CHX. Figure 2.9a shows a set of preprocessed chromatograms of a binary mixture of NET and CHX. Figure 2.9b shows the extracted relative concentration profile obtained by EFA-ALS (informed mode), and Figures 2.9c and d present the extracted response patterns of each pair component alongside the library reference pattern (derived from peak maxima). The ED values between extracted and library patterns were 0.11 for both vapors. For this particular case, the *ED* values met both the *ED*-proximity and *ED*-threshold criteria, and the quantification errors were -0.4% and -0.2%, for NET and CHX respectively.

Table 2.5 summarizes the results of EFA-ALS analyses of the entire data set in blind mode. The extracted-pattern fidelity was sufficient to yield correct assignments of identity in the vast majority of cases (112 out of 126; 89%) using the simple *ED*-proximity criterion. Even for MIBK+TOL, only four errors (10%) occurred over the entire range of R_s and *RRR* values. In all but two cases, the error in assigned identity occurred when the vapor was the minority component in the composite. Results for OCN+BAC were also quite good, with only two errors, both of which were for OCN at a low relative concentration. That OCN was mis-assigned at R_s = 1.0 is surprising given that it is the first eluting component of the pair. The errors obtained for CHX in the NET+CHX pair are also remarkable, particularly at the larger values of R_s. Examination of the extracted relative response patterns revealed that the contributions from HME to the CHX patterns were significantly higher than those in the library pattern, exceeding the contribution from C8 in several cases. Apparently, even at R_s values of 1.0 and 0.5, EFA cannot avoid distortion of the (partially embedded) CHX peak by the long tail of the HME peak for NET, despite the preprocessing steps performed to minimize this problem.

As shown in Table 2.5, however, many of the *ED* values are >> 0.20 and, if the more rigorous *ED*-threshold criterion for matching is applied, then only 33% (41 of 126) of the assignments were correct: 12% for MIBK+TOL, 45% for OCN+BAC, and 40% for NET+CHX. The majority of correct assignments (27/41, 66%) occurred for the predominant component of the mixture. Overall, *ED* values were generally larger for the second eluting compound, consistent with distortion arising from overlap by, or embedding within, the tail of the first peak.

Table 2.6 shows the results of EFA-ALS analysis in informed mode. The *ED* values between extracted and calibrated patterns (vectors) decreased by 0.20, on average, from those in blind mode, and the differences in *ED* values of the first and second components decreased. The correct assignment rate increased to 98% (124 of 126) on the basis of the simple *ED*-proximity criterion and to 54% (68 of 126) if the *ED*-threshold criterion is imposed. Notably, the large *ED* values for CHX at *RRR* = 5:1, 10:1, and 20:1 in blind mode were significantly reduced in informed mode. The 58 assignments that did not meet the *ED*-threshold criterion were distributed in accordance the pattern similarity of the pair members: 39 (67%) for MIBK+TOL, 14 (24%) for OCN+BAC, and 5 (9%) for NET+CHX. NET+CHX was the only pair for which the assignment errors showed a dependence on R_s, with the average *ED* reduced from 0.25 to 0.09 on going from $R_s = 0.1$ to $R_s = 1.0$. The improvement reflects the fact that the informed mode analyses circumvent pattern extraction errors by EFA.

2.3.6 Quantification

Tables 2.5 and 2.6 also present the errors in the component masses estimated from the extracted peak profiles on the basis of peak-maxima calibrations. As mentioned above, results were based on the MSS, rather than on the average or median of all sensors in the array. For assessing the results, an arbitrary benchmark of ±30% error in the estimated mass of each component, relative to that obtained (from the MSS) from the calibration library, was used. Estimates exceeding this benchmark are presented in bold typeface in Tables 2.5 and 2.6.

In blind mode (Table 2.5), only 54% (68/126) of the mass estimates had errors less than the benchmark error value, and the number of errant cases decreased in the order MIBK+TOL>OCN+BAC>NET+CHX. In only 3 of 21 samples were both of the components of the MIBK+TOL composite accurately quantified. The largest errors were observed for (first-eluting) OCN when it was the minority component in the OCN+BAC composite, regardless of the R_s value. Inspection of the extracted patterns revealed that a significant fraction of the C8 sensor response to BAC had been attributed to the OCN, and since C8 is the MSS for OCN, this led to large overestimates in the OCN concentration. Since embedding of the OCN peaks within the larger BAC peaks would only occur at $R_s = 0.1$, this factor does not explain the error.

In general, errors in quantification of the majority component were smaller and less frequent than the errors of the minority component and there was a trend toward underestimation of the former and overestimation of the latter. The quantification errors did not show a particularly strong dependence on R_s for any of the pairs (in either mode), but was significantly increased (in both modes) when the *RRR* exceeded 5:1 or 1:5. OCN+BAC was the only pair showing a discernible correlation between pattern fidelity and quantification accuracy. For this pair, across all *RRR* and R_s, a weak linear trend was apparent between *ED* and quantification error. The trend was positive for OCN and negative for BAC, with $r^2 > 0.69$.

In informed mode (Table 2.6) 75% (95/126) of the sample mass estimates fell within the benchmark of ±30% error. The increase, relative to blind mode, follows from the improvement in the accuracy of extracted patterns obtained in informed mode. The trends noted for blind mode persisted with informed mode, but there were fewer errors and the magnitudes of the errors were generally reduced. Notably, the errors in quantification for OCN remained extremely high when it was the minority component.

2.3.7 Comparison of 4 vs. 3 CR array

The most obvious explanation for the relatively poor performance of the EFA-ALS algorithm with respect to both pattern extraction and quantification is the differential tailing of HME and OPH (though to a lesser extent) relative to C8 and DPA, which caused excessive pattern drift across the peak. This drift necessarily broke one of the key assumptions of EFA and

ALS (and indeed all bilinear data algorithms), as discussed in Chapter 1 Section 1.2.9, that the spectra or patterns for an analyte remain constant. One hypothesis for resolving this problem was to omit the tailing trace(s), and utilize only the sensors whose typical peak asymmetries were similar to one another (i.e. eliminate traces with excessive or unusual tailing). To test this hypothesis, one case (NET + CHX at RRR = 20:1 and Rs = 0.1) was analyzed a second time in informed mode without the HME trace, using only the C8, DPA and OPH sensor data (effectively creating an abbreviated 3 CR array).

A comparison of the performance of the standard 4 CR array and the abbreviated 3 CR array is presented in Figure 2.10. Evident from 2.10c, (and Table 2.6) the pattern for NET is correctly extracted under these conditions using the 4 CR array; NET is the majority component and elutes first (less affected by tailing) here, so these results are expected. The pattern for CHX, however, is not correctly extracted; from Figure 2.10d it is evident that the algorithm attributes the majority of the tailing HME to the second eluting component, yielding an ED of 1.20 (Table 2.6) in comparison with the library pattern for CHX. The pattern matching values for the 4 CR array are presented in 2.10g, in units of ρ. In comparison, the 3 CR array yields an equivalently accurate extracted pattern for NET (Figure 2.10e) and a far more accurate extracted pattern for CHX, shown in 2.10f. Comparing the accuracy of extraction between the 4 CR-array and the 3 CR-array (Figure 2.10g and 2.10h, respectively), it is evident that the 3 CR-array is superior, supporting the hypothesis that omitting tailing sensors from EFA-ALS will improve the accuracy of pattern extraction.

2.4 Conclusions

This is the first report on the application of MCR to experimental data from a microsensor array employed as the detector for a GC. In delineating the methodological details of the hybrid EFA-ALS algorithm used here, several important factors relevant to the implementation of multivariate data analysis for this application were characterized, including the pattern similarity, relative concentration, chromatographic resolution, and peak asymmetries of the components of the binary peak composites

The general finding that the response to two vapors is additive confirms that this critical assumption of EFA can be met for MPN-coated CR sensors. The extent of response pattern distortion across the span of the peaks observed was unexpected, and our expedient approach to resolving this in the binary composite peaks was inherently approximate; the residual distortions undoubtedly contributed to decreases in the fidelity of extracted response patterns. This could pose a serious impediment to the general utility of EFA in this type of application. Adjusting MPN film thicknesses or operating conditions might help to minimize this phenomenon. Alternative EFA algorithms that are more resilient to pattern distortion might also be applied.[23]

EFA was able to confirm the number (and elution order) of components in composite peaks in the vast majority of cases. Yet, EFA-ALS in blind mode, faltered in quantitatively analyzing many of the binary composites under the conditions examined. Due to these large quantitative errors, we would not recommended utilizing “blind” mode for quantification of any vapor pair combination in field analysis. This reflects the limitations of the CR array in generating data of sufficient diversity, as well as the difficulty in applying EFA-ALS to a low-dimensional data set with time-varying response patterns. Results suggest that vapor pairs having response patterns with ρ values ≥ 0.85 (perhaps lower) are too highly correlated to be effectively analyzed. Although performance was sensitive to R_s, it was much more sensitive to *RRR*, with *RRR* values < 1:5 or > 5:1 being problematic, especially for the minority component. Under certain circumstances however, such as when pattern similarity is sufficiently low and relative concentrations are near 1:1, reasonably accurate quantification is possible in “informed” mode.

2.5 References

[1] C. Jin, P. Kurzawski, A. Hierlemann, E. T. Zellers, Evaluation of multitransducer arrays for the determination of organic vapor mixtures, *Anal. Chem.* 80, 227-236, 2008.

[2] J. Park, W. A. Groves, E. T. Zellers, Vapor recognition with small arrays of polymer-coated microsensors: a comprehensive analysis, *Anal. Chem*. 71, 3877-3886, 1999.

[3] M. D. Hsieh, E. T. Zellers, Limits of recognition for simple vapor mixtures determined with a microsensor array, *Anal. Chem.* 76, 1885-1895, 2004.

[4] M. D. Hsieh, E. T. Zellers, Adaptation and evaluation of a personal electronic nose for selective multivapor analysis, *J. Occup. Environ. Hyg.* 1, 149-160, 2004.

[5] Y. Qin, Y. B. Gianchandani, A facile, standardized fabrication approach and scalable architecture for a micro gas chromatography system with integrated pump, *Proc., 17th Intnl. Conf. Solid-State Sensors, Actuators, and Microsystems, Transducers '13* Barcelona, June 16-20, 2755-2758, 2013.

[6] M. Li, E.B. Myers, H.X. Tang, S.J. Aldridge, H.C. McCaig, J. J. Whiting, R. J. Simonson, N. S. Lewis, M. L. Roukes, Nanoelectromechanical resonator arrays for ultrafast, gas-phase chromatographic chemical analysis, *Nano Lett.* 10, 3899-903, 2010.

[7] P. R. Lewis, R. P. Manginell, D. R. Adkins, R. J. Kottenstette, D. R. Wheeler, S. S. Sokolowski, D. E. Trudell, J. E. Byrnes, M. Okandan, J. M. Bauer, R. G. Manley, G. C. Frye-Mason, Recent advances in the gas-phase MicroChemLab, *IEEE Sens. J.* 6, 784-795, 2006.

[8] C.-J Lu, W. H. Steinecker, W.-C Tian, M. Agah, J. A. Potkay, M. C. Oborny, J. Nichols, H.K.L. Chan, J. Driscoll, R. D. Sacks, S. W. Pang, K. D. Wise, E. T. Zellers, First-generation hybrid MEMS gas chromatograph, *Lab Chip* 5, 1123-1131, 2005.

[9] Q. Zhong, W. Steinecker, E. T. Zellers, Characterization of a high-performance portable GC with a chemiresistor array detector, *Analyst* 134, 283-293, 2009.

[10] S. K. Kim, H. Chang, E. T Zellers, Microfabricated gas chromatograph for selective determination of trichloroethylene at sub-parts-per-billion concentrations in complex mixtures, *Anal. Chem.* 83, 7198-7206, 2011.

[11] P. J. Chapman, F. Vogt, P. Dutta, P. G. Datskos, G. L. Devault, M. J. Sepaniak, Facile hyphenation of gas chromatography and a microcantilever array sensor for enhanced selectivity, *Anal. Chem.* 79, 364-370, 2007.

[12] W. R. Collin, G. Serrano, L. Wright, H. Chang, N. Nuñovero, E. T. Zellers, Microfabricated gas chromatograph for rapid, trace-level determinations of gas–phase explosive marker compounds, *Anal. Chem.*, 86, 655-663, 2014.

[13] C. J. Lu, J. Whiting, R. D. Sacks, E. T. Zellers, Portable gas chromatograph with tunable retention and sensor array detection for determination of complex vapor mixtures, *Anal. Chem*. 75, 1400-1409, 2003.

[14] C. Jin, E. T. Zellers, Chemometric analysis of gas chromatographic peaks measured with a microsensor array: methodology and performance assessment, *Sensor Actuat. B-Chem.* 139, 548-556, 2009.

[15] M. P. Rowe, K. E. Plass, K. Kim, C. Kurdak, E. T. Zellers, A. J. Matzger, Single-phase synthesis of functionalized gold nanoparticles, *Chem. Mater.* 16, 3513-3517, 2004.

[16] L. Wright, E. T. Zellers, A nanoparticle-coated chemiresistor array as a microscale gas chromatograph detector for explosive marker compounds: flow rate and temperature effects, *Analyst*, 138, 6860-6868, 2013.

[17] E. Covington, F. I. Bohrer, C. Xu, E. T. Zellers, Ç. Kurdak, Densely integrated array of chemiresistor vapor sensors with electron beam patterned monolayer-protected gold nanoparticle interface films, *Lab Chip* 10, 3058-3060, 2010.

[18] J. V. Hinshaw, Anatomy of a peak, *LCGC Europe*, 17 (2004) 216-223.

[19] R. Tauler *Centre d'Investigació i Desenvolupament,* available at http://www.cid.csic.es/homes/rtaqam/, accessed Feb., 2013.

[20] R. Tauler, A.K. Smilde, B. J. Kowalski, Local rank, three-way data analysis and ambiguity in multivariate curve resolution, *J. Chemometr.* 9, 31– 58, 1995.

[21] C.-J. Lin, Projected gradient methods for non-negative matrix factorization, *Neural Comput.* 19, 2756-2779, 2007.

[22] C.-J. Lin *National Taiwan University,* available at http://www.csie.ntu.edu.tw/~cjlin/index.html, accessed July, 2012.

[23] A. de Juan, M. Maeder, T. Hencewics, R. Tauler, Local rank analysis for exploratory spectroscopic image analysis fixed size image window-evolving factor analysis, *Chemometrics and Intelligent Laboratory Systems*, 77, 64-74, 2005.

Table 2.1. List of vapor pairs, measures of pattern diversity, and LODs.

Vapor Pair	ρ[a]	ED[b]	LOD[c] (ng)
MIBK + TOL	0.85	0.33	3.2 3.2
OCN + BAC	0.59	0.79	4.1 2.7
NET + CHX	-0.57	1.28	0.8 4.2

[a] Pair-wise Pearson correlation coefficient for normalized responses of pair members (see Figure 2.6);
[b] Euclidean distance between normalized array response vectors of pair members;
[c] Based on the least sensitive sensor in the array (i.e., DPA for all vapors except NET, for which C8 was the least sensitive).

Table 2.2. Asymmetry factors (AF) from each sensor for the 6 test vapors.[a]

Vapor	AF values [b]				
	C8	DPA	OPH	HME	FID
MIBK	1.4	3.0	1.6	4.1	1.2
TOL	1.3	2.1	1.6	2.5	1.1
OCN	1.1	1.5	1.4	2.0	0.9
BAC	1.3	2.0	1.7	2.9	1.2
NET	1.5	2.0	1.8	3.1	1.2
CHX	1.1	1.6	1.4	2.1	1.0

[a] calculated from calibration samples. Injected masses ranged from 200-300 ng;

[b] ratio of peak widths on either side of the peak maximum (back:front) measured at 10% of peak maxima.

Table 2.3. Deviations from additivity of sensor responses in composite peaks at RRR = 1:1 across all R_s values.

Vapor Pair	Difference (%)				
	C8	DPA	OPH	HME	Average
MIBK+TOL	1.7[a] (6.9[b])	1.9 (11)	4.6 (9.7)	-4.1 (13)	1.0
OCN+BAC	0.6 (4.9)	-2.9 (9.8)	3.6 (6.4)	3.8 (11)	1.3
NET+CHX	3.1 (7.0)	-2.9 (12)	-3.4 (2.9)	4.0 (16)	0.2

[a] calculated as difference in peak area between composite un-resolved cases and sum of individual (fully resolved) calibration responses, divided by the sum of individual (fully resolved) calibration responses, for each pair at RRR = 1:1, averaged across three values of R_s. [b] standard deviation in percent additivity across all R_s conditions.

Table 2.4 Rank of binary composite peaks determined by EFA.

R_s	*RRR* [a]	Number of Components		
		MIBK+ TOL	OCN+ BAC	NET+ CHX
1.0	20:1	-	-	2
	10:1	2	2	2
	5:1	2	2	2
	2.5:1	2	2	-
	1:1	1	2	2
	1:2.5	2	2	-
	1:5	2	2	2
	1:10	2	2	2
	1:20	-	-	2
0.5	20:1	-	-	2
	10:1	2	2	2
	5:1	2	2	2
	2.5:1	2	2	-
	1:1	1	2	2
	1:2.5	2	2	-
	1:5	2	2	2
	1:10	2	2	2
	1:20	-	-	2
0.1	20:1	-	-	1
	10:1	2	2	1
	5:1	2	2	2
	2.5:1	2	2	-
	1:1	1	2	2
	1:2.5	2	2	-
	1:5	2	2	2
	1:10	1	2	2
	1:20	-	-	2

[a] RRR values are approximate. The first number in each RRR corresponds to the compound eluting first, i.e. MIBK, OCN, and NET, respectively. A common threshold value of log (eigenvalue) =1.25 was applied to all cases.

Table 2.5. Pattern fidelity and quantification accuracy of profiles extracted by EFA-ALS in blind mode.

R_s	*RRR*	MIBK		TOL		OCN		BAC		NET		CHX	
		ED[a]	Error[b]	ED	Error	ED	Error	ED	Error	ED	Error	ED	Error
1.0	20:1[c]	-[d]	-	-	-	-	-	-	-	0.24	**-32**	**1.27**	28
	10:1	†0.08	**-77**[e]	0.73	**220**	†0.06	-0.1	0.21	**73**	0.29	**-34**	**1.29**	**65**
	5:1	†0.09	**-75**	0.74	**150**	†0.07	-0.2	†0.20	**45**	0.41	-12	**1.31**	**86**
	2.5:1	0.86	**-84**	0.70	**35**	†0.04	3.7	0.29	20	-	-	-	-
	1:1	0.46	-3.4	0.54	**35**	†0.07	7.9	0.24	16	0.23	1.1	†0.08	1.4
	1:2.5	0.91	**110**	**0.25**	13	†0.16	**58**	0.50	15	-	-	-	-
	1:5	0.28	-16	0.85	-2.8	0.30	**200**	0.66	-17	†0.10	-9.1	†0.12	2.0
	1:10	**0.29**[e]	2.2	0.82	3.5	**0.63**	**790**	0.80	-14	†0.19	**91**	†0.03	14
	1:20	-	-	-	-	-	-	-	-	†0.20	**79**	†0.02	13
0.5	20:1	-	-	-	-	-	-	-	-	0.93	**-31**	**1.35**	20
	10:1	0.66	**-62**	0.84	**200**	†0.07	-0.7	0.24	**59**	0.94	-25	**1.28**	**49**
	5:1	0.84	**-60**	†0.12	**130**	†0.06	1.8	0.21	**43**	0.68	-32	**1.35**	**44**
	2.5:1	0.82	**-67**	0.71	15	†0.08	5.4	†0.20	19	-	-	-	-
	1:1	0.83	4.6	0.85	22	†0.09	7.4	0.28	-8.6	†0.11	-0.5	†0.18	1.4
	1:2.5	0.59	**95**	†0.11	11	†0.14	**56**	0.42	7.0	-	-	-	-
	1:5	0.56	**-41**	0.80	-8.5	0.29	**180**	0.64	-1.9	0.32	-17	†0.05	6.1
	1:10	0.56	**200**	0.80	-0.4	0.51	**690**	0.67	-14	†0.17	**77**	†0.21	12
	1:20	-	-	-	-	-	-	-	-	0.32	**67**	†0.03	4.8
0.1	20:1	-	-	-	-	-	-	-	-	0.96	**-33**	**1.20**	**390**
	10:1	0.95	**-61**	†0.05	**180**	†0.07	10	0.23	**79**	0.98	-30	**1.16**	**230**
	5:1	0.53	**-62**	0.48	**130**	†0.11	-2.2	†0.15	**60**	0.54	-23	**0.97**	**130**
	2.5:1	0.65	11	0.80	**-86**	†0.13	11	†0.13	26	-	-	-	-
	1:1	0.73	**40**	0.82	21	†0.09	**60**	0.38	-19	†0.05	-17	0.22	3.9
	1:2.5	**0.60**	**55**	**1.14**	20	†0.17	**160**	0.44	-4.2	-	-	-	-
	1:5	0.58	**128**	0.66	-21	0.41	**250**	0.67	-3.6	0.26	-17	†0.08	6.9
	1:10	0.56	**-32**	0.61	2.2	**0.65**	**750**	0.80	-20	0.26	**73**	†0.02	13.8
	1:20	-		-	-	-	-	-	-	0.34	**85**	†0.06	10.6

[a] Euclidian distance between normalized extracted and library patterns. [b] Quantification error (%) on the basis of peak maxima of MSS from extracted profiles. [c] First number corresponds to compound eluting first, i.e. MIBK, OCN, and NET, respectively. [d] Not tested. [e] Bolded ED entries indicate errors in assigned identities on the basis of the ED value in 4-space and bolded error entries indicate values exceeding +/-30% error.

Table 2.6. Pattern fidelity and quantification accuracy of profiles extracted by EFA-ALS in informed mode.

R_s	*RRR*	MIBK		TOL		OCN		BAC		NET		CHX	
		ED[a]	Error[b]	ED	Error	ED	Error	ED	Error	ED	Error	ED	Error
1.0	20:1[c]	-[d]	-	-	-	-	-	-	-	†0.05	-28	†0.00	-2.3
	10:1	0.48	**-48**[e]	0.23	**180**	†0.05	1.2	†0.06	6.4	†0.08	-27	†0.18	5.1
	5:1	0.46	**-28**	0.24	**120**	†0.05	0.8	†0.08	0.7	†0.07	3.5	†0.19	3.7
	2.5:1	†0.20	-28	0.22	17	†0.05	2.4	†0.14	7.7	-	-	-	-
	1:1	0.26	-8.1	0.26	27	†0.07	-1.3	†0.11	8.6	†0.13	7.2	†0.09	0.3
	1:2.5	0.71	-7.6	†0.12	0.4	†0.19	-22	0.37	-4.1	-	-	-	-
	1:5	0.68	**40**	0.56	-13	0.24	**175**	0.57	-17	†0.07	-7.5	†0.03	3.6
	1:10	0.70	**82**	0.56	-8.2	0.50	**749**	0.78	-14	†0.15	**97**	†0.04	15
	1:20	-	-	-	-	-	-	-	-	†0.11	**88**	†0.03	13
0.5	20:1	-	-	-	-	-	-	-	-	†0.03	-30	†0.00	-12
	10:1	0.49	**-39**	0.24	**92**	†0.07	-0.2	†0.07	6.9	†0.07	-28	0.96	-21
	5:1	0.42	-25	0.21	**82**	†0.05	3.5	†0.05	26	†0.06	-2.7	†0.04	-12
	2.5:1	†0.20	-30	0.24	-26	†0.07	6.1	†0.08	13	-	-	-	-
	1:1	0.43	-18	0.34	-0.8	†0.09	-1.7	†0.13	0.4	†0.11	-0.4	†0.11	-0.2
	1:2.5	0.26	-15	0.28	-2.1	†0.16	-17	†0.14	-0.6	-	-	-	-
	1:5	0.47	14	0.56	-15	0.23	**140**	0.52	-1.9	†0.06	-8.6	†0.04	5.3
	1:10	0.29	**110**	0.56	-11	0.44	**670**	0.66	-18	†0.15	**79**	†0.04	15
	1:20	-	-	-	-	-	-	-	-	†0.09	**84**	†0.03	4.8
0.1	20:1	-	-	-	-	-	-	-	-	†0.02	-29	**1.20**	-16
	10:1	0.50	**-61**	0.29	**190**	†0.07	-8.1	†0.12	**46**	†0.02	-28	1.03	-22
	5:1	0.56	**-49**	0.40	**97**	†0.08	0.9	†0.11	20	†0.02	-10	0.88	-10
	2.5:1	0.66	-17	0.58	**-39**	†0.08	15	†0.10	20	-		-	-
	1:1	0.57	-13	0.28	9.9	†0.09	20	0.38	23	†0.05	-17	†0.09	-0.2
	1:2.5	0.59	**43**	**0.64**[e]	7.8	†0.19	28	†0.20	-11	-	-	-	-
	1:5	0.49	**64**	0.58	-13	0.22	**190**	0.47	-3.6	†0.11	-11	†0.03	6.1
	1:10	0.65	**110**	0.56	-11	0.43	**640**	0.68	-20	0.25	**74**	†0.01	14
	1:20	-	-	-	-	-	-	-	-	†0.11	**110**	†0.02	10

[a] Euclidian distance between normalized extracted and library patterns; [b] Quantification error (%) on the basis of peak maxima of MSS from extracted profiles; [c] First number corresponds to compound eluting first, i.e. MIBK, OCN, and NET, respectively; [d] Not tested; [e] Bolded ED entries indicate errors in assigned identities on the basis of the ED value in 4-space and bolded error entries indicate values exceeding +/-30% error.

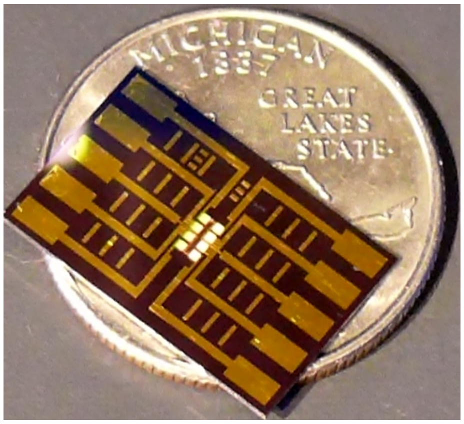

Figure 2.1 Photograph of the CR chip used here, on a U.S. quarter for scale, from reference #12.

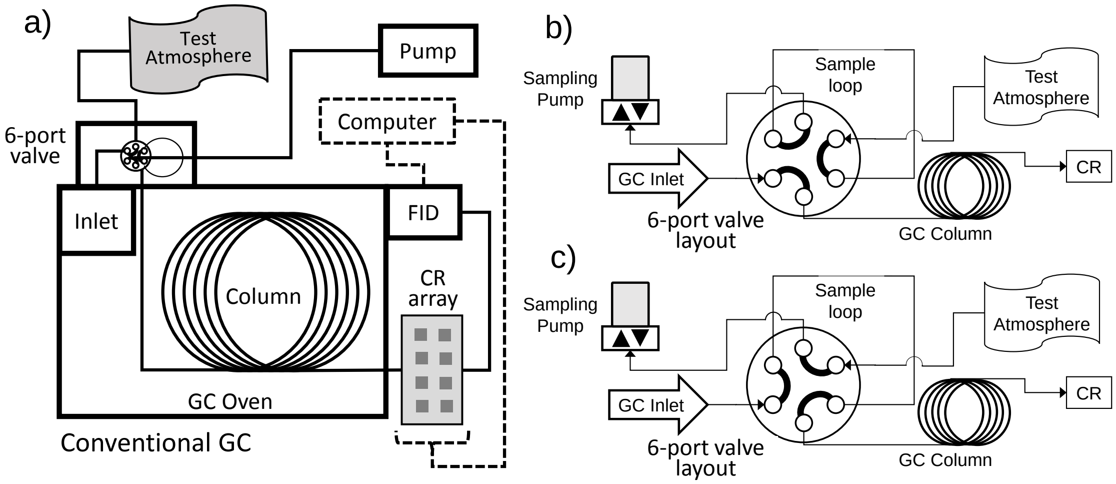

Figure 2.2. a) Schematic of the experimental setup inside conventional GC, with 6-port valve configurations for b) loading and c) injecting.

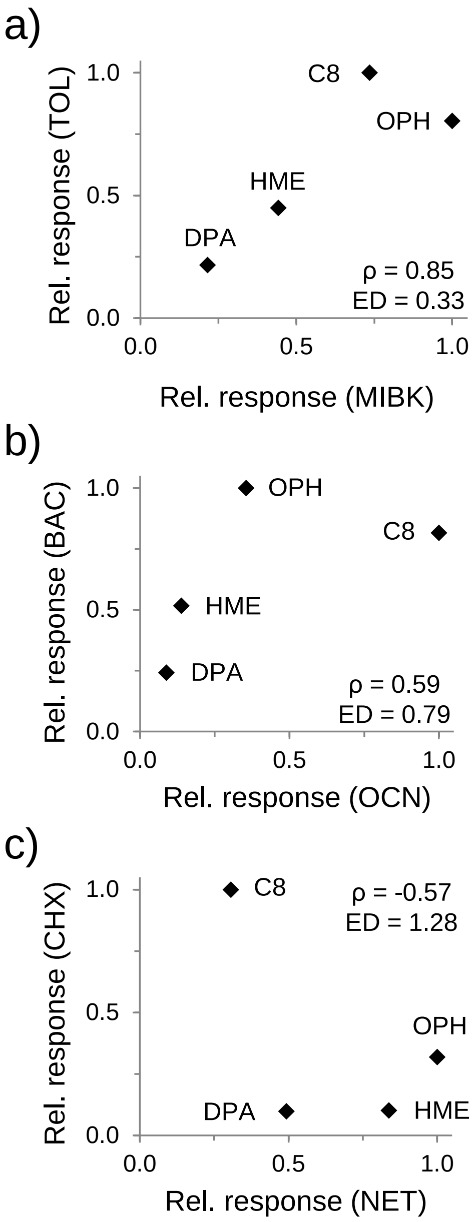

Figure 2.3 Normalized peak maxima sensitivities for each vapor calculation of Pearson correlation; values (ρ) for each plot are 0.85, 0.59, and -0.57 for a), b) and c), respectively. Euclidian distances in 4-space between pattern vectors of each vapor pair were 0.33, 0.79 and 1.28 for a), b) and c), respectively.

Figure 2.4 Calibration curves with forced zero linear regression, from peak maxima. The GC was operated isothermally at 35 °C, at 1.0 mL/min flow rate, with a 25-µL loop injector. Concentrations of the static test atmospheres ranged from 123 to 4810 ppm, as verified by the FID.

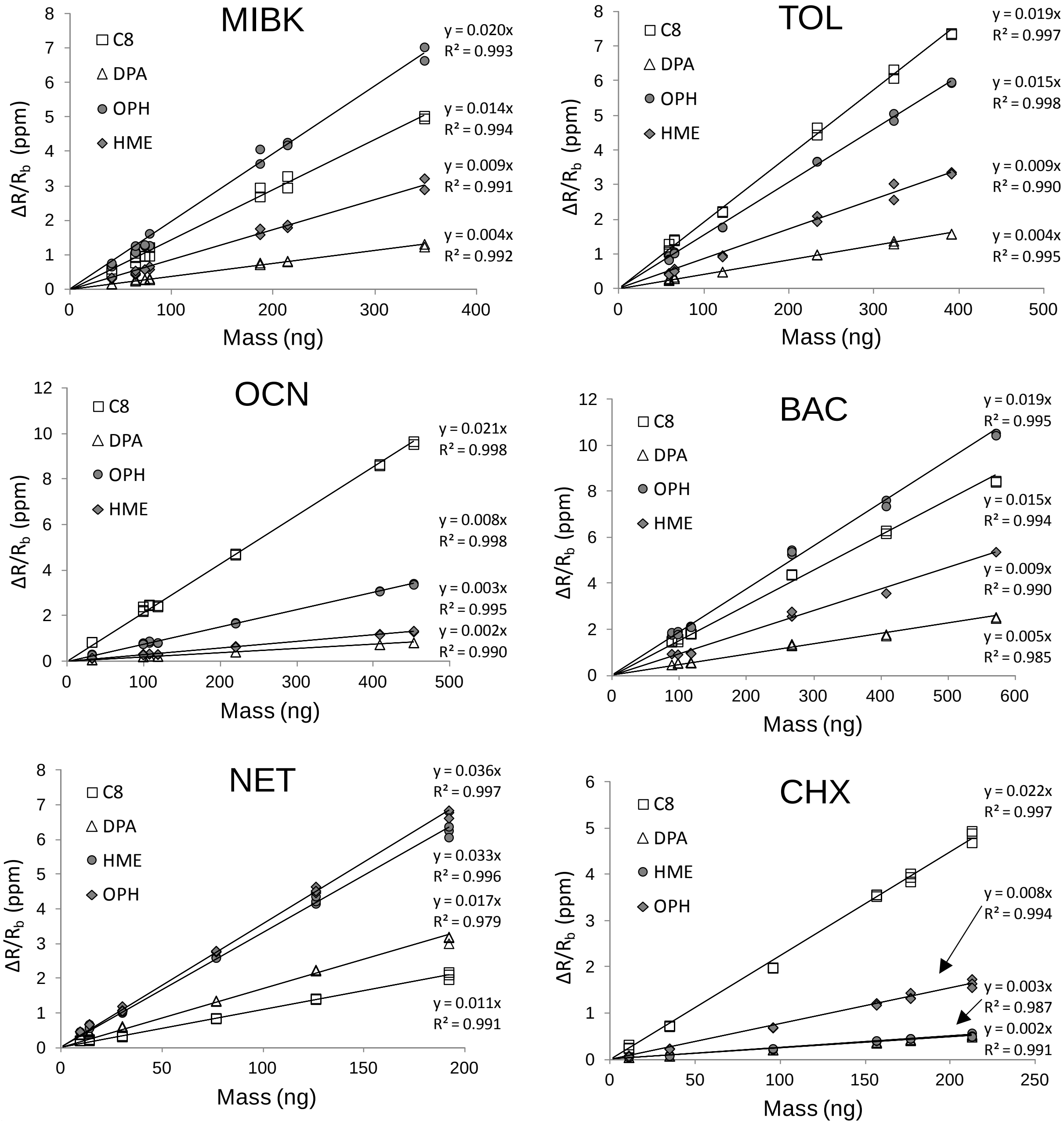

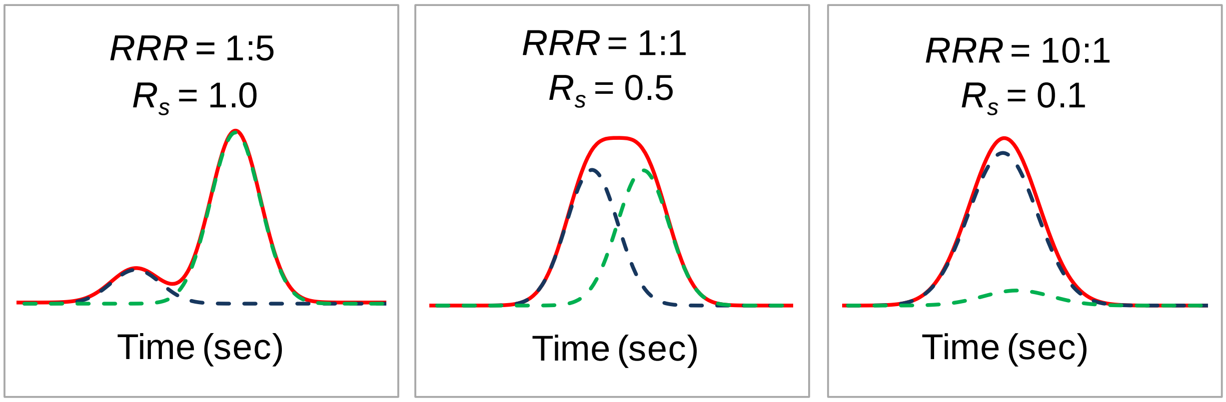

Figure 2.5 Idealized (Gaussian) binary composite chromatograms with values of R_s and RRR selected arbitrarily to illustrate the nature and extent of peak overlap considered in this study. Since actual peaks from the sensors (and FID) are asymmetric to varying degrees, the overlap for a given nominal value of R_s will be greater than shown above.

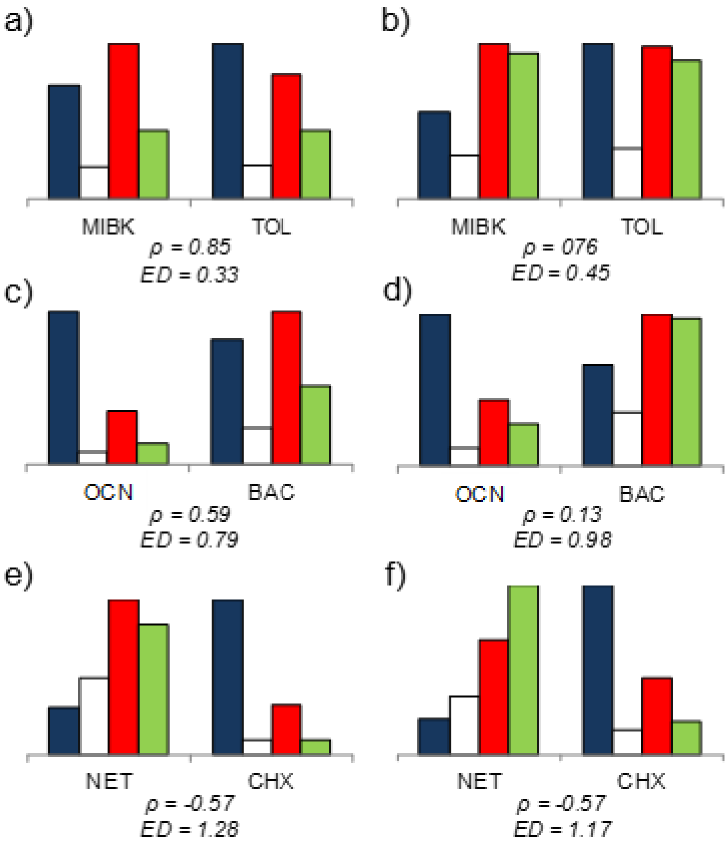

Figure 2.6 Differences in the pattern (l to r: C8, DPA, OPH, HME) correlation for each pair between peak maxima (a, c, and e) and peak area (b, d, f) normalized sensitivity patterns.

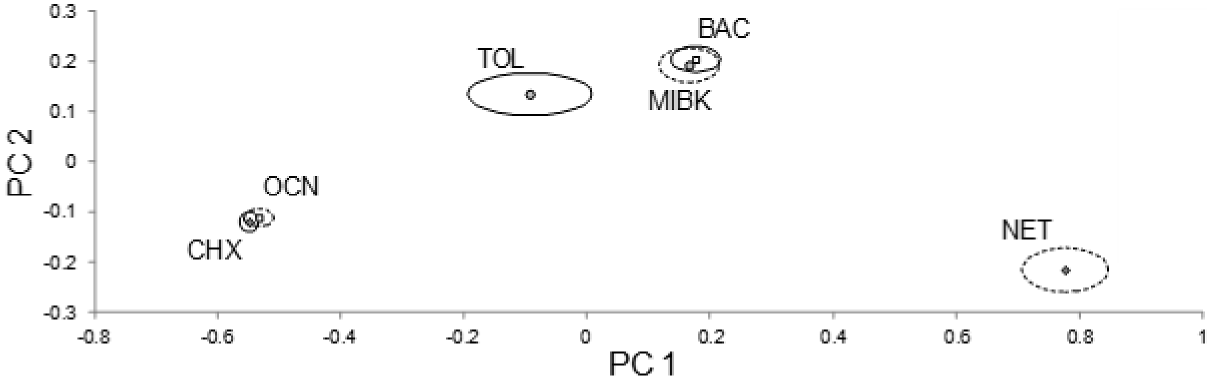

Figure 2.7 PCA plot of the normalized peak maxima sensitivities to each vapor (pairs share same symbol); PC1 explained 87% of the variance and PC2 explained 11% of the variance. The 95% CI boundaries shown around the points corresponding to each vapor were calculated from the variations in normalized calibration sample peak maxima.

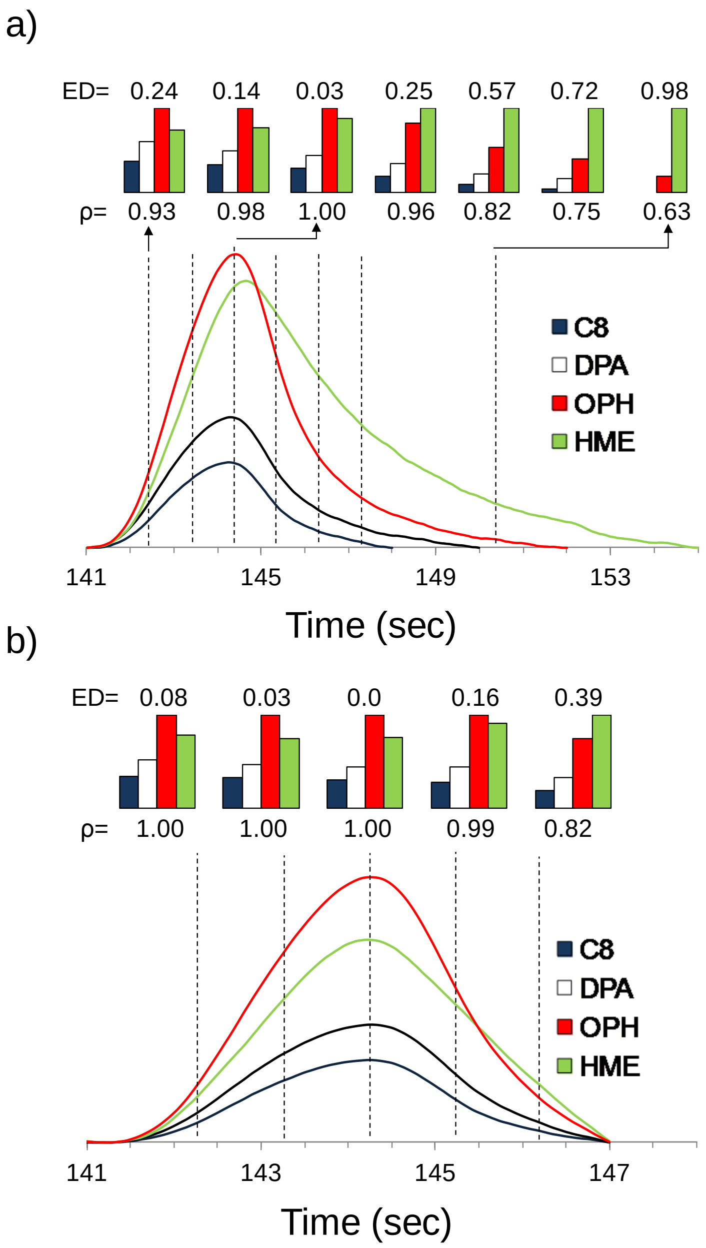

Figure 2.8 Chromatograms for NET from all four sensors in the array a) before and b) after correcting for differential retention times and peak tailing. Normalized patterns at one second intervals across the peak are compared to that at the peak maximum by *ρ* and ED values.

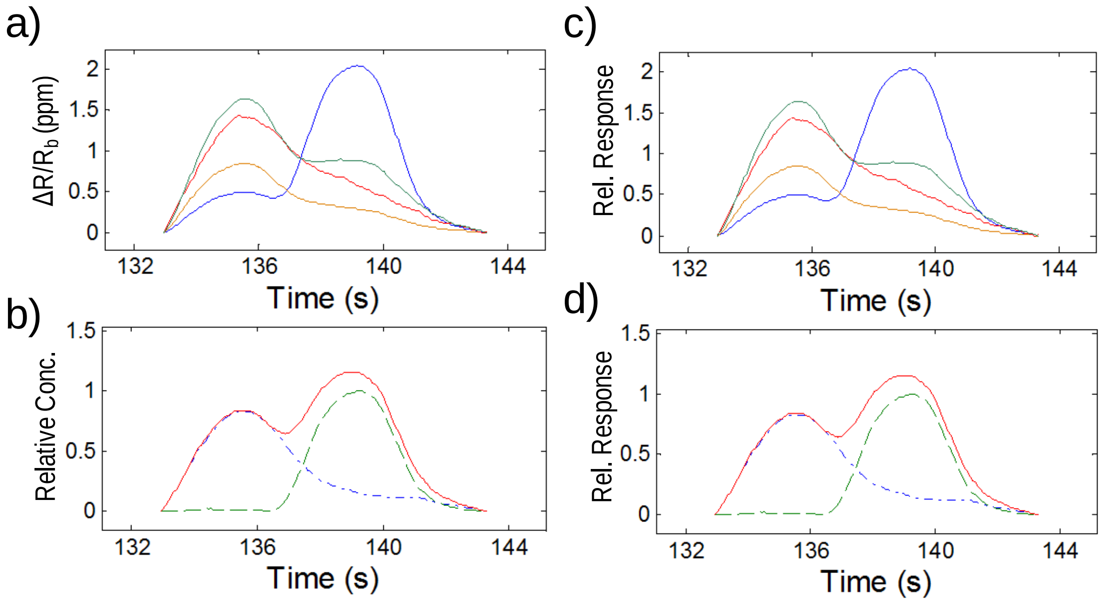

Figure 2.9 Example of the output from the EFA-ALS analysis for NET + CHX at RRR = 1:1 and $R_s = 0.5$; a) Fully preprocessed binary mixture traces, (baseline corrected, retention time adjusted, and windowed); b) extracted unit-less concentration profiles (C matrix) in “informed” mode; and the normalized library and extracted patterns(in order from l to r: C8, DPA, HME, OPH) for c) NET and d) CHX, also collected in “informed” mode.

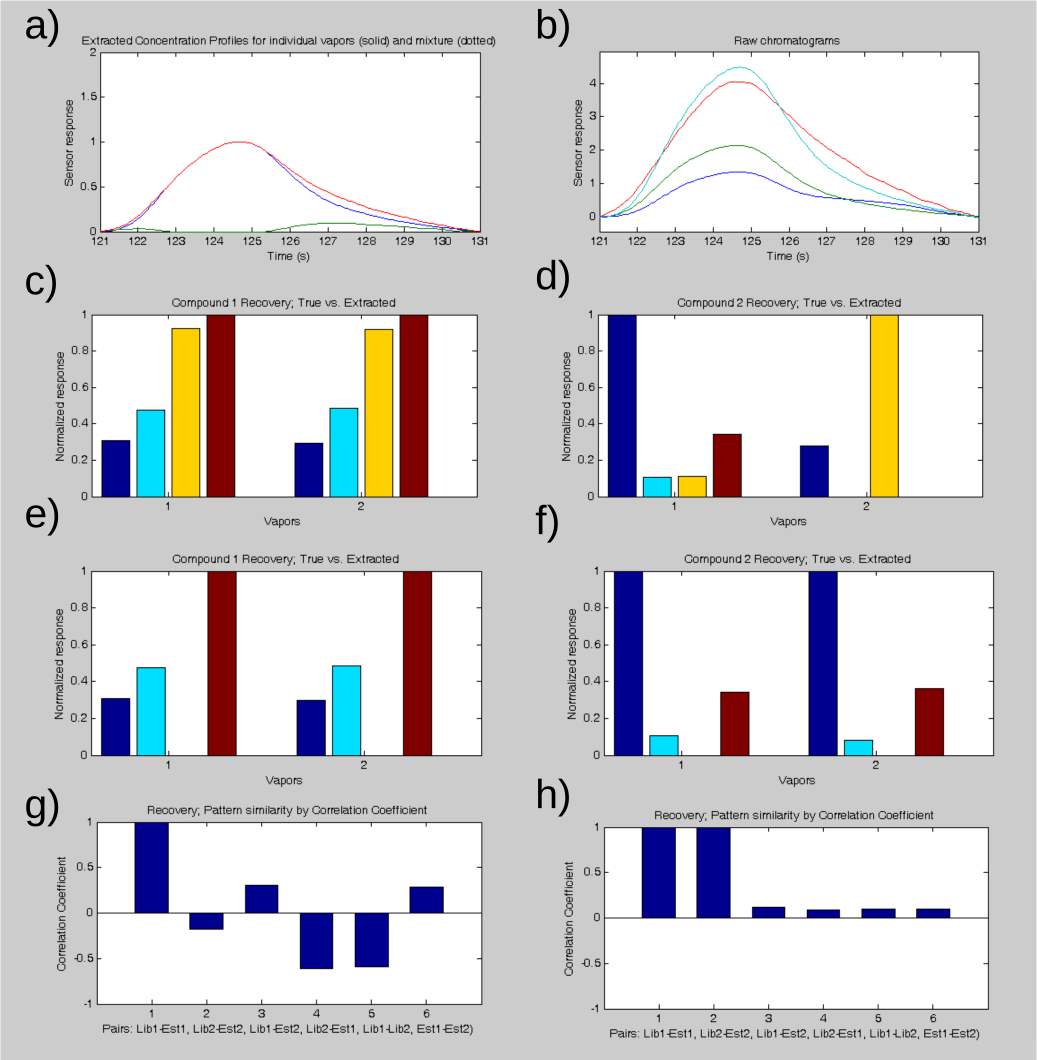

Figure 2.10 Comparison of the output from the EFA-ALS analysis for NET + CHX at *RRR* = 20:1 and R_s = 0.1 in informed mode between the full 4 CR-array and an abbreviated 3 CR-array (with HME omitted). a) Extracted concentration profiles, b) Fully processed binary mixture traces (HME trace shown in red), normalized library and extracted patterns (in order from l to r: C8, DPA, HME, OPH). Results of pattern extraction for c) 4 CR-array for NET, d) 4 CR-array CHX, e) 3 CR-array for NET, and f) 3 CR-array for CHX, with pattern correlation units of g) Pearson correlation and f) Euclidian distance (comparisons from l to r: library NET with extracted NET, library CHX with extracted CHX, library NET with extracted CHX, library CHX with extracted NET, library NET with library CHX, extracted NET with extracted CHX).

Chapter 3

Toward a Microfabricated Preconcentrator-Focuser for a Wearable Micro-scale Gas Chromatograph

3.1 Introduction

In this chapter, we describe the development and characterization of a micro-preconcentrator/focuser (μPCF) for use, ultimately, in the wearable PEMM μGC, introduced in Chapter 1 (Figure 1.7) and discussed in more detail in Chapter 4 (Figure 4.1). The instrument is intended for generalized VOC measurements in industrial workplace environments, and we set out goals of quantitatively analyzing ~10-20 VOCs per measurement at a rate of 6-8 measurements per hour, where the VOCs would all fall within a specified volatility window defined by their vapor pressures; concentrations might range over several orders of magnitude, but for quantification most or all would be at parts-per-billion (ppb) to parts-per-million (ppm) levels. Reconciling the constraints these place on the μPCF with those related to the separation efficiency of the microcolumns and the sensitivities of the microsensor array to be employed required careful assessment of the tradeoffs to achieve satisfactory system-level performance. Using a set of extant μPCF devices, we determined the adsorbent masses and operating conditions that would be required for a next-generation dual-adsorbent μPCF to achieve the desired selective, exhaustive preconcentration and efficient, sharp injection of mixtures of VOCs with vapor pressures, p_v, in the designated range, at concentrations relevant to demonstrating compliance with current occupational exposure limits.

In this study, it was necessary to define, rationalize and address the competing performance criteria affecting the design of the new μPCF that would ultimately serve as both the sampler/preconcentrator and the (thermally desorbed) injector for the system. In the following section, the experimental design developed for this study is explained in terms of the nature and number of VOC compounds, ranges of concentrations, sampling flow rates and times, and desorption flow rates and times. We then proceed to describe our methodology. The results of testing with representative quantities of the adsorbent materials to determine conditions for optimal desorptions/injections are then described. The effects of key variables on the dynamic adsorption capacity are then presented followed by a final performance demonstration with a moderately complex mixture of target and interfering VOCs. Note that all testing reported here used conventional bench-scale GC instrumentation for separation and detection.

3.1.1. Experimental design and rationale

Traditional adsorbent-packed preconcentrators, while ideal for long term exhaustive preconcentration due to their large breakthrough volumes, are ineffective GC injectors because their injection volumes are large and their heating rates are slow, which combine to yield broad injection bands.[1] Conventional GC gas sampling loops can provide sharp injection bandwidths, however they are only suitable in situations where preconcentration is unnecessary (i.e. where air concentrations are high enough that injected masses lie above the LOD of the detector). Incorporating a preconcentration device widens the effective dynamic range of the system, because sampling volumes can be adjusted; lower detection limits can be achieved as well.

Micro-scale preconcentrators can offer a solution in which both preconcentration and injection functions are provided by a single low-power device, which is particularly attractive for portable, battery-powered μGC systems.

In order to specify the types and, ultimately, amounts of adsorbent materials to use in the μPCF described here, defining the nature, number, and concentration ranges of target VOCs was necessary at the outset. In other words, it was necessary to identify the intended application(s) and anticipate possible VOC mixtures the instrument would encounter in the field (the design and operation of the PEMM μGC were presented in Chapter 1, Section 1.2.6, and described in greater detail in Chapter 4). One criterion used to delimit the target VOCs was that they had to fall within a p_v range of ~0.03 to 13 kPa (i.e., 0.2 to ~95 mm Hg). Less volatile compounds would tend to accumulate on internal surfaces and components in the fluidic pathways, and more volatile compounds would be more difficult to trap, separate, and detect given the short column length and limitations with respect to minimum temperature. Selective preconcentration is, in fact, an essential element of all μGC system designs because of the relatively short microcolumns used and limited peak capacities available.

Another criterion used to define the targets was that they had Threshold Limit Values (TLV®) issued by the American Conference of Governmental Industrial Hygienists,[2] which are generally in the high-ppb to mid-ppm range. Thus, we had benchmarks for the range of concentrations on which to focus for this application (e.g., 0.1-2×TLV). The selection of interferences was not so constrained, and for testing purposes we chose to include just a few representative compounds with p_v values higher than the range specified above, in order to demonstrate the degree of selectivity achievable with the μPCF. Less volatile interferences were not included here because we had not yet finalized the design of the pre-trap we intend to include in the PEMM for precluding their capture. As to the number of targets to include, the decision was somewhat arbitrary because the PEMM μGC is intended for a wide variety of targets, the nature and number of which would change with the application. We settled on 14 target VOCs with the expectation that, for many applications, fewer would need to be targeted, but other VOCs within the specified volatility range could be present; that is, VOCs that are targets in one situation could be a potential interferences in another. Table 3.1 lists the set of target VOCs used in this study, along with their p_v values and TLV values.

Establishing limits of detection (LOD) was then necessary in order to specify the minimum air sample volume and the associated volumetric flow rate of the sampling step. Since practitioners often consider 0.1×TLV as a useful level to consider the hazard from a given chemical to be acceptably low,[3-6] we adopted this as a benchmark value. For benzene, which has the lowest TLV among our targets (Table 3.1), this corresponds to 0.05 ppm, and for ethyl acetate, with the highest TLV of 400 ppm, it corresponds to 40 ppm. Previous testing performed with the type of CR array to be used as the PEMM detector (see Chapter 2) indicated that a minimum sample mass of ~5 ng would ensure detection by at least two microsensors in an array for VOCs in the specified volatility range. Assuming exhaustive trapping by our μPCF, then the sample volumes required to achieve the desired LODs would span from 0.040 mL for ethyl acetate to 32 mL for benzene. If we then set a maximum concentration limit of 2×TLV, which would represent an excessively high concentration, this would correspond to 1.0 ppm for benzene and 800 ppm for ethyl acetate. If we further place the constraint that these concentrations should create responses that are 20×LOD, then the required sample volumes would be the same as those quoted above for 0.1×TLV levels.

Note, however, that the range of TLV values assigned to our set of target compounds is 800-fold, and by stipulating a dynamic range of 0.1-2×TLV for each target, the range of desired measurable concentrations spanned by the target list is from 0.05 (benzene) to 800 ppm (ethyl acetate), or 16,000-fold! The corresponding range of masses this represents was deemed infeasible to analyze, much less trap exhaustively on a µPCF in a single sample, and it illustrates an important challenge for this application. In response to this, we are considering two operating modes for the instrument; one when relatively low VOC concentrations would be anticipated, and another when higher concentrations would be anticipated. Pending a more definitive delineation of "low" and "high" concentrations, for the latter, we have set a provisional minimum sample volume of 10 mL, such that, even in the presence of co-contaminants at high concentrations, benzene could still be measured at its TLV with a signal corresponding to 3×LOD. At the same time, the captured masses of other VOCs would not be excessive.

Given the ranges of structures and vapor pressures among our target VOCs, and taking into account previous experience in our group on this topic,[1,7-13] we selected the graphitized carbons Carbopack X (C-X) and Carbopack B (C-B) as suitable adsorbent materials to use in the dual-cavity µPCF. The former has been shown to have the right combination of adsorption capacity and desorption efficiency for VOCs with p_v values from ~4.0 to 13 kPa, while the latter shows similar suitability for VOCs with p_v values from ~0.01 to 4 kPa.[7,8,10,12] Both are hydrophobic.

To specify a *minimum* flow rate required placing a limit on the time allotted for this step in the duty cycle of the instrument. Since we wished to collect measurements over a relatively short time period to capture short-term variations in exposure, but we were not concerned with acute health effects arising from extremely high exposures, we settled on a 10-min cycle time as a provisional specification, i.e., 1 sample every 10 min. Anticipating ~4 min for injection/separation/detection, and ~1 min for re-setting parameters after each analysis, ~5 min could be allotted to sample collection. For sample volumes of 10 to 35 mL, the range of minimum flow rates would then be ~ 2 to 7 mL/min.

The *maximum* flow rate would then be dictated primarily by two factors: the LODs and the values of τ_{safe}, defined in Section 1.2.7. Having set 5 ng as a reasonable minimum sample mass, as shown above, it would require sample volumes between 0.040 - 32 mL to capture such a quantity for measurements at 0.1×TLV for all target VOCs. From previous work with a C-X packed single-cavity µPCF device,[1] a τ value of 20 msec would yield 90% bed efficiency for our most volatile target, benzene (i.e., $\tau >> \tau_{safe}$). For the cavity sizes of the devices available for this study this would correspond to flow rates between 8.5 and 14 mL/min. At these flow rates it would require only a few seconds to a few minutes to capture sufficient mass for reliable analysis of several target VOCs at the concentrations under consideration. Other factors, such as internal flow-path dead volumes that demand somewhat larger sample volumes, place additional constraints on the maximum flow rate. Assuming a similar value of τ is needed to achieve similar bed efficiencies for the less volatile VOCs to be captured in the upstream cavity packed with C-B, then similar constraints on maximum flow rates would apply, and the smaller of the two beds would govern the maximum flow rate.

Of course, the influence of co-contaminants on the breakthrough volumes of target VOCs must also be included in any comprehensive study. Toward this end, the compound expected to have the lowest value of V_b (equation 1.1) for each adsorbent bed would be designated as the "sentinel" for the other compounds, and limits on sample volumes could be set accordingly.[1,7-12]

To ensure negligible carryover of samples from run to run, the desorption efficiency (DE) must be as close to 100% as possible. Desorption bandwidth is also important, as the downstream chromatographic resolution is affected by the sharpness of the injection band. For assessing DE, a focus would naturally be placed on compounds with low p_v values, which are the most difficult to volatilize from the adsorbent surface. For assessing bandwidth, compounds with high p_v values and short retention times would be of greater concern, since they are more difficult to resolve chromatographically.

3.2 Experimental methods

3.2.1 Materials

All test compounds were purchased from Sigma-Aldrich/Fluka (Milwaukee, WI) or Acros/Fisher (Pittsburgh, PA) in >95% (most > 99%) purity and were used as received. Samples of C-B and C-X (60/80 mesh, Supelco, Bellefonte, PA) were sieved to isolate fractions with nominal diameters of 212-250 μm.

3.2.2 Devices

The dual-cavity μPCF devices used here are designated as μPCF-2 and the single cavity devices are designated as μPCF-1x or μPCF-1b depending on whether they were loaded with C-X or C-B, respectively. As with the μPCF-1 devices, described previously,[1,11,12,14,15] the 4.2-mm × 12.1-mm μPCF-2 chips were fabricated from 500-μm thick Si wafers using deep-reactive-ion-etching to create all features. The central cavity, inlet/outlet ports, and the tee-junction adjacent to one side of the cavity were all 380-μm deep (see Figure 3.2). Cylindrical pillars (150-μm spacing and widths) were added just inside the cavity inlet and outlet to retain adsorbent granules, and to divide the cavity into front and back sub-sections, with volumes of 4.7 µL and 2.9 µL, respectively. The walls of the cavity tapered toward the inlet and outlet to reduce turbulence and promote even distribution of the flow stream. Filling ports etched into the sidewalls of each subsection were used for loading adsorbent granules. A 120-µm thick Pyrex plate was anodically bonded to the top surface at wafer level to seal the tops of the devices. Two Ti/Pt contact pads along with a resistive temperature device (RTD) were evaporated onto the backside of the Si for bulk resistive heating and temperature monitoring, respectively. Devices were then diced into individual chips.

Deactivated fused-silica capillaries were sealed into the inlet/outlet ports using silicone adhesive (Duraseal 1531, Cotronics, Brooklyn, NY). Each device cavity or subsection was filled with sieved adsorbent granules using a gentle vacuum. The µPCF-1 devices were loaded to capacity with either 2.3 mg of C-X or 2.0 mg of C-B. The µPCF-2 device was also loaded to capacity, the larger section with 2.0 mg of C-B and the smaller section with 1.4 mg of C-X. Adsorbent masses were determined by weighing the device with an electronic balance to ±0.1mg before and after loading (note: since C-B has a lower density than C-X, the mass of this adsorbent contained in a given cavity volume is also lower). Devices were then mounted on custom printed circuit boards (PCB) using epoxy (Hysol 1C, Rocky Hill, CT); only the capillaries were bonded to the board to maximize thermal isolation of the device. A rectangular hole in the PCB beneath each device further improved thermal isolation. Al wire-bond wires were used for electrical connections.

3.2.3 Test atmospheres

Test atmospheres were generated by injecting pre-determined volumes of liquid analytes into 10-L Supel-Inert® foil-laminated gas sampling bags (Model 30240-U, Supelco), prefilled with a known volume of clean, dry N_2 from a compressed gas cylinder. Serial dilutions were made to achieve the desired range of concentrations, which were verified by a calibrated bench-scale GC with FID (Model 7890, Agilent Technologies, Palo Alto, CA). For tests performed at high humidity, small volumes of distilled water were added to the bags to achieve the desired humidity levels assuming complete vaporization.

3.2.4 Desorption testing

Three compounds spanning the range of p_v values of the compounds listed in Table 3.1 were chosen for desorption testing: benzene, toluene and n-dodecane. The effects of desorption flow rate, heating period, vapor loading, and split ratio on the desorption efficiency and bandwidth were evaluated for each VOC individually. The experimental setup for desorption testing is shown in Figures 3.1a and b. Analyses were performed using the bench-scale GC-FID. The μPCF was mounted across two ports of a 6-port valve. A suction pump (model UMP015, KNF) was used to load the μPCF by drawing a finite air sample from the test atmosphere through the device at a low flow rate (i.e., 5 mL/min). To desorb the trapped VOCs, the valve was switched to the second position, and N_2 or He from the GC injection port was backflushed through the μPCF while it was heated at ~325 °C/sec to 225 °C and maintained at that temperature for varying amounts of time. This was achieved by applying 42 V across the device and using pulse width modulation with feedback from the RTD at 50 Hz to minimize overshoot and maintain a constant temperature. For μPCF-2, the flow during sampling passed through the C-B bed first, and during desorption it was in the opposite direction.

No column was used for these single-VOC tests; the valve was plumbed directly to the FID via deactivated fused silica capillary, and both were heated to minimize any adsorption during transfer. Where separations were required, a 6-m capillary column (250-μm i.d.; 0.25-μm thick Rtx-1; Restek, Bellefonte, PA) was used. The effect of increasing the desorption flow rate while maintaining a constant flow rate to the detector was explored by splitting the flow downstream from the μPCF using a 'Y' press-tight connector. Split ratios were adjusted using the GC inlet head pressure and lengths of capillary on the vent line to create the appropriate pressure drops. Flows were measured by a miniature bubble-buret meter.

Desorption efficiency was also evaluated as a function of heating time for benzene, toluene and n-dodecane. μPCF-2 was pre-loaded with 250 ng of each analyte individually, sufficient to detect < 1% residual mass with the FID. Desorption at 225 ^{0}C and 3 mL/min was continued for 20, 40, or 60 sec and was followed by another desorption of similar duration after allowing the device to cool to ambient temperature. The area of the first desorption was divided by the sum of the areas from both desorptions (the first desorption and any residual peak from the secondary desorption) to determine the desorption efficiency.

3.2.5 Breakthrough testing

Figures 3.1c and d show the breakthrough testing set-up, which is similar to those presented previously.[7,11] Test atmospheres were drawn through the μPCF and a downstream 25-μL or 250-μL sampling loop using the pump at discrete flow rates between 4 and 10 mL/min. At 30-sec intervals, the six-port valve was actuated to inject the contents of the loop into the 6-m capillary column in the GC oven while the pump continued to draw sample through the μPCF. Devices were cleaned after each exposure by heating to 200 °C for 10 min under N_2 flow.

By convention, the sample volume required for the concentration downstream from the μPCF (C_x) to reach 10% of the inlet concentration (C_o), was used as the metric of the dynamic adsorption capacity of the devices, and is designated V_{b10}. This is considered the maximum sampling volume for exhaustive (quantitative) capture. All V_{b10} values were estimated to the closest 0.5 mL. Breakthrough fractions were determined by comparing the peak areas of samples obtained over the course of each test to those of samples injected directly from the test atmosphere used as the source of the challenge. The μPCF devices were thermostated for all tests by applying pulse width modulation to a 5 V bias to the on-chip heaters.

3.2.6 Data acquisition and management

Device heating functions were controlled, and RTD output data were collected, with a desk top computer using custom LabVIEW software written in-house. Peak parameters, including retention times, areas, heights, and full width at half height (*fwhm*) were measured using Chemstation (Rev.B.01.01, Agilent Technologies). Gaussian peak fitting and calculations of asymmetry factors were performed with OriginPro 9.1 (OriginLab, Northampton, MA). Other data processing, statistical analyses, and graphing utilized Excel (Office 2013, Microsoft).

3.3 Results and discussion

3.3.1 Desorption bandwidth

Figure 3.3 shows the effect of desorption flow rate on the injection band width from μPCF-2 for benzene, toluene, and n-dodecane. Each compound was tested individually, in triplicate, by drawing a 5 mL sample of a test atmosphere containing 3-6 ppm of the compound (~50 ng) through the μPCF at 5 mL/min, reversing the direction of flow, and then heating to 225

°C in < 1 sec and holding for 60 sec. As shown, the *fwhm* values of the desorbed peaks were inversely proportional to flow rate, with a dependence that varied inversely with p_v. The ratios of *fwhm* values at 1 and 5 mL/min were 1.8, 2.4, and 2.7 for benzene, toluene, and n-dodecane, respectively. Benzene consistently gave the sharpest peaks, but at the highest flow rate of 5 mL/min its peak was only slightly narrower than that of toluene, and only 28% narrower than that of n-dodecane.

These trends are consistent with the expectation that more volatile compounds would be more rapidly and completely vaporized by the heat applied, and that compression of the desorption band would occur primarily by the increased rate at which the µPCF headspace volume was swept. The less volatile n-dodecane exhibited behavior indicative of slower or less efficient vaporization, such that the increased flow rate enhanced the rate of desorption as well as compressing the peak. These results are in qualitative agreement with those reported by Whiting and Sacks for a small packed-capillary preconcentrator device.[16]

The inset in Figure 3.3 shows the effect on the *fwhm* values of benzene and n-dodecane of increasing the desorption flow rate further by incorporating an injection split. By venting a portion of the downstream flow stream, sharper injections are possible without altering the flow rate passing through the GC column. For an analytical path flow rate of 3 mL/min and split ratios of 2:1, 5:1, and 10:1 (i.e. desorption flow rates of 9, 18, and 33 mL/min, respectively), the *fwhm* decreased by 33%, 42% and 55% for benzene and by 36%, 40% and 44% for n-dodecane relative to the splitless injection at 3 mL/min.

That the peak width for the more volatile benzene continued to decrease while that for the n-dodecane showed very little change beyond a split ratio of 2:1 indicates that the injection band for benzene continued to be flow rate limited while that of n-dodecane was still partially governed by the slower rate of thermal desorption from the adsorbent surface. For both compounds, the largest change in *fwhm* values occurred between no split and 2:1. Consistent with this split ratio, the observed FID peak areas for benzene and n-dodecane decreased by ~65%, whereas the peak heights decreased by only 50 and 43%, respectively. This reflects the band compression (i.e., focusing) accompanying the increase in flow rate, which at least partially offsets the loss of injected mass with respect to the peak-height sensitivity and, thus, LOD.

Increasing the initial sample volume (and mass) by 5-fold led to an increase in *fwhm* of < 10% for all three vapors at 3 mL/min (splitless). At 1 mL/min the increase was greater, particularly for n-dodecane. Asymmetry factors, calculated at 10% of the peak maximum, were 1.0, 1.8 and 3.1 for benzene, toluene and n-dodecane, respectively, with splitless injection, consistent with the assertion above that thermal desorption speed and efficiency decrease with decreasing p_v value.

For n-dodecane and compounds of similar or lower volatility, on-column focusing can mitigate the effects of injection band broadening and asymmetry,[17] and for compounds of somewhat higher volatility (e.g., toluene), which are not focused at the head of the column, the retention times are long enough to expect reasonable chromatographic resolution. In contrast, for benzene and similarly volatile compounds, injection band broadening has a greater influence on their resolution due to their short retention times. To evaluate the latter, in a subsequent test series, a 6-m capillary column was connected downstream from the μPCF and the chromatographic resolution (R_s) of benzene from a similarly volatile compound, trichloroethylene (TCE), was evaluated as a function of desorption flow rate and injection split ratio. Estimates of R_s (from section 1.2.8, $=\Delta t_R\ [2*(\sigma_a+\sigma_b)]^{-1}$) were calculated from the difference in retention times, Δt_R, and the average standard deviation of the Gaussian profiles fitted to the peaks, σ_a and $\sigma_{a.}$[17]

Figure 3.4a shows results for splitless injections of 50 ng of each compound at each of three flow rates. All peaks fit Gaussian profiles with $R^2 > 0.98$. Interestingly, there was little change in R_s on going from 1 to 3 mL/min; the narrowing of the peaks was accompanied by a commensurate reduction in t_R values. Since the optimal velocity for separations on this type of column corresponds to a flow rate < 1 mL/min, we would have expected a decrease in R_s at the higher flow rate. Evidently, the reduction in the injection band width compensated for the loss in chromatographic efficiency over this range of flow rates. At 5 mL/min, however, the latter factor dominated and there was a significant decrease in R_s, consistent with the data in Figure 3.3 showing relatively little reduction in the injection band width above 3 mL/min.

Figure 3.4b shows the dependence of R_s and sensitivity on the injection split ratio, while maintaining a flow rate of 3 mL/min in the analytical path. The ~linear increase in R_s with the split ratio follows from Δt_R remaining constant while the widths of both peaks decreased at the same rate with increasing desorption flow rate. The tradeoff is a loss in sensitivity from venting large portions of the sample. As shown in Figure 3.4b, the fractional reduction in average peak height was much less than that of average peak area because of the compression of the injection band. In any case, the relative gain in resolution (~1.4 fold) was smaller than the relative loss in sensitivity (~2.5-3 fold) over this range of split ratios, consistent with results reported in ref. 19.

Since the responses of the CR microsensors should show the same trends in sensitivity and resolution as the FID used here,[19,20] these results allow for a rational choice of split ratio on the basis of the specific demands of a particular analysis. That is, for a scenario involving lower concentrations of a less complex VOC mixture, a lower split ratio could be selected in favor of sensitivity, whereas for a scenario with higher concentrations of a more complex VOC mixture, a higher split ratio could be selected in favor of resolution. Of course, the sample volume is another adjustable variable that could impact such decisions (see Section 3.3.3).

3.3.2 Desorption efficiency

Tests were then performed to determine the minimum time period required to remove all traces of analytes from the μPCF during thermal desorption. Once again, benzene, toluene, and n-dodecane were used as the test compounds to span the range of volatility expected of any samples that might be collected. Results are summarized in Table 3.2. Heating for 20 sec was sufficient to desorb >99% of the benzene and toluene, but only 97% of the n-dodecane. For heating periods of 40 and 60 sec, the desorption efficiencies of n-dodecane were 99 and >99%, respectively. Increasing the initial VOC mass loading from 250 ng to 1 μg had no effect on desorption efficiency for benzene and < 1% decrease for n-dodecane. Therefore, 40 sec was deemed sufficient to avoid carryover of any low volatility analytes.

3.3.3 Trapping capacity

Results of initial range-finding breakthrough tests conducted at 30 °C are presented in Table 3.3. On the basis of earlier work,[7,8,12] benzene and toluene were selected as sentinel breakthrough compounds for C-X and C-B, respectively. At 5 mL/min, the average V_{b10} for benzene with the μPCF-1x device was 41 mL and the average V_{b10} value for toluene with μPCF-1b was 31 mL. Increasing the flow rate to 10 mL/min led to a decrease in V_{b10} of ≤ 3% in all cases, which is consistent with operation at $\tau >> \tau_{safe}$ where the flow rate dependence of V_{b10} is expected to be small.[12] Therefore, V_{b10} values at 5 and 10 mL/min were combined in Table 3.3.

Since the larger subsection of the μPCF-2 device holds the same mass of C-B as μPCF-1b (i.e., 2.0 mg), results from the latter are transferrable to the former. Note that previous work has shown that benzene is not retained by C-B,[7,21] and therefore should only be trapped by the downstream C-X bed in μPCF-2. These results demonstrate that, at relatively low concentrations in the absence of co-contaminants, the individual μPCF-1 devices provide ample capacity for benzene and toluene to measure them at concentrations < 50 ppb with the PEMM microsystem, assuming an LOD of ~5 ng (vide supra).

For the next set of breakthrough tests, μPCF-2 was challenged with a mixture of benzene, toluene, ethylbenzene, and xylene (i.e., BTEX), each at its respective TLV concentration except for benzene, which was at 2×TLV to permit reliable quantification of V_{b10}. Replicate tests (n = 3) were performed under both dry and humid (88% relative humidity, RH) conditions in N_2. A representative set of breakthrough curves is presented in Figure 3.5. Average V_{b10} values for the sentinels benzene and toluene were 33 and 90 mL, respectively (RSD < 3%). For ethylbenzene and xylene, V_{b10} was consistently > 150 mL, at which point the tests were terminated. These results confirm that μPCF-2 has sufficient capacity to quantitatively retain BTEX mixtures at relevant concentrations above the 31-mL sample volume necessary to detect benzene at 0.1×TLV.

These results are also consistent with those for individual exposures to benzene and toluene presented in Table 3.3; a significant decrease in V_{b10} for benzene occurred because of the smaller mass of C-X in μPCF-2, despite the lower challenge concentration (i.e., 1ppm vs. 5 ppm), and a significant increase in V_{b10} for toluene occurred because of the downstream C-X bed in μPCF-2, despite the presence of xylene and ethylbenzene. Although it is likely that toluene would start to displace benzene from the C-X by competitive adsorption once it breaks through the C-B bed, a larger decrease in V_{b10} for benzene would have been expected if it were an important factor. In fact, the decrease was less than expected on the basis of the reduction in adsorbent mass (*vide infra*). No changes in V_{b10} were observed for any of the compounds at the higher background humidity level.

The next set of breakthrough tests was designed to characterize capacity at much higher concentrations. In lieu of using a challenge test atmosphere containing a large number of compounds, mixtures of four representative compounds at higher concentrations were used. This permitted measurements at a higher frequency because chromatographic separation times were shorter. For characterizing C-X, a mixture of 2-butanone, benzene, ethyl acetate and toluene was used, and for C-B a mixture of toluene, cumene, 1,2,4-trimethylbenzene and n-dodecane was used. Within a subset, compounds were included that spanned the range of p_v values appropriate for that adsorbent material, although including toluene in the mixture for C-X was actually a more rigorous test, because the vapors intended to be captured on C-X have higher p_v values. The challenge mixtures contained 100, 150, or 200 ppm of each compound. At 200 ppm, the net (composite) mass per unit volume concentration was roughly equivalent to that of all of the target compounds in Table 3.1 at their respective TLV concentrations (note: since n-dodecane has no assigned TLV, a concentration of 10 ppm was assumed).

Table 3.4 shows the measured V_{b10} values as a function of flow rate and temperature for the subset of compounds intended to characterize the performance of the C-X bed. As expected, V_{b10} varied inversely with p_v among the test compounds under all conditions. Values of V_{b10} for the high-p_v interference 2-butanone (p_v = 13.3 kPa) were consistently the smallest observed, never exceeding 7 mL, while the values of V_{b10} for toluene consistently exceeded those of the other compounds by >2 fold. Benzene had V_{b10} values ranging from only 7.5 to 11 mL. For all concentrations at 30 °C there was a very slight decrease in V_{b10} with increasing flow rate as expected. V_{b10} also decreased with the 2-fold increase in C_o, but only for toluene was the decrease > 12% (i.e., ~26%).

The relative insensitivity to flow rate and concentration are both predicted by the Wheeler Model.[12,22] The small concentration dependence reflects the increase in the dynamic adsorption capacity with increasing concentration in the sub-monolayer regime where that model is applicable. The Wheeler Model also predicts the breakthrough volume to increase in proportion to the bed mass. The ratios of V_{b10} for the μPCF-1x and μPCF-2 devices at 200 ppm were, on average, slightly lower than the ratio of adsorbent masses in these two devices (mass ratio = 1.6) for the three more volatile compounds, mostly likely because of competitive adsorption. Since toluene was partially retained on the C-B bed of μPCF-2 it cannot be included in these comparisons.

Temperature had a large impact on V_{b10} for all compounds; an increase from 25 to 40 °C, which corresponds to only a 5% increase on the Kelvin scale (i.e., 313/298) resulted in reductions of 2.5-3.2 fold in V_{b10} among the C-X test compounds. Since diffusion coefficients *increase* with temperature, the loss in capacity must be due to a decrease in the dynamic adsorption capacity, which should vary as $e^{-\alpha T}$, where T is temperature in Kelvin and α is proportional to the enthalpy of adsorption.[23] These results serve to highlight the importance of maintaining the μPCF-2 device at a low temperature and, in particular, to allow it sufficient time to cool down after each injection prior to starting to collect the subsequent sample with the PEMM prototype.

We note that V_{b10} for benzene with μPCF-2 at 30 °C did not reach the benchmark value of 10 mL for any of these high-concentration challenge mixtures, but that it reached 11 mL with μPCF-1x due to the increase in the C-X bed mass. Similarly, the ethyl acetate V_{b10} values, which barely exceeded the benchmark value with uPCF-2, increased significantly with μPCF-1x. Although the V_{b10} estimates obtained by testing with these high VOC concentrations are conservative, affording some margin of safety for cases in which additional compounds of similar or lower volatility might be present, these results led us to conclude that the bed mass of C-X in the next-generation dual-cavity μPCF devices to be installed in the PEMM prototype must be increased to 2.3 mg.

Table 3.5 presents the measured V_{b10} values as a function of flow rate and temperature for the compounds intended to characterize the performance of the C-B. As above, μPCF-1b was used as a surrogate device that held the same mass of C-B as the large subsection of μPCF-2. For these tests only one mixture was used, with each component at 200 ppm. Once again, V_{b10} consistently varied inversely with p_v among the test compounds. Since results at 5 and 10 mL/min were not significantly different, they were combined in Table 3.5. At 30 °C, V_{b10} ranged from 12 mL for the sentinel toluene to > 150 mL for the least volatile n-dodecane. As was found for the tests with C-X, V_{b10} decreased with increasing temperature, but at a much lower rate, decreasing by < 20% in all cases for an increase from 30 to 40 °C. The V_{b10} value for n-dodecane remained > 150 mL under all conditions.

Interestingly, V_{b10} for toluene with C-B decreased by about 2.5-fold relative to the value presented in Table 3.3, which was obtained at a much lower concentration in the absence of co-contaminants. However, even at the high concentrations tested here in the presence of high concentrations of co-contaminants, the V_{b10} value exceeds the 10 mL benchmark value. Of course, as shown in Table 3.5 and Figure 3.5, toluene would be trapped effectively on the downstream C-X bed at larger sample volumes, but this situation should ideally be avoided, because it might lead to injection band broadening due to the stronger adsorption of toluene on C-X. Thus, we conclude that 2.0 mg of C-B is sufficient for trapping the less volatile fraction of anticipated VOC mixtures, and the next-generation μPCF to be used in the PEMM prototype should be designed to hold this mass of C-B.

3.3.4 Sampling and analysis of the 17-VOC mixture

The performance of μPCF-2 was then evaluated with a test atmosphere containing a mixture of the 17 compounds in Table 3.1, each at 10 ppm to facilitate rapid separation and detection of low breakthrough fractions with the downstream capillary column and FID. The sampling flow rate was 5 mL/min and the test was concluded when the total sample volume reached 60 mL. The breakthrough curves in Figure 3.6a demonstrate the partial selectivity against high-p_v compounds: the V_{b10} values of dichloromethane, acetone, and 2-butaone were all smaller than that of benzene, and the former two compounds reached 100% breakthrough prior to V_{b10} for benzene. Although a fraction of the sampled mass of each of these compounds was retained, it was much lower than that of the sentinel benzene and other targets. Surprisingly, the V_{b10} of 1,2-dicholoroethane was also slightly smaller than that of the more volatile benzene, which can be ascribed to the dipolarity of this compound and consequent lower affinity for the non-polar C-X surface. Despite the presence of several compounds competing for adsorption sites on the C-X, the V_{b10} of benzene was still 31 mL.

Figure 3.6b shows the chromatogram obtained by sampling at 5 mL/min for 4 min through the μPCF-2, followed by heating, back flushing, and injecting the sample with a 2:1 split and an analytical path flow rate of 3 mL/min of He. A 20-mL sample volume was used for convenience to illustrate the selective preconcentration and, at the same time, generate reasonably large peaks for all compounds. As shown, all 17 compounds were separated in < 3 min. Acetone and dichloromethane eluted first and gave much smaller peaks due to selective preconcentration. The 2-butanone eluted next and gave a large peak due to its being retained to a greater extent than the other two interferences. The remaining 14 compounds were captured quantitatively from the 20 mL sample (see Figure 6a; total mass of ~12 μg) and the injected masses of each ranged from 630 to 1380 ng prior to the split. Notably, both 1,2-dichloroethane and ethyl acetate eluted before benzene due to their higher polarity, and gave somewhat smaller peaks, presumably due to their having smaller response factors in the FID.[17]

Among the 14 targets the chromatographic resolution was quite good, with values of $R_s >$ 1.0 in all cases. Prior work demonstrated about a 10% reduction in resolution of early eluting peaks for the microcolumns to be used in the PEMM prototype relative to a commercial capillary like that used here, indicating that the separation of similar mixtures should be comparable. The inset in Figure 6b shows that the first six compounds were separated in < 24 sec. Some tailing was evident in all of the peaks, but asymmetry factors were < 1.6 in all cases due, in part, to the sharp split injection. The small *fwhm* values of peaks 13-17 (i.e., 0.8 to 1.3 sec) reflect the influence of on-column focusing at the outset of the separation. The somewhat larger *fwhm* values of peaks 7-12 (i.e., 1.2 to 1.7 sec) reflect the fact that these compounds are too volatile to be focused, and they have wider effective injection bands and spend more time on the column than the more volatile compounds (i.e., peaks 4-6) for which *fwhm* ranged from 0.8 to 1.1 sec). Regardless, none of the peaks is excessively broad and all are well separated. Moreover, there is additional space available in the mid-range of the chromatogram to accommodate other compounds that might be encountered in practice in this volatility range.

3.3.5 Preconcentration factors (PF)

Assuming no breakthrough, the PF is the ratio of the volume of the air sample collected to the volume in which that same mass is contained at the point of detection.[24,25] The latter can be taken as the volume of the peak generated directly from the injection or after chromatographic separation. The latter volume will differ from the former due to on-column focusing or broadening of the injection band, but using it to determine an "effective PF", while less rigorous, is more practical, since all analyses will include a separation step prior to detection. Note that the practice of calculating "preconcentration factors" from the ratio of peak areas generated with and without a μPCF included in the system[26,27] is not recommended, because it does not afford any useful information about the critical performance parameters of a μPCF.

For the most volatile target, benzene, an injection *fwhm* value of 0.90 sec was obtained at 3 mL/min (no split), which corresponds to a preconcentrated volume of 0.048 mL. Assuming a 31-mL sample volume, then we obtain a PF value of ~620 for benzene. For our least volatile target, n-dodecane, the injection *fwhm* value was ~1.7 sec at 3 mL/min (no split), which corresponds to a peak volume of 0.085 mL. For a sample volume of 31 mL, this yields a PF value of only 370. Note, however, that V_{b10} for n-dodecane was > 150 mL under all conditions tested. Increasing the assumed sample volume to 150 mL leads to a PF of 1590, even after allowing for a 10% increase in the *fwhm* value of the peak at the higher injection mass.

If an injection split were used, then there would be a commensurate reduction in PF due to the loss of sample mass, which would greatly exceed the decrease in *fwhm* afforded by the split (see Figure 3.4b). For example, from Figure 3.6b, the *fwhm* values of benzene and n-dodecane after separation on a 6-m column at 3 mL/min with a 2:1 injection split were 1.5 and 1.9 sec, respectively. The effective PF values using the corresponding peak volumes of 0.076 mL and 0.097 mL together with the 20 mL sample volume, were only 88 and 68 for benzene and n-dodecane, respectively, reflecting the small sample volume and the loss of ~67% of the sample from the split injection.

3.4 Conclusions

The design and operating features of the μPCF developed here meet or exceed the requirements of this component of the (wearable) μGC into which it will be integrated for the specific application of quantitatively analyzing exposures to mixtures of VOCs encountered in workplace environments. Thus, a dual-cavity μPCF containing 2.0 and 2.3 mg of C-B and C-X, respectively, operated at a flow rate of 5-10 mL/min yielded V_{b10} values ranging from ~10 mL to > 40 mL for mixtures of ~10-20 compounds in the designated volatility range, with preconcentration factors of ~200 to 1,600 and sampling times of ≤ 5 min.

Selectivity against high-volatility interferences was achieved/demonstrated while retaining the capability for exhaustive capture of target compounds, in mixtures, at relevant concentrations. The breakthrough volumes and associated quantities of target compounds captured (and subsequently thermally desorbed) were sufficiently large to ensure detection at < 0.1 TLV by the microsensor array to be used as the μGC detectors. Conditions established for desorption and injection into a downstream separation column ensured > 99% desorption efficiency and injection bandwidths narrow enough to permit high chromatographic resolution of mixture components. The latter could be enhanced by use of split injection in cases where the accompanying loss in sensitivity could be tolerated.

3.5 References

[1] T. Sukaew, H. Chang, G. Serrano, E. T. Zellers, Multi-stage preconcentrator/focuser module designed to enable trace level determinations of trichloroethylene in indoor air with a microfabricated gas chromatograph *Analyst*, 136, 1664-1674, 2011.

[2] ACGIH, Threshold Limit Values for Chemical Substances and Physical Agents & Biological Exposure Indices for 2015, ACGIH, Cincinnati, OH, 2015.

[3] J. S. Ignatio, W. H. Bullock, Eds., *A Strategy for Assessing and Managing Occupational Exposures*, 3rd Ed., AIHA Press, Fairfield, VA, 2006.

[4] J. L. Perkins, *Modern Industrial Hygiene - Vol. 1. Recognition and Evaluation of Chemical Agents*, 2nd Ed., ACGIH, Cincinnati, OH, 2008.

[5] National Institute for Occupational Safety and Health, *NIOSH Manual of Analytical Methods*, http://www.cdc.gov/niosh/docs/2003-154/ (accessed May 2015).

[6] Occupational Safety and Health Administration, *Sampling and Analytical Methods*, https://www.osha.gov/dts/sltc/methods/ (accessed May 2015).

[7] C-J Lu, E. T. Zellers, A dual-adsorbent preconcentrator for a portable indoor-VOC microsensor system *Anal. Chem.*, 73, 3449-3457, 2001.

[8] C-J. Lu, E. T. Zellers, Multi-adsorbent preconcentration/focusing module for portable-GC/microsensor-array analysis of complex vapor mixtures, *Analyst*, 127, 1061-1068, 2002.

[9] W-C Tian, S. Pang, C-J Lu, E. T. Zellers, Microfabricated preconcentrator-focuser for a microscale gas chromatograph, *J. Microelectromech. Syst.*, 12, 264-272, 2003.

[10] W.C. Tian, H. K. L. Chan, C-J. Lu, S. W. Pang, E. T. Zellers, Microfabricated multi-stage preconcentrator-focuser for a micro gas chromatograph, *J. Microelectromech. Syst.*, 14, 498-507, 2005.

[11] G. Serrano, T. Sukaew, E. T. Zellers, Hybrid preconcentration/focuser module for determinations of explosive marker compounds with a micro-scale gas chromatograph *J. Chrom. A*, 1279, 76-85, 2013.

[12] T. Sukaew, E. T. Zellers, Evaluating the dynamic retention capacities of microfabricated vapor preconcentrators as a function of flow rate *Sens. Actuators B: Chemical*, 183, 163-171, 2013.

[13] J. H. Seo, S. K. Kim, E. T. Zellers, K. Kurabayashi, Microfabricated passive vapor preconcentrator/injector designed for micro gas chromatography *Lab Chip*, 12 (4),717-724, 2012.

[14] S. K. Kim, D. R. Burris, H. Chang, J. Bryant-Genevier, and E. T. Zellers, Microfabricated gas chromatograph for on-site determinations of trichloroethylene in indoor air arising from vapor intrusion, part 1: field evaluation, *Env. Sci. and Tech*., 46, 6065-6072, 2012.

[15] W. R. Collin, G. Serrano, L. K. Wright, H. Chang, N. Nuñovero, E. T. Zellers, Microfabricated gas chromatograph for rapid, trace-level determinations of gas phase explosive marker compounds, *Anal. Chem.*, 86, 655-663, 2014.

[16] J. Whiting, R. Sacks, Evaluation of split/splitless operation and rapid heating of a multi-bed sorption trap used for gas chromatography analysis of large-volume air samples *J. Sep. Sci.*, 29, 218-227, 2006.

[17] R. L. Grob, E. F. Barry, *Modern practice of gas chromatography*, 4th edition, Wiley Interscience, Hoboken, NJ, 2004, pp. 114-115.

[18] C. Zhou, Y. Jin, H. Xu, S. Feng, G. Zhou, J. Liang, J. Xu, Use of wheeler-jonas equation to explain xenon dynamic adsorption breakthrough curve on granular activated carbon *J. Radioanal. Nucl. Chem.*, 288, 251-256, 2011.

[19] C-J. Lu, W.H. Steinecker, W-C. Tian, M.C. Oborny, J.M. Nichols, M. Agah, J.A. Potkay, H.K.L. Chan, J. Driscoll, R.D. Sacks, K.D. Wise, S. W. Pang, E.T. Zellers, First-generation hybrid MEMS gas chromatograph, *Lab Chip*, 5, 1123-1131, 2005.

[20] Q. Zhong, W. H. Steinecker, E. T. Zellers, Characterization of a high-performance portable GC with a chemiresistor array detector, *Analyst*, 134, 283-293, 2009.

[21] Lahlou, H.; X. Vilanova, X. Correig, Gas phase micro-preconcentrators for benzene monitoring: a review *Sens. Actuators, B: Chemical*, 176, 198-210, 2014.

[22] G. Wood, E. S. Moyer, A review of the wheeler equation and comparison of its applications to organic vapor respirator cartridge breakthrough data *Am. Ind. Hyg. Assoc. J.* 50 (8), 400-407, 1989.

[23] C. Zhou, Y. Jin, H. Xu, S. Feng, G. Zhou, J. Liang, J. Xu, Use of wheeler-jonas equation to explain xenon dynamic adsorption breakthrough curve on granular activated carbon *J. Radioanal. Nucl. Chem.*, 288, 251-256, 2011.

[24] International Union of Pure and Applied Chemistry, Compendium of chemical terminology gold book, 2.3.3, 1174-1175, 2004, available at goldbook.iupac.org/P04804 (accessed May 2015).

[25] J. Namieśnik, Preconcentration of gaseous organic pollutants in the atmosphere *Talanta*, 35(7) 567-587, 1988.

[26] B. Alfeeli, M. Agah, MEMS-based selective preconcentration of trace level breath analytes *IEEE Sensors J.*, 9, 1068-1075, 2009.

[27] W-C. Tian, T. H. Wu, C-J Lu, W. R. Chen, H. J. Sheen, A novel micropreconcentrator employing a laminar flow patterned heater for micro gas chromatography *J. Microelectromech. Syst.*, 22 (6), 1-8, 2012.

Table 3.1 17 test compounds with corresponding vapor pressures (p_v) and TLVs.

Compound	Peak #[a]	p_v [b] (kPa)	TLV[c] (ppm)
dichloromethane	2	58.0	50
(DCM)[d]	1	31.5	500
acetone (ACE)[d]	3	13.3	200
2-butanone (MEK)[d]	6	12.6	0.5
benzene (BEN)	5	10.5	10
1,2-dichloroethane	4	9.71	400
(DCA)	7	6.25	10
ethyl acetate (EAC)	9	3.78	20
trichloroethylene	8	2.65	20
(TCE)	11	1.53	150
toluene	10	1.46	5
methyl isobutyl ketone	12	1.27	20
n-butyl acetate	13	1.01	100
2-hexanone	14	0.60	50
ethylbenzene	15	0.27	25
m-xylene	16	0.033	1
cumene 1,2,4-trimethylbenzene nitrobenzene n-dodecane	17	0.018	-[e]

[a] Peak assignments for chromatogram in Fig. 3.6b.

[b] Values at 25 °C.

[c] TLV-TWA; ref. 2.

[d] High-volatility interferences.

[e] No assigned TLV value.

Table 3.2. Desorption efficiencies (DE) of three test compounds from µPCF-2 for different heating periods; T_{max} = 225 °C.

	Avg. DE (%)[a]		
Compound	20 sec	40 sec	60 sec
benzene	>99	>99	>99
toluene	99	>99	>99
dodecane	97	99	>99

[a] Compounds were tested individually; ~250 ng of vapor was loaded for each test; desorption flow rate = 3 mL/min; n = 3 for each case (RSD < 8% in all cases); resolution of the determination was 0.5-1%

Table 3.3 Values of V_{b10} for benzene and toluene tested individually at 5 ppm and 30 °C with the two single-cavity μPCF devices indicated.

Device	Compound	V_{b10}[a] (mL)	RSD (%)
μPCF-1x	benzene	41.0	1
μPCF-1b	toluene	31.0	4

[a] Avg. of 3 replicates each at 5 and 10 mL/min.

Table 3.4 Values of V_{b10} for mixtures of representative VOCs drawn through µPCF-2 and µPCF-1x, as a function of concentration, temperature, and sampling flow rate.

Compound	Flow rate (mL/min)	V_{b10} (mL) µPCF-2						µPCF-1x
		30 °C			100 ppm			200 ppm
		200 ppm	150 ppm	100 ppm	25 °C	35 °C	40 °C	30 °C
2-butanone	4	4.5	5.0	5.0	5.0	3.0	2.0	7.0[a]
	6	4.5	4.5	5.0	-[b]	-	-	-
	8	4.0	4.5	4.5	-	-	-	-
	10	4.0	4.0	4.5	-	-	-	6.5
benzene	4	8.5	8.5	9.0	9.5	4.5	3.0	11.0
	6	8.0	8.0	8.5	-	-	-	-
	8	7.5	8.0	8.5	-	-	-	-
	10	7.5	8.0	8.5	-	-	-	11.0
ethyl acetate	4	11.0	11.5	12.0	12.5	7.0	4.5	13.5
	6	11.0	11.5	11.5	-	-	-	-
	8	10.5	11.0	11.5	-	-	-	-
	10	10.0	11.0	11.0	-	-	-	14.0
toluene	4	27.0	32.0	37.0	46.0	27.0	17.0	45.0
	6	25.0	30.0	35.0	-	-	-	-
	8	25.0	30.0	34.0	-	-	-	-
	10	24.0	29.0	32.0	-	-	-	45.0

[a] tested at 5 mL/min instead of 4 mL/min; [b] denotes untested conditions

Table 3.5 Values of V_{b10} for a mixture of representative VOCs (200 ppm each) with μPCF-1b as a function of temperature.

Compound	V_{b10} (mL)[a]		
	30 °C	35 °C	40 °C
toluene	12.0	11.5	9.5
cumene	23.0	22.0	20.0
1,2,4-trimethylbenzene	82.5	80.5	78.0
n-dodecane	>150	>150	>150

[a] Avg. of 3 replicates each at 5 and 10 mL/min (RSD < 3 % in all cases).

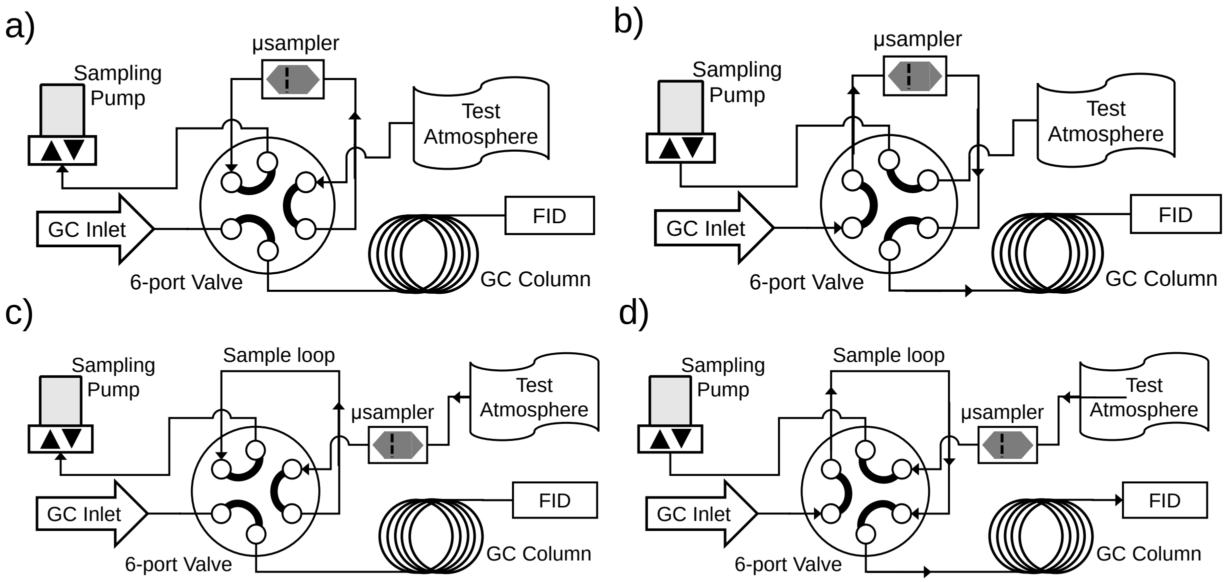

Figure 3.1. Experimental set-ups for desorption and capacity testing of each μPCF. For the former, the μPCF was a) pre-loaded from the test atmosphere and then b) heated and back-flushed for desorption. For the latter, c) the test atmosphere was continually drawn through the μPCF and the sample loop and d) periodically (e.g., every 30 sec) the sample loop volume was injected into the column for separation and quantification.

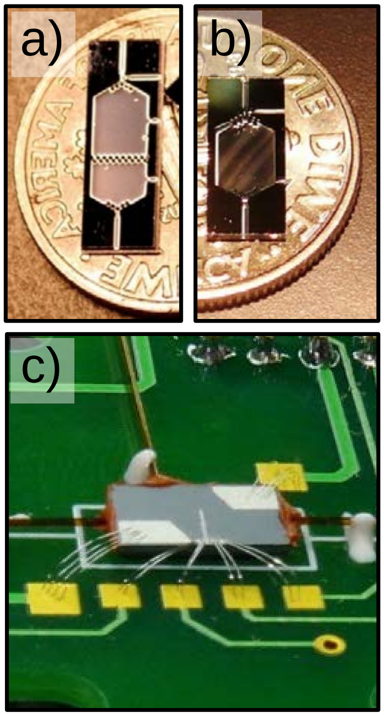

Figure 3.2. Photographs of a) µPCF-2; and b) µPCF-1 devices (on U.S. dimes for scale); c) µPCF-2 inverted and mounted to a custom printed circuit board; device is suspended by the inlet/outlet capillaries that are epoxied to the board for mechanical and thermal isolation. Wire bonded leads are for (bulk) heating and for monitoring temperature via the patterned RTD extending into the center of the chip.

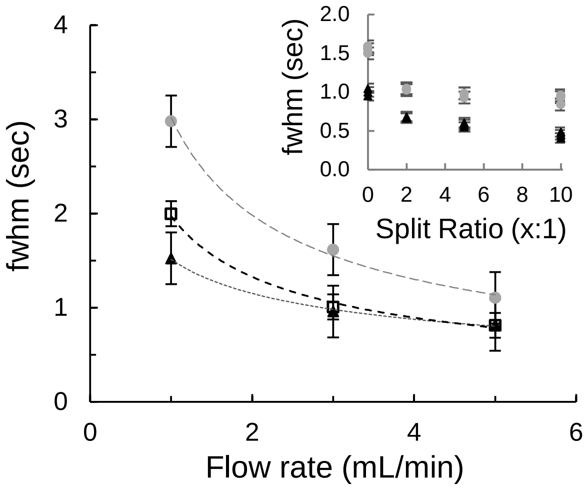

Figure 3.3. Desorption bandwidth (i.e., *fwhm*) from μPCF-2 as a function of flow rate for benzene (triangles), toluene (squares), and n-dodecane (circles), tested individually without a downstream column; FID. Error bars represent 95% confidence intervals (n=3). Curves represent the least-squares fits to the data. Inset shows the effect of the injection split-flow ratio (vent:analysis) on the *fwhm* values for benzene and n-dodecane; analytical path flow rate was maintained at 3.0 mL/min.

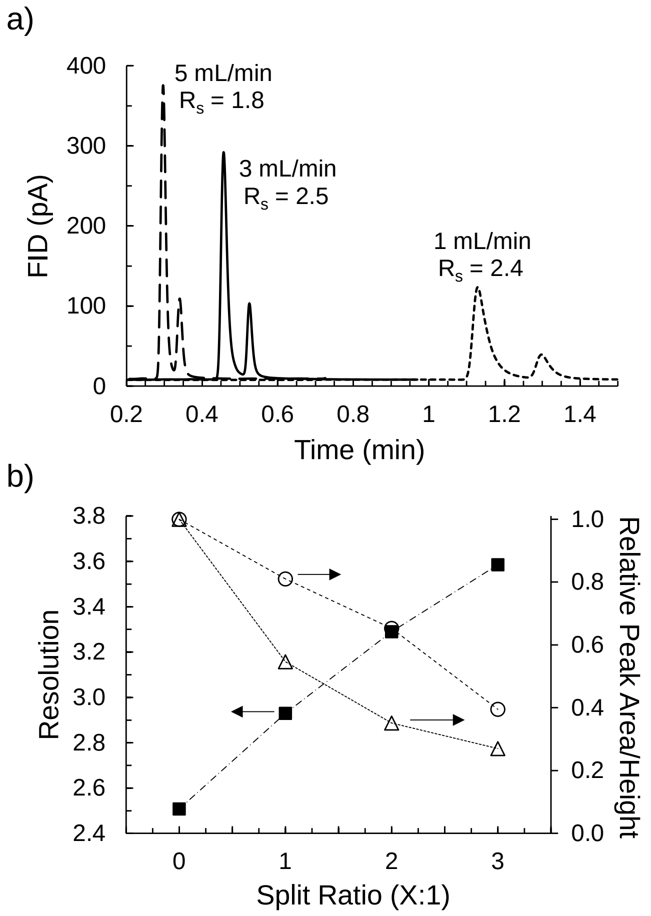

Figure 3.4. a) Superimposed chromatograms of benzene (1st peak) and trichloroethylene (2nd peak) collected at three flow rates (as indicated), with the corresponding R_s values for the pair. Samples of the binary vapor mixture (~50 ng each) were pre-loaded into µPCF-2, desorbed/injected splitless in He, and separated on a 6-m long, PDMS-coated capillary column isothermally at 30 °C; FID. b) R_s (squares), average peak height (circles), and average peak area (triangles) for benzene and trichloroethylene plotted as a function of the injection split-flow ratio (vent:analysis), with the column (analytical path) flow rate maintained at 3.0 mL/min.

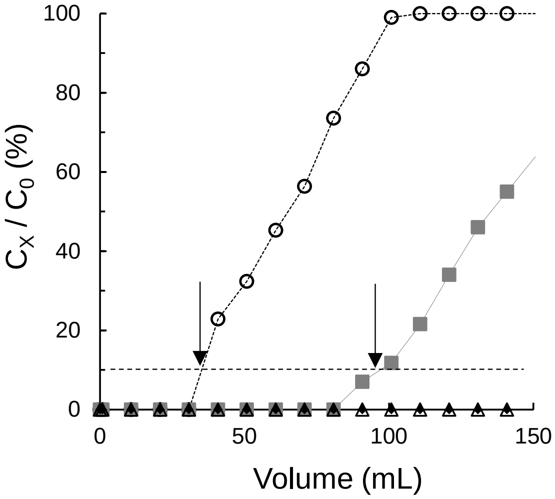

Figure 3.5. Representative breakthrough curves of μPCF-2 challenged with a mixture of benzene, toluene, ethylbenzene and m-xylene (i.e., BTEX) at 1, 20, 20, and 100 ppm, respectively (i.e., TLV concentrations for all except benzene) in N_2. C_x/C_o is the breakthrough fraction. V_{b10} values for benzene (33 mL) and toluene (90 mL) are designated by the vertical arrows. V_{b10} values for ethylbenzene and m-xylene were > 150 mL. Conditions: flow rate = 5 mL/min; temperature = 30 ^{0}C; FID.

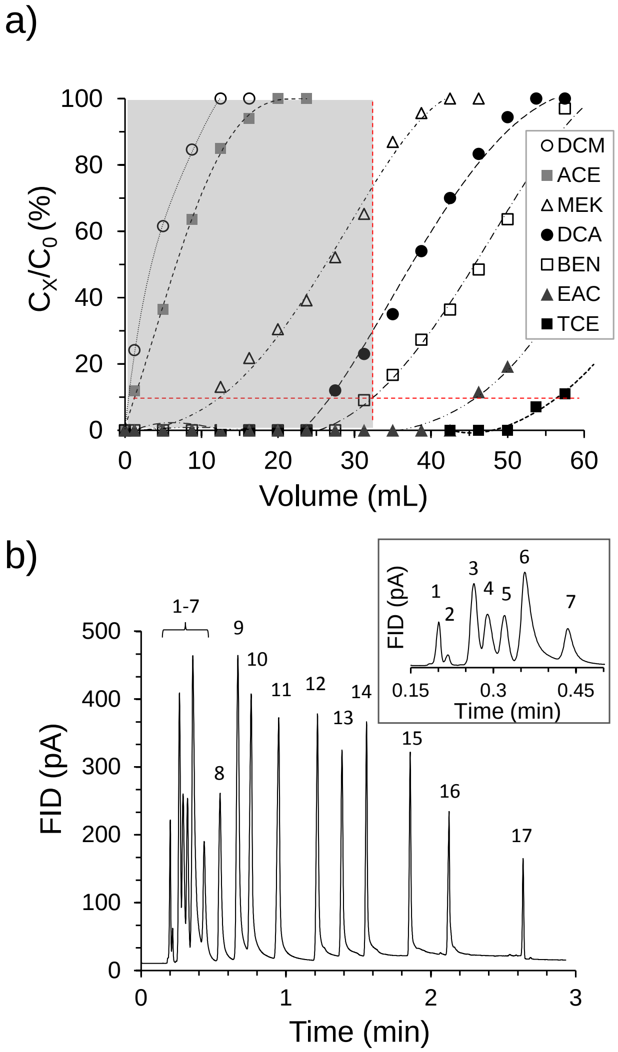

Figure 3.6. a) Breakthrough curves of µPCF-2 challenged with the 17-VOC mixture (see Table 1 for acronym definitions) at 30 °C and 5 mL/min with C_o = 10 ppm for each compound; only the first seven compounds to break through were monitored. Shaded region corresponds to $V \leq V_{b10}$ for benzene. b) Chromatogram of a 20-mL sample of the same 17-VOC test atmosphere injected from µPCF-2 and separated on a 6-m capillary column; inset shows enlargement of the first seven compounds to elute (see Table 1 for peak # assignments). Conditions: 3 mL/min; 2:1 split injection; column held at 28 °C for 0.5 min, then 10 °C/min to 33 °C, then 50 °C/min to 125 °C.

Chapter 4

Micro-Scale Gas Chromatograph Prototype for Analysis of VOC Mixtures at Typical Workplace Concentrations

4.1 Introduction

Gas chromatographic instrumentation constructed using Si-microfabricated components (μGC) may afford the occupational exposure scientist a tool for collecting near-real-time *personal* exposure measurements of multiple volatile organic compounds (VOC). Such technology would fill the long-standing gap in VOC monitoring capabilities between standard time-integrating sorbent-tube samplers used with personal sampling pumps, which rely on off-site laboratory analysis,[1-2] and extant portable GCs[3] and more sophisticated field-transportable FTIR[4] and GC-MS[5] instruments, which are too large and expensive for routine evaluations of personal exposures. The capability to accurately determine the identities and concentrations of multiple VOCs directly on individual workers over short time periods would facilitate determinations of compliance with established regulations and would also enhance the quality and quantity of exposure data obtainable for studies of health effects of VOCs commonly encountered in working environments.[6]

For such applications, a μGC would need to have (microfabricated) components capable of the following functions: (selective) sample capture/preconcentration and focused injection, chromatographic separation, and detection. Pumps and valves would also be required. Since the first μGC was described in the late 1970s,[7] and some of the components of that microsystem were incorporated into commercial instruments,[8] significant advances have been made by numerous other research groups in the design and demonstration of individual microfabricated components for preconcentration,[9-13] separation,[14-25] and detection,[26-32], and in their integration into functional microanalytical subsystems.[33-36] Many fewer reports have appeared on packaged μGC prototypes wherein all key components are microfabricated,[37-39] and the goal of creating hand-held or wearable battery operated μGC instrumentation for routine air monitoring has yet to be realized.

Over the past 15 years, our group has also developed and characterized microfabricated components for μGC, including preconcentrators,[40-44] one- and two-dimensional separation modules,[45-48] and sensors and sensor arrays.[49-55] We have assembled some of these into μGC[56,57] and μGC × μGC[58,59] subsystems, and we have also developed fully automated prototype instruments containing μGC systems for measuring low- to sub-ppb concentrations of trichloroethylene (TCE) in vapor-intrusion (VI) impacted homes,[60-62] and vapor phase markers of the explosive trinitrotoluene for ultimate deployment at transportation security checkpoints.[63] Features common to these prototype instruments include a partially selective high-volume sampler of conventional design, a micromachined preconcentrator/focuser (μPCF) for focusing and injection, μcolumn(s) for temperature programmed separations, and an integrated array of four microfabricated chemiresistors (μCR) with thiolate-monolayer protected gold nanoparticle (MPN) interface films for multichannel detection. The inclusion of an array-based detector adds an additional dimension to the analysis, which facilitates the recognition of eluting VOCs.[53]

Our current efforts are directed toward creating a μGC that we have termed a Personal Exposure Monitoring Microsystem (PEMM), which is being designed as an autonomous, battery operated, belt-mountable instrument for measuring worker exposures to numerous target VOC mixtures simultaneously. Toward that end we created a first-generation (Gen-1) bench-top PEMM prototype that is AC powered and laptop controlled. The Gen-1 PEMM (i.e., PEMM-1) is the subject of this report, and the purpose of this study was to gather experience and data to inform the design, assembly, and operating conditions of the wearable Gen-2 PEMM (i.e., PEMM-2).

By way of introduction, a block diagram of the analytical subsystem of the Gen-1 PEMM is presented in Figure 4.1. The core microanalytical system comprises a dual-bed μPCF, a dual-μcolumn separation stage, and a μCR array. This is combined with non-microfabricated components that include a pre-trap, a set of manifold-mounted latching mini-valves for directing flow, a split-injection valve, a mini-pump, a regulated in-board He gas canister, interface circuitry for powering, controlling and/or processing signals from each component, and software for operating the system and acquiring data with a dedicated laptop computer.

By design, air samples would be drawn by the mini-pump through the inlet, and low volatility interfering VOCs would be completely or partially retained by the wall-coated-capillary Pretrap (not presented here). The rest of the air sample would then pass through the μPCF, where target VOCs would be quantitatively captured on one or both of the two adsorbent beds. After turning off the pump and throwing the necessary valves to start the flow of He through the microsystem, the μPCF would be rapidly heated to thermally desorb the sampled VOCs for passage to the μcolumns. A temperature-programmed separation of the VOC mixture components would then be performed, with detection provided by measuring the changes in resistance of the MPN-coated μCR devices in the array. The collective array responses would afford a pattern that could then be merged with retention time (t_R) values to assist in analyte recognition.

The μPCF and μCR array devices of the PEMM-1 unit are the same as those being incorporated into the PEMM-2 units currently under construction, and neither has been presented before. The separation module differs from that to be used in the PEMM-2, and a similar dual-μcolumn ensemble has been used in our recent study of μGC × μGC separations,[47] but they have not been incorporated into a functional microsystem prior to this. Given that they have the same total length as the columns to be used in PEMM-2, they were expected to provide resolution and peak capacities comparable to that planned for the Gen-2 microsystem, though at higher power for heating. Other unique aspects of this system are the use of a pre-trap, split-flow injection, and He carrier gas. Our focus on analytes at relatively high concentrations also separates this study from previous studies. Following descriptions of the devices, system integration methods, and testing methodology, we present a rationale to justify key features and operating parameters incorporated into the PEMM-1 for workplace exposure monitoring applications. We then present component-level test results intended to confirm critical performance capabilities, followed by system-level test results. The implications of the results for the design and operation of the PEMM-2 are then assessed.

The instrument is intended to provide generalized VOC measurements in industrial workplaces. More specifically, we set goals of quantitatively analyzing up to ~20 VOCs per measurement at a rate of ~6-8 measurements per hour. For practical reasons we focused on VOCs falling within a moderate volatility window defined by their vapor pressures. Although concentrations might span a wide range, for quantification it was assumed that they would fall in the mid-parts-per-billion (ppb) to mid-parts-per-million (ppm) range. Reconciling the tradeoffs among preconcentration, separation, and recognition/detection was one of the many challenges faced in striving for satisfactory system-level performance.

4.2 Experimental Methods

4.2.1 Materials

Most test compounds and reagents were purchased from Sigma-Aldrich/Fluka (Milwaulkee, WI) or Acros/Fisher (Pittsburgh, PA) in >95% (most >99%) purity and were used as received. MPNs with core diameters in the range of 3.5–5 nm derived from the following thiols were used as μCR interface films: n-octanethiol (C8), 6-phenoxyhexane-1-thiol (OPH), isooctyl-3-mercaptopropionate (EOE), methyl-6-mercaptohexanoate (HME) and 1-mercapto-(triethylene glycol) methyl ether (TEG). TEG was purchased from Nanoprobes, Inc. (Yaphank, NY). The remaining MPNs were synthesized in house by a known method.[63] EOE was used on the basis of a recommendation from Prof. Lu, at National Taiwan Normal University.[64] The graphitized carbon adsorbents Carbopack X (C-X, 60/80 mesh, 240 m^2/g) and Carbopack B (C-B, 60/80 mesh, 100 m^2/g) were obtained from Supelco (Bellefonte, PA). The C-X and C-B were sieved such that only the fractions with nominal diameters between 212 and 250 μm were used. Polydimethylsiloxane (PDMS) was purchased from Ohio Valley Specialty Chemicals (OV-1, Marietta, OH). Pressurized helium gas canisters (95 mL, 4.0 cm × 4.0 cm × 13 cm) containing 2.4 g of He under a pressure of 2500 psi were obtained from Leland (South Plainfield, NJ). Deactivated fused silica capillary used for interconnections and commercial capillary columns used for some analyses and for the pre-trap were obtained from Supelco.

4.2.2 μPCF

The dual cavity μPCF chip, shown in Figure 2a, had dimensions of 13.6 × 4.1 mm, and was fabricated from Si using deep-reactive-ion-etching (DRIE). Each cavity has a volume of ~4.7 μL, with the two 380 μm deep cavities separated by a row of 150 μm diameter pillars spaced 150 μm from one another. The walls of the cavities are tapered toward the inlet/outlet channels to reduce turbulence. Filling ports were etched into the sidewalls of each cavity for loading the adsorbents. Fluidic ports were etched to snugly accommodate a 250 μm i.d. (380 μm o.d.) fused silica capillary. The inlet channel of the device features a tee junction to permit sample loading through one branch and back-flushed injection through the other. A 120-μm thick Pyrex plate was anodically bonded to the top surface at wafer level to seal the cavities and channels. A Ti/Pt resistive heater and resistive temperature device (RTD) were patterned onto the backside of the Si after growing a thin oxide layer for electrical isolation (Figure 4.2a). Modeling was performed by members of the Kurabayashi research group to assess and optimize the temperature gradients and power efficiency for different heater-metal configurations, and the final design represented a trade-off in optimizing these performance parameters. The details of this modeling are not presented here. Devices were then diced into individual chips, and deactivated fused silica capillaries (0.250 mm i.d.) were affixed to the three fluidic ports using a flexible, high-temperature silicone adhesive (Duraseal 1531, Cotronics, Brooklyn, N.Y.).

The front cavity (i.e., that ultimately mounted closest to the μcolumns; Figure 4.1) was loaded with 2.0 mg C-B and the rear cavity was loaded with 2.3 mg C-X. Each cavity had an internal volume of 4.7 μL, making the rear cavity larger than that of the dual stage device evaluated in Chapter 3. Mild suction applied to the fluidic port for each cavity was used to entrain adsorbent granules and draw them into the device one by one. Physical agitation was used to ensure tight packing of the adsorbent and complete filling of each cavity. Adsorbent masses were determined by weighing the device to ±0.1mg with an electronic balance before and after loading (note: since C-B has a lower bed density than C-X, i.e., 0.38 and 0.43 g/cm^3, respectively, according to Supelco, the mass of this adsorbent contained in a given cavity volume is also lower). Filling ports were subsequently sealed with Duraseal under gentle suction to ensure that the adhesive contacted the inner walls of the filling port.

The device was inverted and then mounted on a custom printed circuit board (PCB) using epoxy (Hysol 1C, Rocky Hill, C.T.); only the capillaries were bonded to the board to maximize thermal isolation of the device. A rectangular hole in the PCB beneath each device further improved thermal isolation. Al wire-bond wires were used for electrical connections to the heater and RTD.

An initial fast (uncontrolled) ramp of 400 °C/sec, on average, was used to heat from 30°C to 100°C, followed by a slower controlled ramp of 150 °C/sec (achieved via the PWM algorithm described above). The rapid initial rate of heating insured sharp desorption of the more volatile fraction of analytes, and the lower heating rate used subsequently minimized over-shooting the maximum temperature of 225 °C. Figure 4.4 shows the heating and cooling profiles of the μPCF. Cooling back to the baseline temperature of 30 °C required roughly 90 s and was thus complete prior to the time period anticipated for elution of the analytes in a typical run. The initial heating rate was very reproducible, with a 14% (rsd) over the course a series of 10 injections.

Injection bandwidth was characterized using a bench-scale GC with flame ionization detector (FID) (7890 Agilent, Santa Clara, CA) with the μPCF mounted across two ports of a 6-port valve. Test atmospheres containing ~ 5 ppm of benzene, toluene or dodecane in N_2 were generated in Flex-foil® inert gas sample bags (Supelco). A suction pump (model UMP015, KNF

Neuberger, Trenton, N.J.) was used to draw a sample from the bag through the μPCF to load 50-100 ng of analyte, after which the valve was switched and He from the GC injection port was backflushed through the μPCF while it was heated to 225 °C and maintained at that temperature for 60 s, which are the conditions to be used for injection in the prototype.

4.2.3 μColumns

Each of the two μcolumn chips (Figure 4.2b; 3.1 × 3.1 cm) contains a single DRIE channel (240 μm (d) × 150 μm (w); 3.1 m long) that spirals in to the center and then back out to the edge of chip in a square pattern with chamfered corners. A 500 μm Pyrex cap was anodically bonded to the top face sealing the fluidic channel at wafer scale. A pair of heaters and an RTD were patterned with Ti/Pt onto the backside for heating and monitoring temperature, respectively. Deactivated fused silica capillaries (250 μm i.d.) were inserted into the fluidic ports at the inlet and outlet of each μcolumn and sealed with Duraseal.

A previously described static method was used for depositing the PDMS stationary phase on the inner walls of the channels.[18,45]. It entailed filling with a solution of PDMS in dichoromethane that also contained 1% (w/w-PDMS) dicumyl peroxide as the cross-linking agent, sealing one end of the μcolumn temporarily, and then slowly evaporating the solvent using a light vacuum at constant temperature. The PDMS was then cross-linked by gradually heating to 180 °C over the course of 40 min under N_2. The concentration of the PDMS solution was adjusted to yield a nominal average thickness of 0.20 μm.

After coating, the inlet and outlet capillaries were removed from the fluidic ports and replaced with fresh uncoated capillaries that were sealed to the chip with Hysol. The capillaries emanating from the outlet of the first μcolumn and the inlet of the second μcolumn were cut to a length of ~ 5 mm, inserted into opposite ends of a short (i.e., ~1.2 cm) Pyrex/Si conduit interconnect with a Ti/Pt meander-line heater patterned on the Pyrex, and sealed with Hysol. The assembly was then inverted and affixed, with Hysol, to a custom PCB with rectangular cutouts below the μcolumn. Electrical connections were made with Al wire-bonds.

Prior to system integration, this dual ensemble of μcolumns was characterized for separation efficiency and dynamic range. The μcolumns were installed inside the oven of the bench scale GC, and connected between the GC inlet and FID. Analytes were introduced by either autosample syringe or a conventional 6-port valve (model# AC6WE, Vici Valvo, Houston TX) mounted to the GC. The FID was calibrated using syringe liquid injections of analyte diluted in CS_2.

4.2.4 μCR array

In an effort to improve the sensitivity and chromatographic performance of the Gen-1 sensor devices presented in Chapter 2, several design changes were incorporated into the Gen-2 μCR arrays. The μCR array chip (33 × 20 × 0.5 mm) has a linear arrangement of sensors, comprised of 10 sets of Cr (30 nm)/Au (300 nm) interdigital electrodes (IDE) in a single row, with a Cr/Au RTD at the center, deposited and patterned via a standard lift-off process onto a Pyrex substrate. Each μCR contained 27 pairs of IDEs, 5 μm wide spaced 4 μm apart and overlapping by 210 μm. A meander-line Ti (30 nm)/Pt (80 nm) heater was patterned on the backside. Header pins were bent 90^0 and low-temperature-soldered to each of the 22 bonding pads on the top surface. Cables were soldered to the heater bonding pads. The linear arrangement of the sensors, along with the glass substrate, allowed for a mirco-fabricated narrow flow-path fluidic channel to be loaded on-top, reducing the fluidic dead-volume inside the sensor chamber by eliminating the conventionally machined ceramic lid and double-sided adhesive tape. The Si lid (33 × 10 × 0.5 mm) was fitted with a linear recessed channel, 150 µm deep × 350 µm wide, etched by DRIE lengthwise down the center so as to align directly above the sensors in the array. The near-zero dead volume fluidic channel of the lid, with a cross-sectional area roughly equivalent to the µcolumn and interconnecting fused silica capillary, was intended to eliminate any flow-dependent contributions to extra-column band broadening in the sensor, thus improving chromatographic performance (narrower channel allows for faster diffusion in the mobile phase above the sensor, improving the rate of response by reducing the time necessary to reach equilibrium in absorption and desorption).

The array was cleaned by sequential sonication in acetone and 2-propanol, followed by drying in a stream of scrubbed air. MPNs were dissolved in suitable solvents (toluene for C8, OPH, and TEG, chloroform for EOE, dichloromethane for HME) at concentrations of ~5 mg/mL. Two sensors were coated with films of each type of MPN by drop-casting from a 1 µL syringe to create multilayer films with baseline resistances between 100 kΩ and 10 MΩ, depending on the MPN and the film thickness. Film thicknesses were not measured but are estimated to be on the order 200-500 nm, on average, on the basis of previous work.[50] Films were not uniform, but rather exhibited a classic "coffee stain" pattern upon solvent evaporation.

After coating, strips of 50-µm thick double-sided adhesive (VHB tape, 3M, St Paul, MN), measuring 3 × 25 mm, were mounted along both sides of the line of sensor on the array. The Si lid was aligned above the array substrate and then lowered onto the tape and pressed down to create a seal. A narrow bead of Hysol epoxy was then applied along the outer seam to further seal the interface and left at room temperature for 24 hr to cure under N_2. Segments of 250 µm i.d. deactivated fused silica capillary were affixed to the fluidic ports with Hysol for making connections to other devices.

The Gen-2 µCR arrays (lidded and plumbed) were calibrated using a conventional benchtop GC equipped with an autosampler and 6-port valve. The sensor array was placed inside the GC oven, maintained at 30^0C, and plumbed between a 6-m commercial PDMS column upstream and a calibrated FID for reference downstream. Static test atmospheres containing n-hexane, methyl ethyl ketone, ethanol and toluene were generated, verified by FID, then used to calibrate the µCR using a conventional 6-port valve. Peak areas were determined using OriginPro software, and calibration curves were built in Excel.

4.2.5 System control and data acquisition

Two custom PCBs were designed, fabricated (Advanced Circuits, Aurora, CO), populated, and verified to provide the electronic interfaces for the µCR array, temperature sensors, mini-pump, mini-valves and device heaters and RTDs. Control of the thermal, fluidic and analytical components was possible through the software graphical-user-interface (GUI), which permitted either manual real time or autonomous unattended operation of the instrument. Independent proportional-integral-derivative (PID) feedback loops were designed to achieve control and optimal reproducibility of the device temperature programs at the specified heating rates and set-point temperatures. Solid-state relays, mounted on the PCBs, were used to control the device heaters by pulse-width-modulation (PWM) generated signals.

Among the main considerations in the PCB layouts was the appropriate use of low-noise design techniques in order to maintain the integrity of the noise-sensitive signals, most importantly, the µCRs. At the front-end of the µCR interface electronics, a nulling circuit was implemented to cancel the baseline resistance contribution to the sensor output signals. An algorithm was developed to generate the digitally controlled cancelling signals used for baseline cancellation during the initial start-up of the instrument. This implementation also compensated for medium- and long-term drift in sensor resistances, and maximized the signal-to-noise ratio prior to digitization. In addition, an automated selection feature of appropriate excitation voltages for the µCRs was created, achieving similar circuit sensitivities regardless of sensor resistances, and improving the reproducibility of the response measurements. By monitoring the cancelling signals applied to the aforementioned nulling circuit, it was possible to convert the measured output voltages to changes in relative resistance and to display the responses in such units in real time.

The instrument was operated via a laptop computer and a custom LabVIEW (Ver. 14.0, National Instruments, Austin, TX) program written in-house. A single 16-bit multi-functional DAQ card (USB-6216 OEM, National Instruments, Austin, TX), mounted between the two custom PCBs, was used for data acquisition and signal generation tasks. The µCR array signals, device temperatures, and instrument configuration parameters were monitored and stored for subsequent data analysis. Raw chromatogram traces were stored as text files and subsequently analyzed using OriginPro (Ver. 9.1, OriginLab, Northampton MA) to extract retention times, peak heights, and peak areas). Calibration curve development and resulting response pattern comparison were performed in Excel.

4.2.6 System Integration and Prototype Assembly.

Figures 4.2d and 4.2e show the arrangement of PCBs and fluidic components prior to final assembly, and the fully assembled PEMM-1 prototype, respectively. The dimensions of the latter are 6 (h) x 12 (w) x 5.5 (d) inches without the He canister and it weighs 7 lbs (without the He canister). Adding the He canister and regulator increases the net depth by 3.8 cm and the weight by 0.34 kg. In Figure 4.2d, the microcomponent carrier PCBs are shown (*sans* microcomponents) mounted on stand-offs to a single, easily removable base-plate PCB. Beneath this PCB are, in order, the microcomponent control PCB, the DAQ card, and the fluidic control PCB. The custom-machined stainless-steel valve manifold, located beneath the base-plate PCB, was tapped with 1/16" Valco threads which accept fused silica capillary when used with graphite ferrules. The top face of the manifold was machined to accept the 5 face-mount, 3-way, latching solenoid valves (Model# LHLA1221111H, Lee Co., Westbrook CT). A commercial mini-pump (NMP 09M, KNF Micro AG, Reiden, Switzerland), internally mounted on the box wall, was used to collect air samples. Two miniature needle valves (Beswick Engineering, Geenland, NH) were mounted to the font panel of the enclosure (Figure 4.2e) to permit manual adjustment of the sampling flow rate and injection split ratio. The He canister (13.5 cm long and 4 cm in diameter, 2.5g of helium) and accompanying regulator (Leland Gas Technologies, South Plainfield, NJ) were mounted to the exterior of the rear panel of the enclosure (not visible in Figure 2e).

Sections of deactivated fused silica capillary (250 µm i.d.) and 1/16" stainless-steel tubing were used for fluidic interconnections throughout the system. Voltage regulators for actuating the pump and solenoid valves were mounted to the inside of the front panel to facilitate access. One small axial fan was placed on the right-facing panel and a series of vent slots were included in the bottom panel of the enclosure for cooling the lower PCBs. Two additional axial fans were installed on the front-facing panel adjacent to the microcomponents, and slotted vents were cut into the rear panel to facilitate cooling of the µPCF and the µcolumns after each analysis. 24V DC power was provided through an AC-to-DC converter connected to wall power.

Fluidic connections between microsystem components were made via press-tight unions (Supelco, Bellefonte, PA) wrapped in polyimide-embedded resistive film heaters (Omega Engineering, Stamford CT) to eliminate cold-spots. A constant voltage was applied to these heaters, which maintained connections at ~100 °C. The He canister is projected to provide a minimum of 280 analytical runs, or roughly 46 hours if analysis are performed once every 10 minutes, or 37 hours if analysis are performed once every 8 min, assuming a combined 50 mL of He used per analysis for both analytical separation (3 mL/min for up to 10 minutes) and purging of the fore-line (up to 20 mL). For the testing presented here, however, a conventional 110 L compressed gas cylinder of He was plumbed to the bulkhead fitting which would otherwise accept the outlet from the canister. Head pressures necessary to achieve 3 mL/min through the analytical system, un-split and split, were 18 and 23 psi, respectively.

4.3.6. Electronic design rationale

This section was contributed by fellow Zellers lab member Nicolas Nuňovero. Although PEMM-1 is AC powered, an external AC-DC converter was used to match the DC operating voltage to be used in the PEMM-2 prototype. A set of adjustable high efficiency DC-DC converters were employed to supply the range of voltages required for each system component. Chassis mounted step-down converters were selected for powering the Manifold Board, µCR sensors, interconnection heaters and micro-sampler. Step-up voltage regulators, originally conceived to supply power to the µPCF and µcolumns to meet their high voltage demands during ramping, were discarded due to noise in the temperature sensors affecting the temperature control stability. For low signal circuitry, an electrically isolated DC-DC converter with regulated output was employed.

Regarding data acquisition and control subsystem, a single DAQ board was identified to provide enough features to meet all acquisition and control requirements. New electronic signal handling circuits were needed to help improve sensor parameters like resolution and dynamic range, which were important given the anticipated exposure scenarios. For this purpose MEMS board containing the µCR signal conditioning circuitry was redesigned. Additional features of this board were related to the micro-components electronics, including the RTD measurement interfaces, and heater actuation for the micro-column, micro-sampler and µCR array. The manifold PCB board was dedicated to actuating other fluidic components like the pump, valves and fans. A labeled engineering schematic of the Gen-1 PEMM is presented in Figure 4.3.

The enclosure layout diagram in Figure 4.3 shows the positions of cut-outs for ventilation and mounting of components. A commercial enclosure was purchased and subsequently modified via precision water-jet machining for tailored mounting of components. Readouts for voltage regulators simplify voltage adjustment for each component. Outlet from manifold was designed to facilitate connecting to a downstream FID for calibration checks. This figure is courtesy of Nicolas Nuňovero.

4.3 Results and Discussion

4.3.1 System design and operational specifications

Several performance criteria specific to the intended application had to be established at the outset in order to rationalize the design, integration, and operation of the instrument components. Since most of these were discussed in detail in the previous chapter (and our recent article on the µPCF developed for this system),[44] only the more salient points will be presented here. The primary criterion used to place boundaries on the target VOCs was that they had to fall within a p_v range of ~0.03 to 13 kPa. Less volatile compounds would likely adhere to surfaces in the fluidic pathways and more volatile compounds would be difficult to trap, separate, and detect. Where possible, target VOCs were chosen that also had assigned Threshold Limit Values (TLV®),[67] which are generally in the high-ppb to mid-ppm range, and which serve as reference values for specifying the range of concentrations to be encountered. The selection of interferences was not subject to any particular constraints; for testing purposes we chose to include one representative compound with p_v values higher than the target range specified above, dichloromethane. In regard to the nature and number of target VOCs to include in a particular analysis, of course, this would change with the specific exposure scenario presented by a given workplace. A mixture comprising 15-20 VOCs was selected with the understanding that this mixture complexity was somewhat arbitrary as actual workplace exposures may comprise greater or fewer components in practice. Table 4.1 lists the set of target VOCs used in this study, along with their p_v values and TLV values.

The second criterion of concern in the design was the sampling volume (as discussed in Chapter 3), which must be sufficient to exhaustively capture enough mass of each analyte to accurately quantify without inadvertently causing saturation of the detector, as saturation invariably invalidates quantifications. Assuming a limit of detection (LOD) of ~5 ng for the µCR sensors on the basis of previous studies[53,54,56,60] and further assuming that 0.1×TLV is a suitable minimum concentration to measure, the minimum sample volume would then depend on the target VOC with the lowest TLV value. For benzene, with a TLV of 0.5 ppm, reaching the 0.1×TLV level would require a minimum air sample of 32 mL, whereas for heptane, with a TLV of 400 ppm, it would require less than 0.1 mL. (NOTE: we are assuming here that measurements can be made at the LOD, however in practice limits of quantification, which typically established at 3×LOD or 10×standard deviation of signal noise, would be used). These volumes are intended to highlight the variability in necessary sampling volumes established using exposure limits, not to set these volumes for the example targets. Assuming that accurate quantification is important up to, say, 2×TLV, which would represent a fairly high concentration, this would correspond to 1.0 ppm for benzene and 800 ppm for heptane. If we further stipulate that these concentrations must generate responses that are >10×LOD, then the required sample volumes would be the same as those quoted above for 0.1×TLV levels.

The dilemma faced in trying to reconcile sample volumes and/or the required dynamic range of the analytical system with such widely disparate exposure limits was discussed in our previous report, and remains unresolved. However, in an attempt to compromise, we proposed developing two operating modes for the instrument, geared towards either relatively low or high VOC concentration environments. While definitive delineations of “low” and “high” concentrations have not yet been established, for the latter we have set a provisional minimum sample volume of 10 mL, such that even in the presence of co-contaminants, benzene could still be measured at its TLV, with a signal corresponding to 3×LOD, while maintaining an acceptably low risk of saturation due to excessive captured masses of other VOCs. Flow rates during sampling and separation are obviously another consideration, as was discussed in Chaper 3.

The third major criterion of the design was to minimize the size, weight and power consumption of the ultimate belt-mountable PEMM-2 unit without sacrificing analytical performance. Although PEMM-1 is AC powered and designed as a bench-top unit, an external AC-DC converter was used to match the 2V DC operating voltage of the PEMM-2 prototype, and the fluidic components are nearly identical in size to those to be used in the PEMM-2 prototype. A variety of power- and size-saving compromises were employed to accomplish this goal, including the selection of electronic components, carrier gas, fluidic plumbing materials and fittings, valves, and the internal box ventilation strategy.

In order to meet the above three criterion, several design decisions had to be made at the outset. Among these was the selection and design of components. Previous studies were consulted in considering the adsorbent materials to use in the μPCF, the stationary phase coating and thickness to use in the μcolumns, the length of the μcolumns, the MPN coatings to use for the μCR arrays, and the number of μCR sensors to include in the array.[40,41,43-45,49-51,54,56,60] In light of that work, we selected the graphitized carbons C-X and C-B as suitable adsorbent materials to use in the dual-cavity μPCF. C-X has a surface area and adsorptive strength suitable for both quantitative capture and efficient desorption for VOCs with p_v values from ~4.0 to 13 kPa, while C-B's slightly lower surface area and weaker adsorptive strength make it suitable for VOCs with p_v values from ~0.01 to 4 kPa. Both are hydrophobiv, and viable for hundreds of repeated heating cycles, and stable at temperatures beyond 300°C with minimal off-gassing or thermal decay.[60]

Polydimethylsiloxane (PDMS) was chosen as the stationary phase for the μcolumns as it is suitable for separating a wide range of non- and moderately-polar analytes, easily applied, resistant to bleed when cross-linked, and stable at the operational temperatures anticipated here (less than 200°C). The MPN film coatings were chosen based on a combination of film stability/longevity, ease of coating, and chemical diversity in an effort to impart high sensitivity and selectivity.

In the subsequent sections, results of characterizations of the individual components and the sub-systems (comprised of abbreviated groups of components) are presented independently, followed by discussions relating their performance to that of the full system. Injection, separation and detection conditions are evaluated, with careful examination of the competing influences flow rate, carrier gas, injection split ratio, and temperature have on the overall sensitivity, chromatographic resolution, analytical duty cycle, and use of consumables. Compromises of this nature were at the heart of this development effort, and in many cases advantages were difficult to discern. These discussions are followed by critical evaluations considering how these results are likely to influence the design and operation of the Gen-2 PEMM system. While not discussed in great detail here, the design of the electronic circuitry and selection of individual electronic components underwent similar evaluations.

4.3.2 μPCF characterization

The dynamic adsorption capacities and desorption efficiencies for representative VOCs were determined previously at relevant concentrations and sample volumes using the predecessor to the current μPCF device.[44] Since the adsorbent masses tested and fluidic layout of this new μPCF are the same those in the previous study, the capacities and desorption efficiencies were not re-confirmed in this study. Tests of injection bandwidth were also performed with the previous device, but since the capacity and heater design of the new μPCF differed from those of the previous device, a limited set of tests of this performance parameter was conducted. Benzene, toluene and n-dodecane were used as the analytes because they span the range of target-VOC p_v values for which the instrument was designed. Tests were performed at 3 mL/min analytical flow rate under splitless and 2:1 split ratio conditions; example split injections are presented in Figure 4.4.

Specifying a *minimum* sampling flow rate required placing a limit on the time allotted for this step in the duty cycle of the instrument. For the latter, we settled on 1 sample every 10 min as a provisional specification. Anticipating between 4-5 min for injection/separation/detection and roughly 2 min for backflushing and re-setting parameters after each analysis, 3-4 min could be allotted to sample collection. For sample volumes of 10 to 35 mL, the range of minimum flow rates would then be 2.5 to 9 mL/min. The *maximum* sampling flow rate would then be dictated primarily by considerations related to LODs and minimum bed residence times within the µPCF. As presented in Chapter 3, the latter is a more stringent criterion, which for the cavity sizes of the devices available for this study this would correspond to a flow rates <= 14 mL/min. Other factors, such as internal flow-path resistances may ultimate dictate the maximum flow rate.

The values of full width at half maximum (*fwhm*) of peaks measured with splitless injection were 0.94, 1.0, and 1.4 sec, for benzene, toluene and n-dodecane, respectively. Asymmetry factors were 1.1, 1.7 and 2.3, respectively (splitless injection). With a 2:1 split (i.e., a desorption flow rate of 9 mL/min and an analytical flow rate of 3 mL/min), the *fwhm* values decreased to 0.59, 0.79, and 0.85 sec, respectively. These values are somewhat smaller than those observed with the previous device, despite the larger bed attesting to the improved heater design of the new device. These improvements are likely attributable to the optimized design of the heater. The similarity in the fractional reductions in *fwhm* values among the vapors at the higher desorption flow rate indicates that they are all being thermally desorbed with similar efficiency, and that the injection bandwidth is flow rate limited.[65] The sharp injections for benzene and toluene are particularly important for achieving good chromatographic resolution, since the n-dodecane and compounds of similar volatility, would benefit from on-column focusing, as discussed in Chapter 3. Thus, in those cases where separation is more important than sensitivity, the split injection would be advantageous. It is worth noting, however, that the fractional increase in resolution (roughly 25 - 50%) is less than the fractional decrease in sensitivity (-67%), as found in our previous studies.[44,56]

4.3.3 µColumn characterization

Selecting the carrier gas was the first step in evaluating the µcolumns, as it has implications for both chromatographic performance and system integration. Ambient air has been used in portable instruments because it eliminates the need for a consumable resource and reduces the overall footprint of the system.[60,62] However, the scrubbers required to remove contaminants and ambient humidity have finite service lives, and can add significant size and weight to the overall unit. Furthermore, the chromatographic efficiency of air is much less than that of more diffusive gases such as helium (He) or hydrogen at flow rates beyond the optimal flow velocity (i.e., as defined by the Golay minimum), which is where most separations are conducted.[66] As such, on-board tanks of compressed carrier gas are an attractive alternative, despite their size and weight, and the downside of introducing a consumable resource.

In order to properly select a carrier gas for the system, the chromatographic performance was characterized using both N_2 and helium. Prior to system integration, the dual ensemble of µcolumns was installed inside the oven of a bench scale GC, and connected between the GC inlet and FID. Gas-tight syringe injections of a vapor-phase mixture of methane and n-octane were made at each of several flow rates in both N_2 and He carrier gases with the GC oven held at 30°C. The plate height, H, was calculated at each flow rate by standard methods,[66] and the resulting Golay plots, presented in Figure 4.5, yielded optimal flow rates of 0.17 and 0.56 mL/min for N_2 and He, respectively. The maximum plate count, N, was about 4,300 plates/m for both carrier gases.

Evident from the Golay curves is the greater loss of in chromatographic efficiency (i.e., increase in H) of N_2 compared with helium, at higher flow rates. At the anticipated system flow rate of 3 mL/min, the H values were approximately 0.65 and 0.17 for N_2 and He, respectively (see dashed vertical line in Figure 4.5), and the corresponding values of N (number of theoretical plates, see Chapter 1) were 150 and 570 plates/m. The ~4-fold greater value of N at the operating flow rate argued strongly for using He as carrier gas. Furthermore, helium maintains the chromatographic performance over a wider range of flow rates, which made it both the more appropriate choice for separations at 3 mL/min and also the more versatile choice, allowing the ultimate PEMM-2 to be used under a variety of flowrate conditions.

From an engineering perspective, using He eliminated the need for an air scrubber and reduced the overall power dissipation by reducing pumping time. It would also allow for a simpler manifold and valve layout (in the PEMM-2) as the single pump was not required to function in both pull and push directions. This is, however, offset by addition of the on-board gas tank and the associated regulator. The need for its periodic replacement is anticipated to be less of shortcoming than is the need to replace scrubbers were ambient air to be used as the carrier gas.

The wide range of VOC concentrations encountered in the occupational environment demanded that the system be capable of analyzing samples spanning a wide range of injected masses. Theoretically, the *fwhm* of any peak is independent of the injected quantity of an analyte as long as the sorption/desorption equilibrium between the stationary and mobile phases is maintained (holding all else constant, including injection bandwidths and separation conditions). If the column becomes overloaded to the point where there is excess analyte in the mobile phase, then the *fwhm* should increase from the resultant peak tailing.[66]

Separations were conducted isothermally at 50°C at 3 mL/min with 1:100 split injection, of different volumes, for a mixture of neat benzene, toluene, and n-dodecane over a range of increasing injected masses using conventional GC inlet by an autosampler fitted with a 0.5µL syringe. Injected masses, measured by the downstream FID, ranged from 0.15 to 30 µg. The resulting *fwhm* values are plotted in Figure 4.6a. For benzene and toluene, the *fwhm* values were constant up to about ~8 µg injected and then increased slightly up to the maximum injection of 30 µg. The increase in the *fwhm* values was rather small, however, even at 30 µg (i.e., 65% increase). This makes sense, as VOCs in this volatility range have relatively small equilibrium constants (K), with relatively small fractions of analyte partitioning into the stationary phase at any discrete point, as evidence by their short retention times.

For n-dodecane, with a substantially larger equilibrium constant, the *fwhm* was constant up to ~5 µg and then showed a sharp increase with higher injection masses. The mass of a volatile analyte, such as benzene, in the mobile phase necessary to saturate the stationary phase at equilibrium is much higher than what would be necessary for a less volatile compound, such as n-dodecane. Of course, temperature is an important co-variable, as higher temperatures would tend to reduce the dependence of the *fwhm* on mass injected because it would shift the equilibrium in favor of the mobile phase, with less of all analytes partitioning into the stationary phase. Since all separations will be temperature programmed, the influence of this factor could vary over the course of a separation; benzene would probably elute completely before a column temperature of 50°C would be reached, whereas n-dodecane would likely elute at a higher temperature, reducing the ultimate impact of this increase in *fwhm*.

To evaluate the effect this increase in *fwhm* had on chromatographic resolution, the experiment above was repeated, under the same GC conditions, using a close-eluting pair of relatively volatile compounds, benzene and trichloroethylene. Results are presented in Figure 4.6b. Although the resolution, R_s, remained >2.5 under all conditions, above ~8-10 µg, R_s started to drop fairly sharply

Taken together, these data provide some confidence that injections smaller than 5-8 µg, would not result in significant reductions in chromatographic performance due to column overloading. For an anticipated default sample volume of 10 mL, 5 µg would correspond to an air concentration of 500 mg/m^3, which >TLV for most, but not all, compounds (e.g., toluene has a TLV of 20 ppm, or 75 mg/m^3, whereas heptane has a TLV of 400 ppm, or 1600 mg/m^3). This confirms that the upper bound in dynamic range of the µcolumns could be a problem, however with the use of a split injection, these masses could be significantly reduced, eliminating this concern. Thus, the design of the columns, specifically the stationary phase film thickness, is sufficient for the anticipated mass loading range.

4.3.4 µCR array characterization

As is evident from this and following sections, numerous µCR devices were tested prior to the final characterization presented below, with many exhibiting unusually poor signal to noise ratios. The µCR device chips, the fluidic lids, and three of the five MPN films used in these arrays were new at the outset of the study, and had yet to be characterized or optimized, and as such, much of what is presented here was preliminary work on these devices. Coating the arrays initially proved quite difficult; several of the MPNs tended to yield unstable high resistance films that generated broad asymmetric peaks when used in conjunction with chromatographic columns, as can be seen in Figure 4.10 and Table 4.2 (discussed in further detail in later sections). Noise levels of these sensors were also extremely high, reducing sensitivity and chromatographic resolution. Identification numbers of the arrays used in these characterizations are presented in the figure captions to help clarify which procedures yielded the most effective results. These difficulties were attributed to poor adhesion of the electrodes on the glass substrate resulting from problems during the fabrication process. The metallization on the µCR arrays was faulty, giving rise to unreliable readings in numerous devices. Early tests of these µCR arrays also revealed that application of an epoxy adhesive to bond the fluidic lid to the sensor chip surface caused sensor baseline resistances to rise irreversibly upon heating, even for films that had been stable prior to this step. This observation was attributed to off-gassing of free-radical initiators from the epoxy adhesives, which appear to react irreversibly with the nanoparticle sensor films (hypothesized by Dr. William Steinecker). In subsequent µCRs, lids were affixed with 50µm double sided sticky tape, and sealed with an outer layer of epoxy, similar to the method used in older versions of the device in which these problems were not encountered. The buffer between the sensors and the epoxy proved to be effective as sensors sealed in this manner exhibited greater baseline stability and longer overall lifetimes. Efforts by Dr. Chengyi Zhang to purify the MPN materials and optimize the coating procedures, by Dr. William Collin to de-activate the surface of the sensor chips, by Henry Zhan to re-fabricate the µCR array chip devices, and by Junqi Wang to characterizing the subsequent batches of devices, were instrumental in resolving the above mentioned issues. The data presented here, however, was collected prior to the resolution of many of these problems, and is thus subject to several additional sources of variation than is expected to be typical of these Gen-2 µCR array devices.

A Gen-2 µCR array coated with C8, EOE, TEG and OPH (lidded and plumbed) was calibrated using a conventional benchtop GC equipped with a 6-port valve. The sensor array was placed inside the GC oven, maintained at 30^0C, and plumbed between a 6-m commercial PDMS column upstream and a calibrated FID for reference downstream. Static test atmospheres of methyl ethyl ketone (MEK), ethanol (EOH), n-heptane (HEP), and toluene (TOL) were injected via the 6-port valve to calibrate the array; the resulting calibration curves of peak area vs. injected mass are presented in Figure 4.7a-d. Responses were linear for this array, however peak shapes (not shown) were abnormally broad for the TEG and OPH sensors. Despite the high noise, LODs for the most sensitive sensor in the array (typically EOE or C8) ranged from 0.5-1.1 ng, consistent with those presented in Chapter 2 for the Gen-1 µCR devices. For the least sensitive sensor in the array (TEG, in all cases), LODs ranged from 1.9-9.8 ng. Given the preliminary nature of this characterization and the greater-than-expected noise in the signals, it is anticipated that on-going work to optimize the devices and coating techniques (as discussed above) will improve the signal to noise ratio and LODs of these sensors.

4.3.5 Thermal and analytical stability

The PEMM-1 prototype was then assembled, enclosed (lid on), and run through a series of sampling and analytical cycles. Since all of the functions performed by the microsystem components are temperature dependent, maintaining strict temperature control is essential to ensuring stable performance. For the initial series, a blank static test atmosphere of N_2 was sampled for 1 min at 10 mL/min. Valves were then thrown to begin the analytical cycle. He flow, 3 mL/min measured at the outlet, was actuated, the µPCF was heated to mimic (splitless) injection, and the µcolumns temperature program was initiated. Column 1 was ramped at 5°C/min from an initial 30°C to 35°C (1 min), then 75° C/min to 110 °C (1 min), then 20°C/min to 150 °C (2 min), and column 2 was ramped at 5°C/min from an initial 30°C to 35°C (1 min), then 85° C/min to 125 °C (1 min), then 15°C/min to 150 °C (2 min). The full analytical cycle lasted 4 min. Upon reaching the maximum µcolumn temperature, the run was concluded and the instrument was allowed to cool for 3 min, during which time two dedicated fans across from the µPCF and µcolumns, respectively, were activated to facilitate cooling prior to repeating this sequence (this time was selected to ensure all components were below their required initial setpoints). This 8-min (1 minute sampling, 4 minute analyses, 3 minute cooling) was repeated 22 times over the course of 3 hours; RTDs in the system and the thermocouple on the fluidic carrier plate were monitored during the analysis phase (during the temperature program).

The internal temperature is important because higher temperatures of the µPCF reduce the adsorptive capacity of the device. In order to maintain the necessary breakthrough volumes for the intended application, the temperature of this device, and thus that of the internal enclosure, must be maintained at or below 30 °C. Similarly, the reproducibility of the µcolumn temperature ramps is critical for chromatographic retention times. The sensitivities of µCR arrays are also influenced by temperature; thus consistency of the µCR temperature is essential for accurate quantification.

The fidelity of component temperatures to their set point temperatures was assessed. Results from a representative run, about midway through the 22 run series, are shown in Figure 4.8. This temperature program was selected to highlight a scenario in which both low and high volatility analytes would need to be analyzed in a single sample. The 30 °C initial set point of the columns and the slow initial ramp for the first minute of the analysis are required for the separation of high-volatility mixture components. The subsequent faster ramps of 75°C/min and 85°C/min were selected to demonstrate the capability to heat rapidly and accurately. The slower ramps at the end of the separation are typically used for separations of mixtures containing low-volatility analytes, such as dodecane. The final temperature of 150 °C is the highest anticipated column temperature to be used in any separation with PEMM 1.

During the sequence presented above, the temperature, of the fluidic carrier plate rose by approximately 3-4 °C in sync with the temperatures of the µcolumns, indicating the µcolumns had the greatest impact on internal system temperature. Overall, these results suggest that under typical operation in an air conditioned environment with a maximum µcolumn temperature of 150 °C, the internal box temperature would not exceed 30 °C. Active cooling of the devices further reduced the temperature of the µPCF during sampling to roughly 27-28 °C during the above sequence of runs. There was no cumulative drift over the course of the experiment.

The run to run variability in the temperature ramps of the µcolumns was measured by comparing the temperature at a specific time points in each analysis. Relative standard deviations (RSD) in the temperature measurements at each second were calculated. The average RSD was less than 3% for both µcolumns. The influence this variability had on retention times is presented in the next section. While variability was low, deviation from the applied ramp, was apparent at the beginning of each new ramp rate. As can be seen in Figure 4.5, small ‘humps’ in the temperature ramp for both µcolumns at 0 and 2 minutes indicate a small over-shoot in the slow ramps. These are apparently an artifact of the voltages used in the pulse width modulation algorithm used to control the temperatures of these components. Due to the highly reproducible nature of these deviations, their impact on retention times is low.

The µCR array was held at 30 °C using a constant voltage supply applied to the heater on the back-side of the chip whenever the unit was turned on. Pulse width modulation was initially considered as a means to save power and control the temperature more finely, similar to the temperature control of the other fluidic components. However this increased µCR output noise and was thus abandoned. After an initial warm-up time of 10-15 minutes during which the µCR was allowed to reach a steady-state, the temperature of the array was stable. It was anticipated that since the temperature of the array was not actively controlled, it would rise and fall with the fluctuations of the enclosure. However, during the typical 4 minute analysis presented above, the relative standard deviation in the temperature was 1.7% (ranging from 29.8 to 30.2°C). There was no trend in this variation; it did not track the temperature of the enclosure or the µcolumns. This extremely small shift in temperature is likely attributable to the engineered thermal isolation of the device, which is suspended above the fluidic carrier and shielded inside a metallic faraday cage with no circulating air. No insulation was added to the enclosure walls, however this could be added to reduce thermal variation.

These temperatures and temperature variations are obviously influenced by the ambient environment, thus requiring the caveat above that the instrument is intended for operation inside air conditioned environments. A wide range of external factors of the ambient environment, including the effect of humidity and dust among others, which are typically evaluated for manufactured products, were not tested here. Furthermore, it highlighted that the µPCF device cooled down while in close proximity to the hot µcolumns. Similarly, the reproducibility of the µcolumn temperature programs and the stability of sensor array temperature during analysis ensure accurate identification and quantification.

It is difficult to estimate a minimum analytical cycle time from these data as the temperature program would depend heavily on the composition of the mixture. For mixtures requiring high column temperatures similar to that tested here, 3 minutes is a safe window to ensure the temperature of each fluidic component and that of the internal temperature of the enclosure are sufficiently low to initiate the following cycle. For mixtures requiring lower maximum column temperatures (comprised mostly of moderate and high volatility targets), shorter duty cycles would be possible given the shorter times necessary to cool components down.

4.3.6 System characterization

In order to establish a basis for comparison of chromatographic performance with the µCR array and FID and permit the evaluation of extra-column band broadening from the µCR array, fluidic performance was first characterized using an FID in lieu of the µCR array. The effluent from the second µcolumn was fitted directly to a downstream FID using a segment of unheated capillary. A static test atmosphere containing mixture of n-alkanes, from n-hexane to n-dodecane, was used to characterize retention time stability, sampling volume (mass) reproducibility, and peak widths across the volatility range of targets to be analyzed by the system (0.02-13 kPa). Samples from this static test atmosphere were loaded onto the µPCF, desorbed and injected (splitless) to the µcolumns, which were temperature ramped using the program shown in Figure 4.8. Press-tight unions between the µPCF and first µcolumn, and between the second µcolumn and FID, were maintained at 125 °C at all times, and interconnecting capillary between the µcolumns and FID was less than 10 cm.

Results of this characterization are presented in the left hand portion of Table 4.2. It is apparent that retention times using FID detection were very consistent, with RSD < 1% in all cases except for n-nonane. No trends in the retention times that would indicate additional sources of variation, such as carry-over, pressure or flow fluctuations, were observed. This low variability is a testament to the accuracy and reproducibility of the µPCF injection and the high-precision temperature ramps of the µcolumns. These data further demonstrate that there was no drift in the internal box temperature over time. *fwhm* for n-hexane through n-undecane were from 1.6-2.1 sec, with RSDs ≤5% in all cases. These values are consistent with values presented in Chapter 3, where splitless μPCF injections of VOCs with similar retention times were made to conventional columns and FID, suggesting that the separation performance of the μcolumns evaluated here is similar to conventional columns of the same length. *fwhm* values for n-dodecane (C12) were slightly larger and more variable than with the conventional column, with an average of 2.7 sec and RSD of 10.4%. This is most likely due to the low volatility of C12, and consequently adhesion to cold-spots along interior walls of the un-heated interconnecting capillary. Wall adsorption would also account for the slight increase in variability of the C12 peak area. According to chromatographic theory, peak widths for the low volatility VOCs are strongly influenced by the temperature ramp used and thus could be sharpened in cases where faster temperature programs or higher maximum temperatures are permitted.

The above test was repeated without heating one or the other press-tight unions connecting the μcolumns to the μPCF and μCR array, to evaluate the effect. Since these press-tight union heaters demand a large amount of power, it was necessary to evaluate their relevance to the chromatographic performance of the system. When the union between the μPCF and μcolumns was left unheated, no change in *fwhm* was observed for any of the 7 compounds (n-hexane through n-dodecane). This makes sense, as the first μcolumn was held at 30°C for the first 30 seconds of the chromatogram. It was concluded that the more volatile fraction of analytes do not adhere to the uncoated union at these temperatures, and the less volatile fraction of analytes undergo on-column focusing upon reaching the μcolumn, reducing any extra column band broadening due to the transfer capillary.[19,22] When the union between the μcolumn and FID was left un-heated, *fwhm* for n-nonane, n-decane, n-undecane, and n-dodecane increased by

2.8%, 7.0%, 12% and 21%, respectively (no change in *fwhm* was observed for n-hexane, n-heptane or n-octane). The change in *fwhm* for n-nonane was within the RSD (see Table 2), however did exhibit the same trend as the less volatile vapors. This suggests that for mixtures containing only analytes with vapor pressures >0.59 kPa, the cold spot created by leaving the second union unheated is insignificant, thus allowing for a notable power savings. However, for analytes with vapor pressures <0.59 kPa, the unheated union introduces a significant source of extra column band broadening.

Following the above, the FID was replaced with a µCR array (not the same as that calibrated in a previous section), and the same alkane mixture was analyzed again. Flow rate at the µCR array chip was set to 3 mL/min to permit comparison with results above. The results of these tests for the best sensor in the array (EOE) are shown in the right-hand portion of Table 4.2. Here, performance was much poorer than expected. The µCR was a significant source of band broadening, yielding peaks that were both broad and asymmetric. Compared with FID results, retention times, on average, increased slightly, in most cases by only a few seconds. The RSDs of the retention times, however, increased by 2 to 5 fold, particularly for the less volatile analytes. Peak area variation increased 4 to 8 fold, with RSDs from 8.7% to 22%, again with the larger variances observed for the less volatile analytes. The signal to noise ratios for this particular array was lower than anticipated, which likely contributed to the variation in peak area observed here. Responses from the EOE channel were, however, sufficiently large to make accurate measurements. Peak widths increased inversely with vapor pressure, with no change for hexane, and a nearly 5 fold increase n-undecane.

As presented above, peaks measured using the µPCF and µcolumn devices with FID had significantly lower variability and narrower peak widths than those measured by the µCR array.

While this initial µCR device is not considered entirely representative of µCR array performance in general, due to problems discussed above with coating and fabrication, these data still bear brief discussion. The increasing variations in peak width from the µCR array for larger alkanes suggest the sensors are heavily influenced by the vapor pressure of the target analyte. Differences in peak width across sensors in the array could not be monitored in these trials because only the EOE channel for CZ-01-035 had a signal to noise ratio sufficiently large to permit accurate measurements.

Prior to the above characterization of peak width, an initial test of the following 8 VOCs was analyzed, each at ~25 ppm: benzene, trichloroethylene, methyl isobutyl ketone, toluene, butyl acetate, ethyl benzene, o-xylene, and cumene. The sensor employed here was lidded directly with epoxy, without the double-sided adhesive tape, and thus experienced a dramatic rise in baseline resistance shortly after this test was performed. Only data from the OPH sensor are presented, as this was the last sensor to remain within the operational resistance range. A 2 mL bag sample was collected on the µPCF and injected at a 2:1 split with a 5 second pause prior injection (in which flow was initiated 5 seconds prior to heating the µPCF device in an effort to stabilize the µCR baseline). This injection technique was used on prior µGC systems.[60,61] Results are presented in Figure 4.9. The premature desorption of high volatility targets, visible as small shoulders on the initial peaks, is attributed to the poor adsorption of these on the first bed of the µPCF, to which a small fraction of these analytes may have adsorbed during sampling. The greater desorption flow-rate used to achieve 2:1 spilt may also be a contributing factor. The problem was subsequently resolved by eliminating the pause prior to injection. Here, the average *fwhm* was 1.04 seconds, ranging from 0.93 sec for benzene to 1.44 sec for toluene. These peaks were considerably narrower than those for the early eluting components of the alkane mixture discussed in Table 4.2. These preliminary tests using an early array yielded the sharpest peaks of any array tested subsequently.

Finally, a complex, humid (RH~80%) mixture comprising 18 vapors was analyzed, using another μCR array; results are presented in Figure 4.10. The sample was analyzed using a 2:1 split injection. Results from the best sensor of each MPN type are included in the composite chromatogram in Figure 4.10. As has been observed before, peaks from the more polar analytes methyl isobutyl ketone and 1-pentanol were broader and more asymmetric than other peaks in the chromatogram. The large peak that elutes before compound 1 is believed to be water vapor. The accuracy and reproducibility of quantifications was not investigated here, however are currently being evaluated as part of the future work of this study.

Here, as is most typical of these sensor coatings, the C8 sensor yielded the sharpest and most symmetric peaks. This sensor was not in the front of the linear array, in fact the position of a specific sensor along the linear flow-path inside the array did not appear to have an influence on the broadness of the its peaks in any way. This suggests that peak width is mostly related to the desorption dynamics of that sensor, not the sharpness of the incoming analyte pulse. Reversing the fluidic direction of the array did not have a significant influence on peak width. The OPH channel used here yielded uncharacteristically broad peaks (see Figure 4.9 for example). This array was one of the first to yield a high signal-to-noise TEG channel, with only moderate peak asymmetry. As this was one of the previously un-tested MPN functionalities that had initially presented difficulty during coating, this was a significant demonstration. This author anticipates that in a practical setting, only the results from the sharpest sensor (in this case C8) would be used for quantification; input from other sensors would be used to aid in identification (using response patterns and/or relative response ratios).

Normalized response patterns for benzene, methyl ethyl ketone, 1-pentanol, ethylbenzene and n-undecane, calculated from peak height, are presented above Figure 4.10. The C8 signal predominates for n-undecane, benzene and ethylbenzene, while TEG and EOE predominate for methyl ethyl ketone and 1-pentanol, as is common for these devices. The OPH channel of this particular array had very low sensitivity, and as such it did not contribute significantly to the patterns. Overall, response patterns were similar for the aromatics and alkane, and differed for the two more polar compounds.

4.4 Conclusions

We conclude that the Gen-1 PEMM laboratory prototype µGC described in this report is capable of multi-vapor separations at concentrations relevant to workplace applications and that the frequency of measurements and range of VOCs that are amenable to measurement with this instrument render it an effective new addition to the repertoire of exposure assessment tools available to occupational health scientists.

Each of the fluidic components was characterized individually, after which performance of the full prototype was demonstrated. Injection bands from the µPCF devices described here were sharper and more symmetric than those from the bulk heated µPCF presented previously, despite being 24% larger. Overall, chromatographic performance of the µPCF and µcolumn subsystem is sufficient to achieve baseline separation of mixtures of moderate complexity, up to roughly 15 compounds, in less than 3 minutes, with full analyses taking less than 7 minutes. Retention times were very consistent over the short term (10 cycles), with an RSD <1.5% when a FID was used as the detector, and <4% when a µCR was used as the detector. Limits of detection of the new Gen-2 µCR were comparable to those previously reported, however further optimization of coating strategies for this new device are likely to yield even lower LODs. Future work will seek to further investigate the reproducibility of quantification using the µCR array, as well as to evaluate a number of example exposure scenarios which will ultimately be used in a mock-field testing of the Gen-2 PEMM prototype currently under development.

The effect of injected mass on chromatographic performance was also evaluated. The dynamic range of the separation columns was evaluated to identify the point at which chromatographic performance decreased due to overloading of the stationary phase. Here, *fwhm* was shown to be independent of injected mass up to 5-8 µg beyond which peak widths broaden significantly. For high-concentration samples of analytes with similar volatility requiring similar column temperature programs to separate, it is imperative that single analyte mass loadings do not exceed this threshold, or chromatographic performance will decline.

Detection limits of the new fluidically integrated µCR array varied significantly (several additional calibrations were conducted, results of which were not presented). The preliminary results presented here yielded detection limits roughly the same as previously reported devices (those discussed in Chapter 2). Peaks from this detector were, however, shaper, for several of the arrays tested, particularly for examples where split injections were used. These data, however, must be viewed with caution, as other arrays tested yielded significantly broader peaks than previously tested. The yield on the fabrication of full devices was extremely poor overall.

This instrument has demonstrated improved analytical performance relative to prior µGC systems, with respect to volatility range of analytes tested, retention time reproducibility, overall size, weight, and power demand. While the system remains AC-powered, the knowledge gleaned from this effort has been instrumental in the development of the wearable, autonomous Gen-2 PEMM.

4.5 References

[1] National Institute for Occupational Safety and Health, *NIOSH Manual of Analytical Methods*, http://www.cdc.gov/niosh/docs/2003-154/ (accessed April 2016).

[2] Occupational Safety and Health Administration, *Sampling and Analytical Methods*, https://www.osha.gov/dts/sltc/methods/ (accessed April 2016).

[3] DPS Companion 600 GC, DPS Instruments, available at http://www.dps-instruments.com/DPS%20Companion%201%20Brochure.pdf (accessed July 2015).

[4] Gasmet DX4040, Gasmet Technologies, available at http://www.gasmet.com/products/portable-gas-analyzers (accessed April 2016).

[5] HAPSITE ER, Inficon, available at http://products.inficon.com/en-us/nav-products (accessed April 2016).

[6] D. H. Anna, Ed., *The Occupational Environment: Its Evaluation, Control, and Management*, 3rd Ed., Vol. 1, AIHA, Fairfax VA, 2011.

[7] S.C. Terry, H. Jermann, J. Angel, A gas chromatograph air analyzer fabricated on a silicon wafer, *IEEE Trans. Electron Dev.*, 26, 1880-1887, 1979.

[8] Griffin 824, FLIR, available at http://www.flir.com/threatDetection/ display/?id=63268, (accessed August 2015)

[9] I. Voiculescu, R. A. McGill, M. E. Zaghloul, D. Mott, J. Stepnowski, S. Stepnowski, H. Summers, V. Nguyen, S. Ross, K. Walsh, M. Martin, Micropreconcentrator for enhanced trace detection of explosives and chemical agents, *IEEE Sens. J.*, 6, 1094-1104, 2006.

[10] E. H. Camara, P. Breuil, D. Briand, L. Guillot, C. Pijolat, N. F. de Rooij, Micro gas preconcentrator in porous silicon filled with a carbon adsorbent, *Sens. Actuators B: Chemical*, 148, 610-619, 2010

[11] R. P. Manginell, D. R. Adkins, M. W. Moorman, R. Hadizadeh, D. Copic, D. Porter, J. M. Anderson, V. M. Hietala, J. R. Bryan, D. R. Wheeler, K. B. Pfeifer, Rumpf, A., Mass sensitive microfabricated chemical preconcentrator, *J. Microelectromech. Syst.*, 17, 1396-1407, 2008.

[12] M. Y. Wong, W. R. Cheng, M. H. Liu, W. C. Tian, C. J. Lu, A preconcentrator chip employing µ-SPME array coated with in-situ synthesized carbon adsorbent film for VOCs analysis, *Talanta*, 101, 307-313, 2012.

[13] E. H. Camara, P. Breuil, D. Briand, L. Guillot, N. F. de Rooij, C. Pijolat, A micro gas preconcentrator with improved performance for pollution monitoring and explosives detection, *Analytica Chimica Acta*, 688 (2), 175-182, 2011.

[14] G. Frye-Mason, R. Kottenstette, P. Lewis, E. Heller, R. Manginell, D. Adkins, G. Dulleck, D. Martinez, D. Sasaki, C. Mowry, C. Matzke, L. Anderson, Hand-held miniature chemical analysis system (µChemLab) for detection of trace concentrations of gas phase analytes, *Proc. Micro Total Analysis Systems (µTAS) Workshop*, Enschede, Netherlands, May 14-18, pp. 229-232, 2000.

[15] H. Noh, P. J. Hesketh, G. Frye-Mason, Parylene gas chromatographic column for rapid thermal cycling, *J. Microelectromech. Syst*, 11, 718-725, 2002.

[16] G. Lambertus, A. Elstro, K. Sensenig, J. Potkay, M. Agah, S. Scheuering, K. Wise, F. Dorman, R. Sacks, Design, fabrication and microfabricated columns evaluation of for gas chromatography. *Anal. Chem.*, 76, 2629-2637, 2004.

[17] A. Bhushan, D. Yemane, D. Trudell, E. B. Overton, J. Goettert, Fabrication of micro-gas chromatograph columns for fast chromatography, *Microsyst. Technol.*, 13, 361-368, 2007.

[18] S. Reidy, G. Lambertus, J. Reece, R. Sacks, High-performance, static-coated silicon microfabricated columns for gas chromatography, *Anal. Chem*, 78 (8), 2623-2630, 2006.

[19] M. Stadermann, A. D. McBrady, B. Dick, V. R. Reid, A. Noy, R. E. Synovec, O. Bakajin, Ultrafast gas chromatography on single-wall carbon nanotube stationary phases in microfabricated channels, *Anal. Chem.*, 78, 5639-5644, 2006.

[20] J.A. Potkay, G.R. Lambertus, R.D. Sacks, K.D. Wise, A low power pressure and temperature-programmable micro gas chromatography column, *J. Microelectromech. Syst.* 16, 1071–1079, 2006.

[21] D. Radadia, A. Salehi-Khojin, R. I. Masel, M. A. Shannon, The effect of microcolumn geometry on the performance of micro-gas chromatography columns for chip scale gas analyzers, *Sens. Actuators, B Chemical***,** 150, 456-464, 2010.

[22] S. Ali, M. Ashraf-Khorassani, L. T. Taylor, M. Agah, MEMS-based semi-packed gas chromatography columns, *Sens. Actuators. B*, 141, 309-315, 2009.

[23] H. Chen, J. Lu, B. X. Chen, A multidimensional micro gas chromatograph employing a parallel separation multi-column chip and stop-flow μGC× μGCs configuration." *Lab on a Chip*, 13 (7), 1333-1341, 2013.

[24] D. Gaddes, J. Westland, F. L. Dorman, S. Tadidagapa, Improved micromachined column design and fluidic interconnects for programmed high-temperature gas chromatography separations, *J. Chrom. A***,** 1249, 96-104, 2014.

[25] J. Liu, J. H. Seo, Y. B. Li, D. Chen, K. Kurabayashi, X. D. Fan, Smart multi-channel two-dimensional micro-gas chromatography for rapid workplace hazardous volatile organic compounds measurement, *Lab Chip***,** 13 (5), 818-825, 2013.

[26] R. Archibald, P. Datskos, G. Devault, V. Lamberti, F. U. Lavrik, D. Noid, M. Sepaniak, Independent component analysis of nanomechanical responses of cantilever arrays, P. *Analytica Chimica Acta*, 584, 101-105, 2007.

[27] M. Li, E. B. Myers, H. X. Tang, S. J. Aldridge, H. C. McCaig, J. J. Whiting, R. J. Simonson, N. S. Lewis, M. L. Roukes, Nanoelectromechanical resonator arrays for ultrafast, gas-phase chromatographic chemical analysis, *Nano Letters*, 10, 3899-3903, 2010.

[28] F. Y. Chen, W. C. Chang, R. S. Jian, C. J. Lu, Novel gas chromatographic detector utilizing the localized surface plasmon resonance of a gold nanoparticle mono layer inside a glass capillary, *Analytical Chemistry***,** 28 (11), 5257-2564, 2014.

[29] H. B. Zhu, R. Nidetz, M. L. Zhou, J. Lee, S. Buggaveeti, K. Kurabayashi, X. D. Fan, Flow-through microfluidic photoionization detectors for rapid and highly sensitive vapor detection, *Lab Chip*, 15(14), 3021-3029, 2015.

[30] M. Akbar, H. Shakeel, M. Agah, GC-on-chip: integrated column and photoionization detector, *Lab Chip*, 15(7), 1748-1758, 2015.

[31] R. S. Jian, R. X. Huang, C. J. Lu, A micro GC detector array based on chemiresistors employing various surface functionalized monolayer-protected gold nanoparticles, *Talanta*, 88, 160-167, 2012.

[32] K. Scholten, W. R. Collin,X. D. Fan, E. T. Zellers, Nanoparticle-coated micro-optofluidic ring resonator as a detector for microscale gas chromatographic vapor analysis, *Nanoscale*, 7, 9282-9289, 2015.

[33] J. A. Dziuban, J. Mroz,M. Szczygielska, M. Malachowski, A. Gorecka-Drzazga, R. Walczak, W. Bula, D. Zalewski, L. Nieradko, J. Lysko, J. Koszur, P. Kowalski, Portable gas chromatograph with integrated components, *Sens. Actuators A: Physical*, 115, 318-330, 2004.

[34] G. Frye-Mason, R. Kottenstette, P. Lewis, E. Heller, R. Manginell, D. Adkins, G. Dulleck, D. Martinez, D. Sasaki, C. Mowry, C. Matzke, L. Anderson, Hand-held miniature chemical analysis system (µChemLab) for detection of trace concentrations of gas phase analytes, *Proc. Micro Total Analysis Systems Workshop*, Enschede, Netherlands, May, 229-232, 2000.

[35] Y. T. Qin, Y. B. Gianchandani, iGC1: An integrated fluidic system for gas chromatography including knudsen pump, preconcentrator, column, and detector microfabricated by a three-mask process, *J. Microelectromech. Syst*., 23 (4), 980-990, 2014.

[36] M. Akbar, M. Restaino, M. Agah, Chip-scale gas chromatography: from injection through detection, *Microsystems and Nanoengineering***,** 1, 15039, 2015.

[37] P.R. Lewis, R.P. Manginell, D.R. Adkins, R.J. Kottenstette, D.R. Wheeler, S.S. Sokolowski, D.E. Trudell, J.E. Bymes, M. Okandan, J.M. Bauer, R.G. Manley, G.C. Frye-Mason, Recent advancements in the gas-phase µChem Lab, *IEEE Sensors J*., 6, 784-795, 2006.

[38] S. Zampolli, I. Elmi, F. Mancarella, P. Betti, E. Dalcanale, G. C. Cardinali and M. Severi, Real-time monitoring of sub-ppb concentrations of aromatic volatiles with a MEMS-enabled miniaturized gas-chromatograph, *Sens. Actuator, B Chemical*., 141, 322-328, 2009.

[39] M. Garg, E. Akbar, S. Vejerano, L. Narayanan, L C. Nazhandali, M. Agah, Zebra GC: A mini gas chromatography system for trace-level determination of hazardous pollutants, *Sens. Actuator, B: Chemical*, 212, 145-154, 2015.

[40] W. C Tian, S. Pang, C-J Lu, E. T. Zellers, Microfabricated preconcentrator-focuser for a microscale gas chromatograph, *J. Microelectromech. Syst*., 12, 264-272, 2003.

[41] W.C. Tian, H. K. L. Chan, C. -J. Lu, S. W. Pang, and E. T. Zellers, Microfabricated multi-stage preconcentrator-focuser for a micro gas chromatograph, *J. Microelectromech. Syst.* 14, 498-507, 2005.

[42] J. H. Seo, S. K. Kim, E. T. Zellers, K. Kurabayashi, Microfabricated passive vapor preconcentrator/injector designed for micro gas chromatography, *Lab Chip*, 12 (4), 717 – 724**,** 2012.

[43] T. Sukaew, E. T. Zellers, Evaluating the dynamic retention capacities of microfabricated vapor preconcentrators as a function of flow rate, *Sens. Actuators B: Chemical*, 183, 163-171, 2013.

[44] J. Bryant-Genevier, E. T. Zellers, Toward a microfabricated preconcentrator-focuser for a wearable micro-scale gas chromatograph, *J. Chrom. A.*, 1422, 299-309, 2015.

[45] G. Serrano, S. Reidy, E. T. Zellers, Assessing the reliability of wall-coated microfabricated gas chromatographic separation columns, *Sensors and Actuators: B Chemical*, 141, 217-226, 2009.

[46] S. J. Kim, G. Serrano, K. D. Wise, K. Kurabayashi, E. T. Zellers, Evaluation of a microfabricated thermal modulator for comprehensive two-dimensional gas chromatography," *Anal. Chem*., *83*,5556–5562, 2011.

[47] W. Collin, A. Bondy, D. Paul, K. Kurabayashi, E. T. Zellers, μGC × μGC: comprehensive two-dimensional gas chromatographic separations with microfabricated components, *Anal. Chem.*, 87 (3), 1630-1637, 2015.

[48] W.R. Collin, N, Nunovero, D. Paul, K. Kurabayashi, and E. T. Zellers, Comprehensive two-dimensional gas chromatographic separations with a temperature programmed microfabricated thermal modulator," *J. Chrom. A*, 1444, 114-122, 2016.

[49] Q. Zhong, W. Steinecker, E. T. Zellers, Characterization of a high-performance portable GC with a chemiresistor array detector, *Analyst,* 134, 283-293, 2009.

[50] F. I. Bohrer, E. Covington, C. Kurdak, E. T. Zellers, Characterization of dense arrays of chemiresistor vapor sensors with sub-micron features and patterned nanoparticle interface layers, *Anal. Chem.*, 83(10), 3687-3695, 2011.

[51] M. D. Hsieh, E. T. Zellers, Limits of recognition for simple vapor mixtures determined with a microsensor array, *Anal. Chem.* 76, 1885-1895, 2004.

[52] Jin, P. Kurzawski, A. Hierlemann, E. T. Zellers, Evaluation of multitransducer arrays for the determination of organic vapor mixtures, *Anal. Chem.* 80, 227-236, 2008.

[53] J. Bryant-Genevier, K. Scholten, S. K. Kim, E. T. Zellers, Multivariate curve resolution of co-eluting vapors from a gas chromatograph with microsensor array detector, *Sens. Actuator B: Chemical*, 202, 167-176, 2014.

[54] L. Wright, E. T. Zellers, A nanoparticle-coated chemiresistor array as a microscale gas chromatograph detector for explosive marker compounds: flow rate and temperature effects, *Analyst*, 138, 6860-6868, 2013.

[55] K. Scholten, X. Fan, E. T. Zellers, A microfabricated optofluidic ring resonator for sensitive, high-speed detection of volatile organic compounds, *Lab Chip*, 14 (19), 3873-3880, 2014.

[56] C-J. Lu, W.H. Steinecker, W-C. Tian, M.C. Oborny, J.M. Nichols, M. Agah, J.A. Potkay, H.K.L. Chan, J. Driscoll, R.D. Sacks, K.D. Wise, S. W. Pang, E.T. Zellers, First-generation hybrid MEMS gas chromatograph, *Lab Chip*, 5, 1123-1131, 2005.

[57] K. W. Scholten, W. R. Collin, X. Fan, and E. T. Zellers, Nanoparticle-coated micro-optofluidic ring resonator as a detector for microscale gas chromatographic vapor analysis, *Nanoscale*, 7, 9282-9289, 2015.

[58] W.R. Collin, K. W. Scholten, X. Fan, D. Paul, K. Kurabayashi, and E. T. Zellers, Polymer-coated micro-optofluidic ring resonator detector for a comprehensive two-dimensional gas chromatographic microsystem: μGC × μGC– μOFRR, *Analyst*, **2016**, 141, 261 – 269.

[59] W. Collin, , K.W. Scholten, D. Paul, K. Kurabayashi, X. Fan, E. T. Zellers, "μGC × μGC Microsystem with Resistive and Optical Detection," *Proceedings, Transducers '15,* June 21-25, Anchorage, AK, USA, 2015.

[60] S. K. Kim, D. R. Burris, H. Chang, J. Bryant-Genevier, and E. T. Zellers, Microfabricated gas chromatograph for on-site determinations of trichloroethylene in indoor air arising from vapor intrusion, part 1: field evaluation, *Env. Sci. and Tech.*, 46, 6065-6072, 2012.

[61] S. K. Kim, D. R. Burris, J. Bryant-Genevier, K. A. Gorder, E. M. Dettenmaier, E. T. Zellers, Microfabricated gas chromatograph for on-site determinations of trichloroethylene in indoor air arising from vapor intrusion, part 2: spatial/temporal monitoring, *Env. Sci. and Tech.*, 46, 6073-6080, 2012.

[62] W. R. Collin, G. Serrano, L. K. Wright, H. Chang, N. Nuñovero, E. T. Zellers, Microfabricated gas chromatograph for rapid, trace-level determinations of gas phase explosive marker compounds, *Anal. Chem.*, 86, 655-663, 2014.

[63] M. P. Rowe, K. E. Plass, K. Kim, C. Kurdak, E. T. Zellers, A. J. Matzger, Single-phase synthesis of functionalized gold nanoparticles, *Chem. Mater*. 16, 3513-3517, 2004.
[64] R.S. Jian, R.X. Huang, C. J. Lu, A micro GC detector array based on chemiresistors employing various surface functionalized monolayer-protected gold nanoparticles, *Talanta*, 88, 160– 167, 2008.
[65] J. Whiting, R. Sacks, Evaluation of split/splitless operation and rapid heating of a multi-bed sorption trap used for gas chromatography analysis of large-volume air samples *J. Sep. Sci.*, 29, 218-227, 2006.
[66] R. L. Grob, E. F. Barry, *Modern practice of gas chromatography,* 4th edition, Wiley Interscience, Hoboken, NJ, 2004, pp. 114-115.
[67] ACGIH, Threshold Limit Values for Chemical Substances and Physical Agents & Biological Exposure Indices for 2015, ACGIH, Cincinnati, OH, 2015.

Table 4.1. 18 test compounds with corresponding TLVs, comprising the hypothetical exposure mixture analyzed in Figure 4.10.

Peak #[a]	Compound	TLV[b] (ppm)
1	dichloromethane[c]	50
2	ethyl acetate	400
3	benzene	0.5
4	trichloroethylene	10
5	n-heptane	400
6	methyl isobutyl ketone	20
7	toluene	20
8	1-pentanol	-[d]
9	butyl acetate	100
10	ethylbenzene	25
11	3-heptanone	50
12	n-propylbenzene	-
13	1,2,4-trimethyl benzene	25
14	n-decane	-
15	nitrobenzene	1
16	n-undecane	-
17	1,2,4-trichlorobenzene	5
18	n-dodecane	-

[a] Peak assignments for chromatogram in Fig. 4.6b
[b] TLV-TWA;
[c] dichloromethane is a high-volatility interference
[d] No assigned TLV value

Table 4.2. Retention times, peak areas, and peak widths from PEMM 1with conventional FID on the left and µCR array detection (ID# CZ-01-035) on the right, of a 7-compond mixture of n-alkanes (C6-C12). Temperature program used here is presented in Figure 4.4.

		FID						EOE sensor of µCR array					
Compound	p_v (kPa)	t_R		Area		*fwhm*		t_R		Area		*fwhm*	
		Mean[a]	RSD[b]	Mean[c]	RSD	Mean	RSD	Mean	RSD	Mean[c]	RSD	Mean	RSD
hexane	17.6	29.2	0.5	2044	1.1	1.7	1.6	31.9	1.0	25.6	8.7	1.7	7.3
heptane	5.33	54.0	0.5	1232	3.1	1.7	2.8	55.4	1.3	39.7	13	1.9	12
octane	1.88	92.6	0.4	627	1.9	1.9	2.2	92.1	1.7	91.2	15	3.3	13
nonane	0.59	133	1.3	215	3.9	1.6	3.6	129	2.7	83.1	15	4.7	17
decane	0.195	164	0.4	103	4.8	1.7	5.0	159	2.9	92.4	20	7.2	2
undecane	0.055	197	0.1	61.4	6.2	2.1	4.2	205	3.5	61.9	22	12.7	22
dodecane	0.018	230	0.6	16.6	6.9	2.7	10.8	-[d]	-	-	-	-	-

[a] Average of n=10 analyses.

[b] Relative standard deviation (RSD), expressed as a percentage.

[c] Units for FID peak area are in pico-amp•sec, units for sensor peak area are in ΔR/R•sec•10^3

[d] C12 peak was not detected using µCR array; peak was indistinguishable from noise.

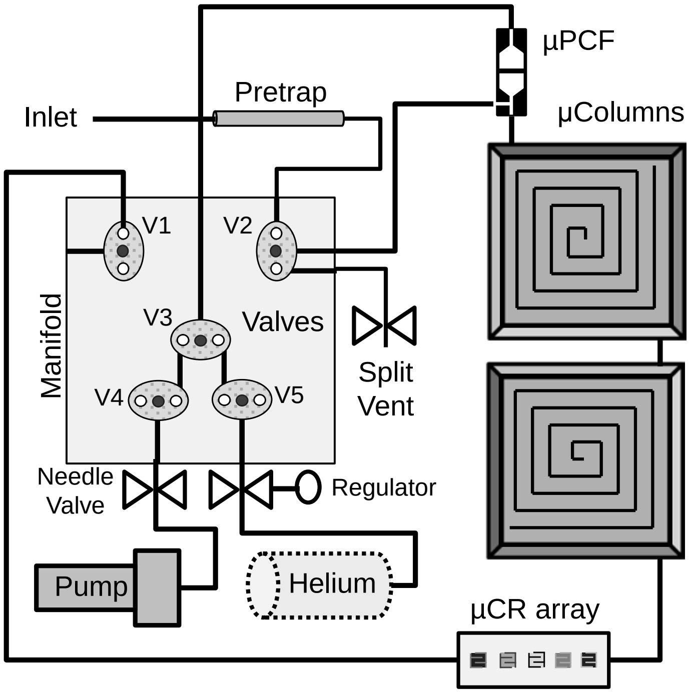

Figure 4.1 Layout diagram of Gen-1 PEMM. Samples are drawn in from the inlet by the pump. Low volatility interferences are captured on the pretrap, while target VOCs are captured on the dual stage µPCF. Valves 1, 2 and 3 are then thrown, passing helium carrier gas forward through the µPCF, which is rapidly heated to thermally desorb VOCs to the µcolumns. Detection is via the downstream µCR array. The injection split ratio is controlled via the needle valve connected to valve V2 and the separation flow rate is controlled via the regulator on the portable helium tank or conventional 110L helium cylinder.

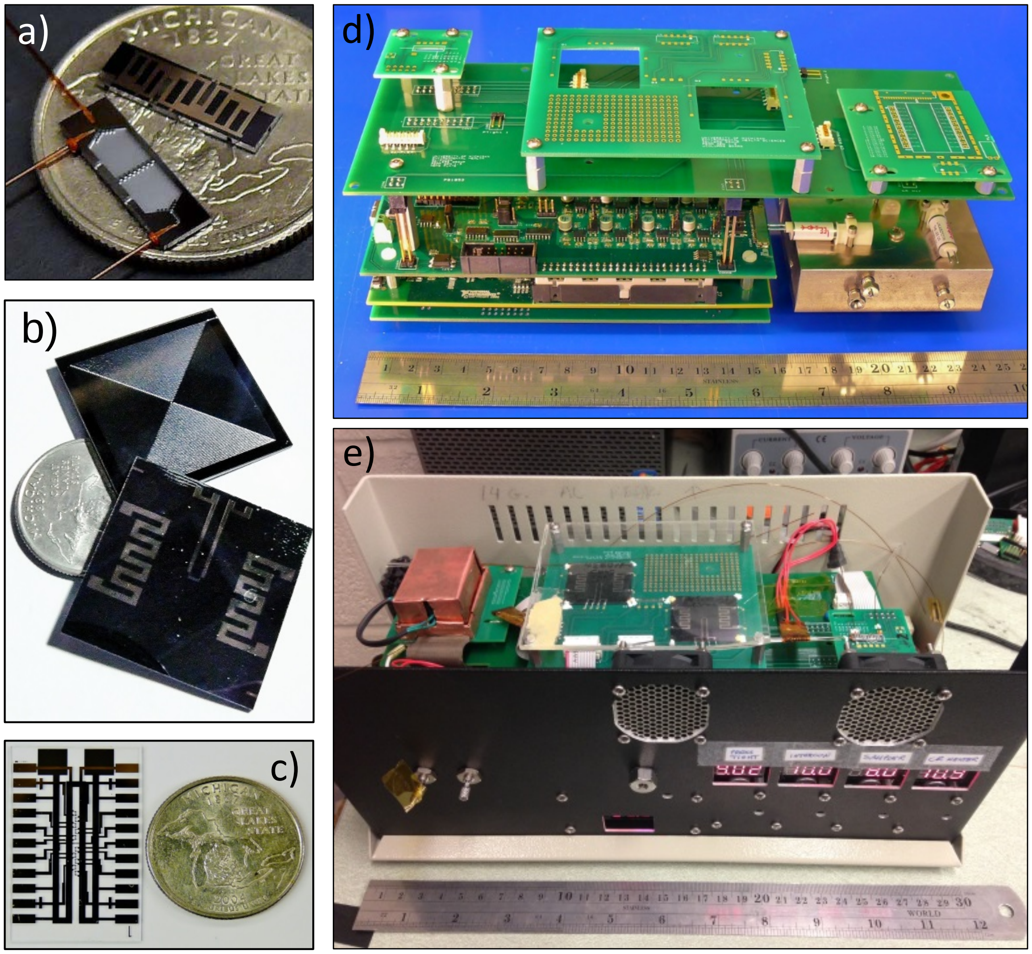

Figure 4.2. Photographs of the a) unfilled Gen-2 μPCF with Ti/Pt heater, fitted with capillaries; b) μcolumns, c) 10 sensor μCR array, with a resistive heater patterned on the backside, d) assembled electronics boards with manifold in place, and e) assembled system inside enclosure with lid removed.

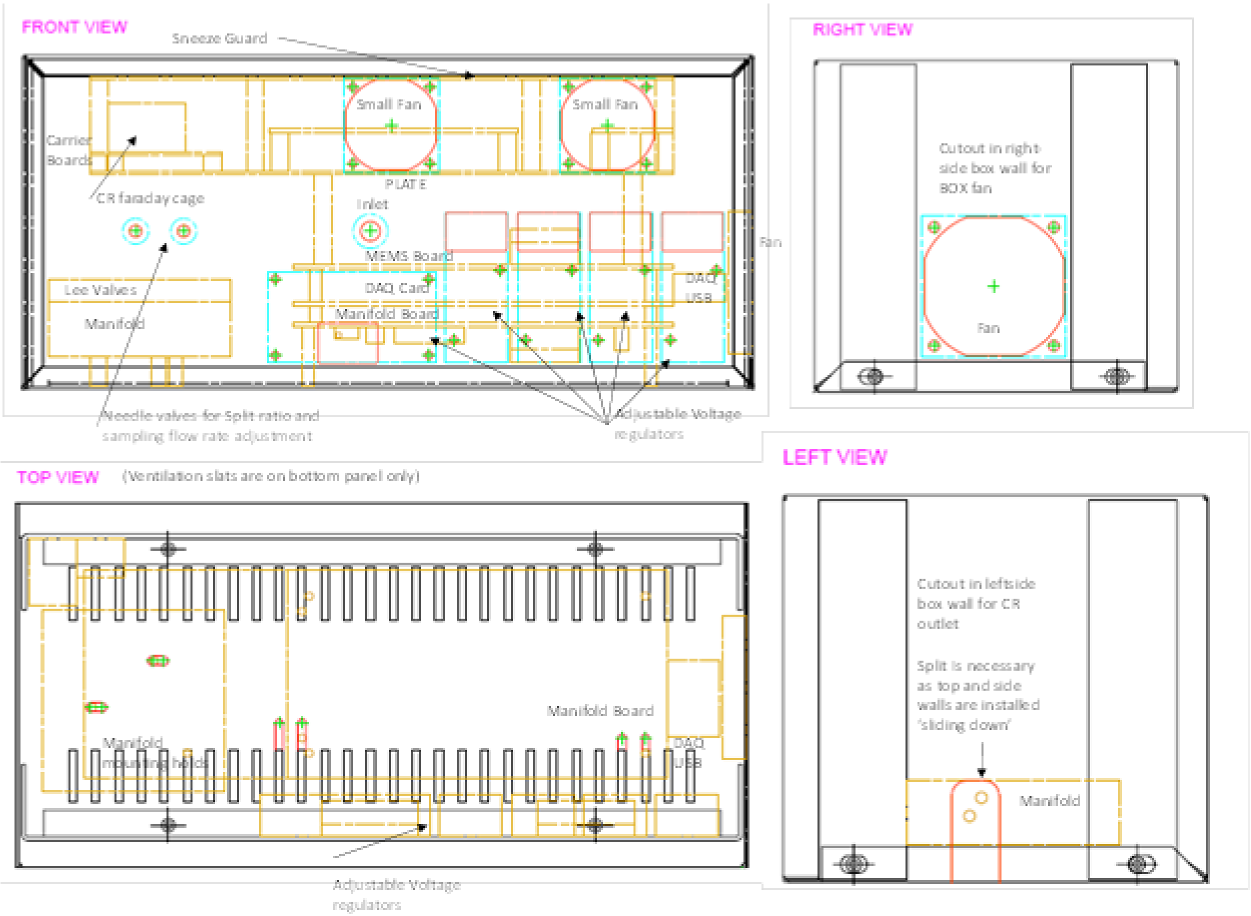

Figure 4.3. Engineering schematic of the layout of PEMM 1 prototype system, with electronic and fluidic components, as well as mounting holes, overlayed and labelled. Voltage regulators mounted onto front panel can be viewed and controlled from outside the enclosure. Needle valves are bulkhead mounted onto front panel for easy adjustment of split ratio and sampling flow rate. Fan on right panel operates continuously to cool electronic PCBs, while dual smaller fans at top of front panel operate post-analysis only to cool the µPCF and µcolumns, respectively. Effluent from the system exists the manifold from left panel, and can be plumbed to reference detector. Image courtesy of Nicolas Nuňovero.

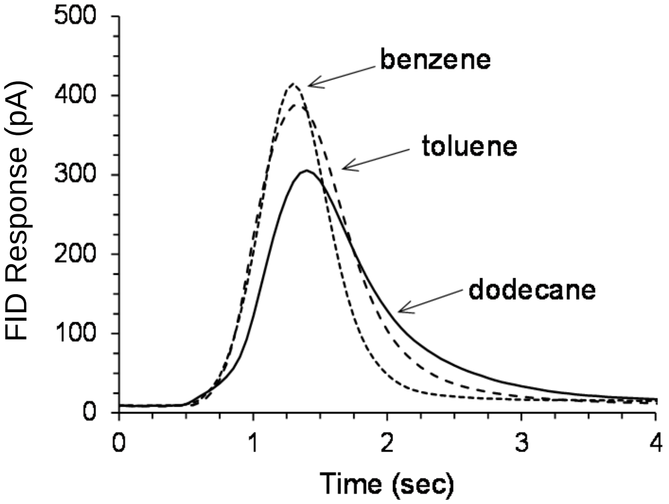

Figure 4.4 Example injection bandwidths of benzene, toluene, and n-dodecane from the Gen-2 μPCF, shown in Figure 4.2c, prior to integration into the full system. The device was positioned across a conventional GC gas sampling loop (see Figure 3.1). 0.5 μg of each vapor was loaded from single-vapor static test atmospheres, and thermally desorbed with a 2:1 split directly to the FID; analytical flow rate was maintained at 3 mL/min.

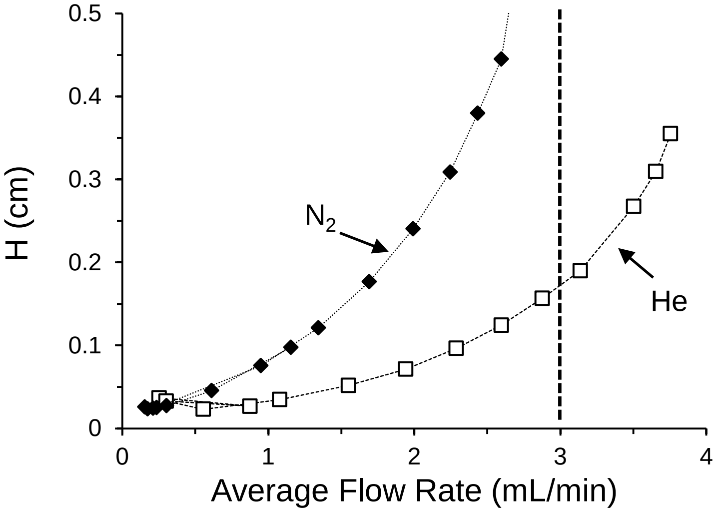

Figure 4.5 Modified Golay plot (using average flow rate instead of linear velocity) of PEMM 1 µcolumns, determined using a mixture of methane and n-octane in nitrogen and helium carrier gases. Gas-tight syringe injections and FID detection were used. Columns yielded 4300 plates/m with both carrier gases, with measured minimums at optimal flow rates of 0.17 and 0.56 mL/min, respectively, for nitrogen and helium. The vertical dashed line highlights system analytical flow rate of 3 mL/min.

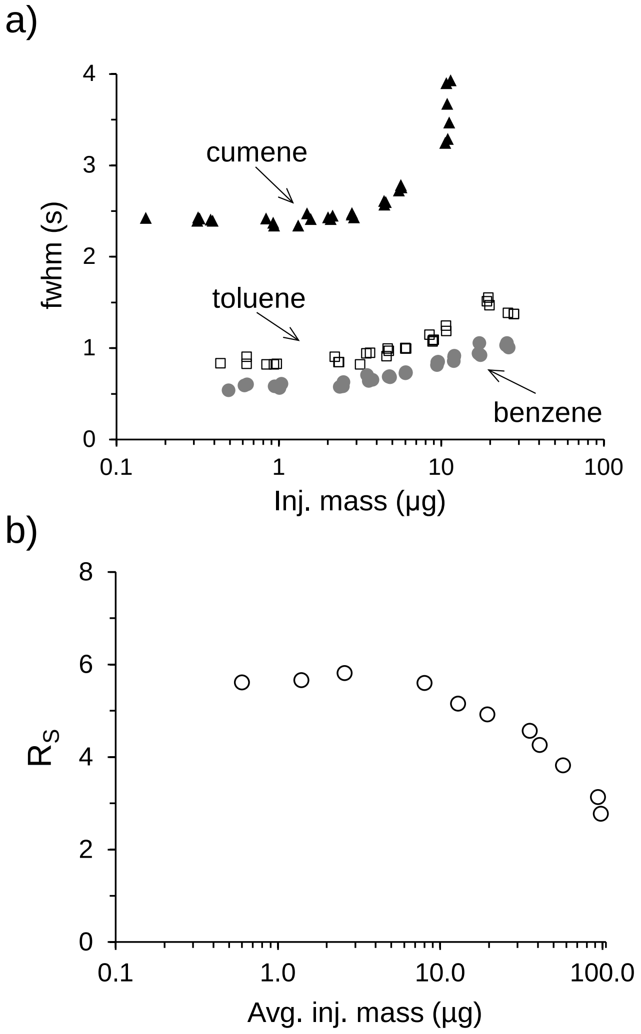

Figure 4.6 Effect of injected mass on chromatographic resolution on 6m µcolumn; a) effect of mass on *fwhm* for three target vapors, benzene, toluene and cumene, and b) effect of injected mass on chromatographic resolution of benzene and trichloroethylene. Mass in b) is the average mass of trichloroethylene and benzene in the injection, mixture was comprised of a 1.5:1 ratio, respectively, to account for difference in FID sensitivity (and maintain similar peak sizes).

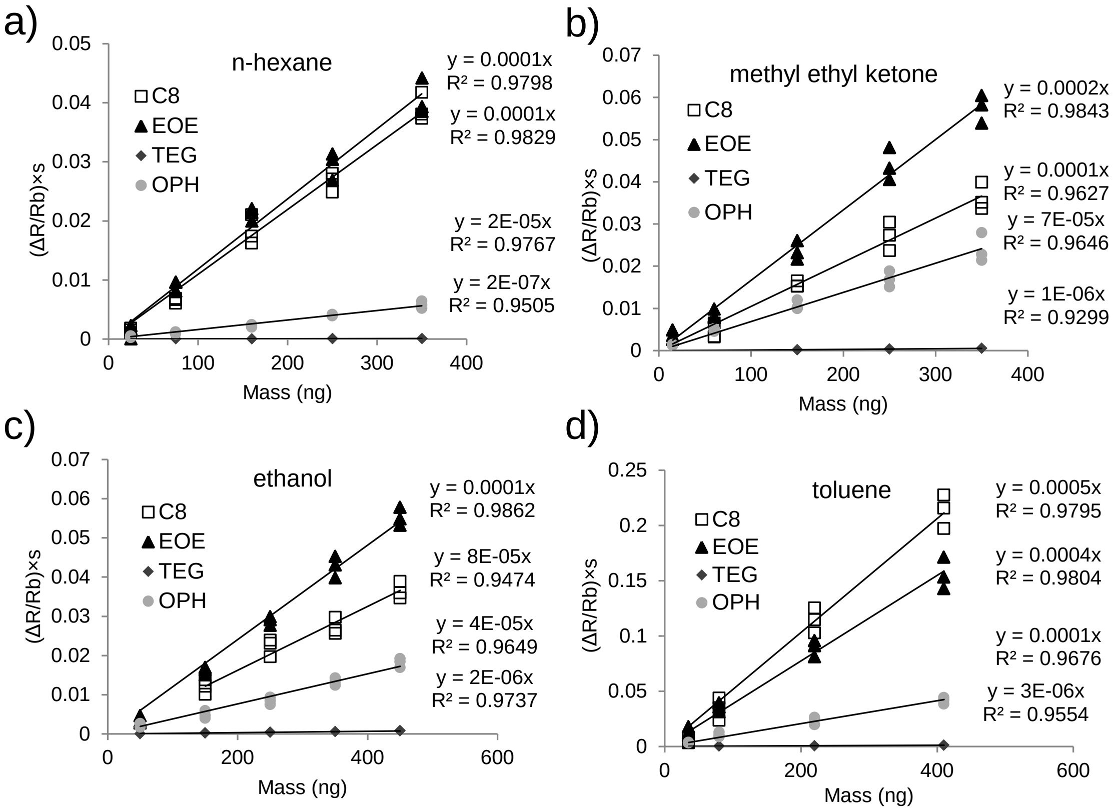

Figure 4.7 Calibration curves of 4-sensor Gen-2 μCR array (ID# CZ-01-044) with forced zero linear regression, from peak areas, a) n-hexane, b) ethanol, c) methyl ethyl ketone, and d) toluene. The μCR array was located downstream of a conventional GC column, operated isothermally at 35 °C, at 3.0 mL/min flow rate of helium. Three data points were collected at each concentration; masses of each verified by FID.

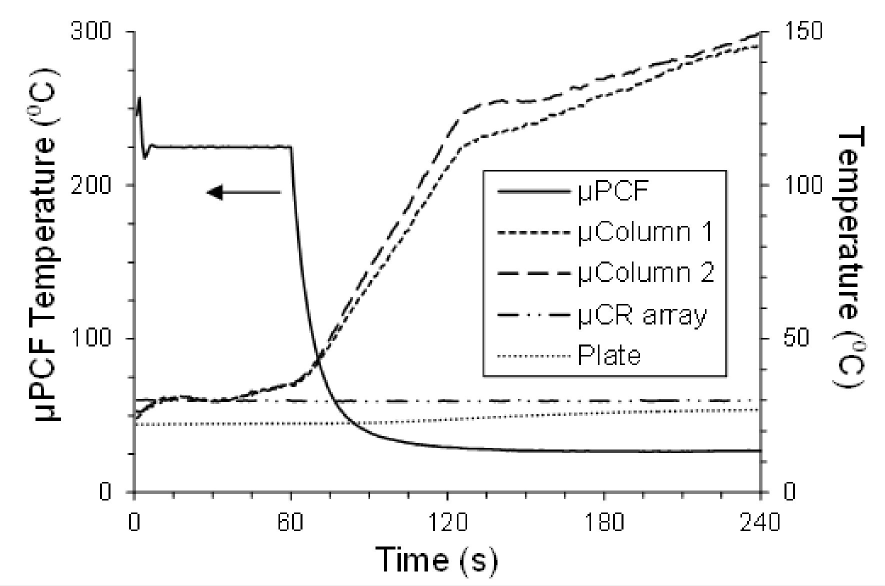

Figure 4.8 Example thermal cycle of the fully assembled Gen-1 PEMM with the system enclosed (lid closed), µPCF temperatures are references to the left hand vertical axis, and temperatures of the other components are referenced to the right hand vertical axis. The fluidic carrier “plate” thermistor was used to indicate ambient internal temperature of the system enclosure; all other measurements are taken directly from the fluidic component RTDs; µcolumn 1 was ramped at 5°C/min from an initial 30°C to 35°C (1 min), then AT 75° C/min to 110 °C (1 min), then AT 20°C/min to 150 °C (2 min), and µcolumn 2 was ramped at 5°C/min from an initial 30°C to 35°C (1 min), then 85° C/min to 125 °C (1 min), then 15°C/min to 150 °C (2 min).

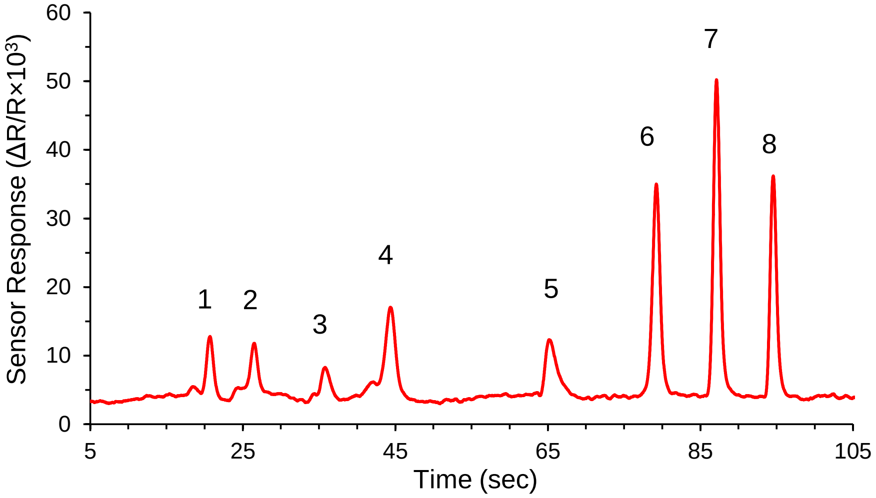

Figure 4.9 8-VOC chromatogram collected using PEMM 1 full system, with a single sensor array (ID# CZ-01-029). Static test atmosphere contained benzene (1), trichloroethylene (2), methyl isobutyl ketone (3), toluene (4), butyl acetate (5), ethyl benzene (6), o-xylene (7), and cumene (8). System conditions: 3 mL/min He carrier gas, μPCF ramp to 225 for 40 seconds, temp program 30 ^{0}C for 0.5 min, then 10 ^{0}C/min to 35 ^{0}C, then 70^{0}C/min to 70^{0}C, then 80 ^{0}C/min to 110^{0}C. μCR array held at 30°C. Only the OPH sensor trace is shown.

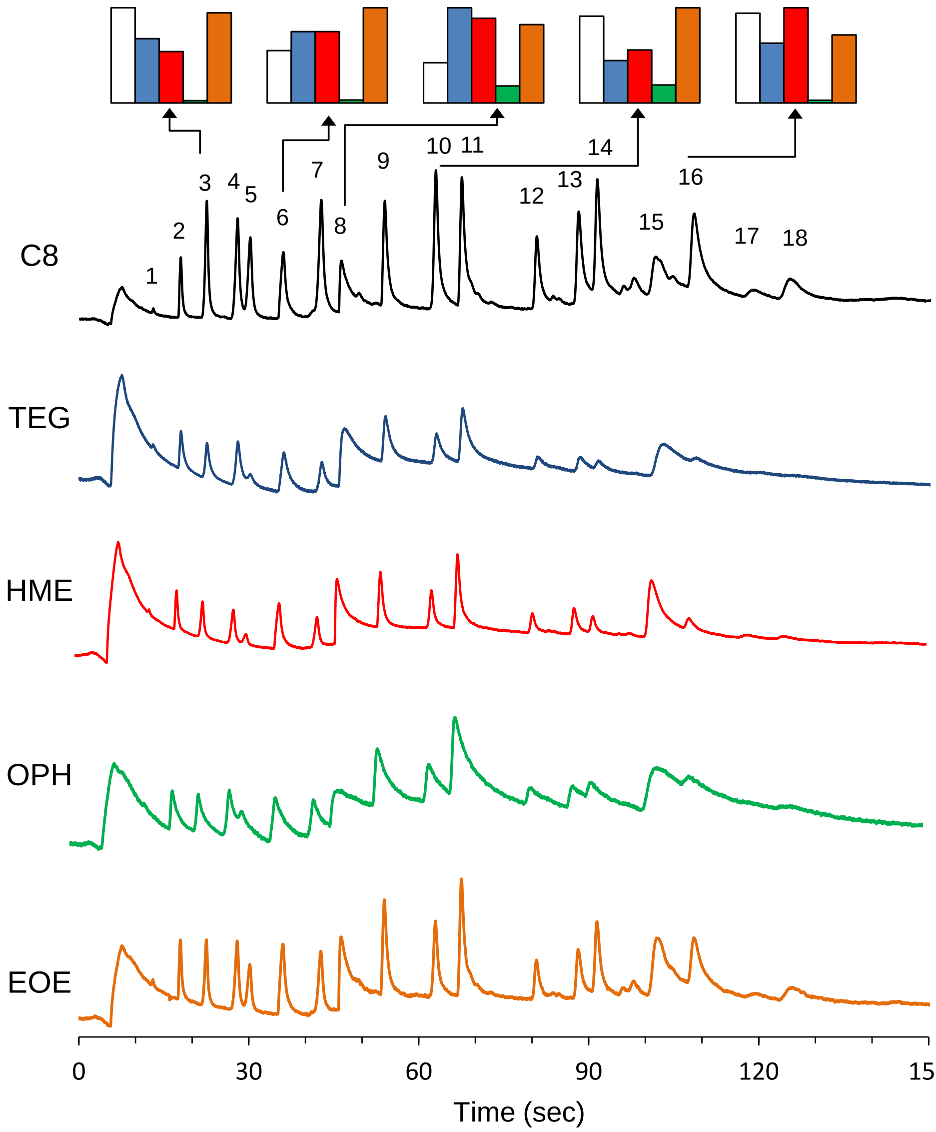

Figure 4.10 Separation of 18 compound mixture by the Gen-1 PEMM, with µPCF, µcolumns, and µCR array (ID# CZ-01-048). Conditions: 2:1 split injection, 3 mL/min analytical flow rate, columns held at 30°C for 30 seconds, then ramped 1°C/sec to 150°C, and held, µCR maintained at 30 °C. Peak identifications: dichloromethane, ethyl acetate, benzene, trichloroethylene, n-heptane, methyl isobutyl ketone, toluene, 1-pentanol, butyl acetate, ethyl benzene, 3-heptanone, n-propyl benzene, 1,2,4-trimethylenzene, n-decane, nitrobenzene, n-undecane, 1,2,4-trichlorobenzene, n-dodecane. Normalized response patterns, derived from peak heights, for six of the measured vapors are presented at the top of the figure, with sensors in order of C8, TEG, HME, OPH and EOE. Large first interference peak is attributed to water vapor. Normalized response patterns are taken from peak heights for five analytes spanning a range of polarities to highlight pattern differentiation.

Chapter 5

Conclusions

5.1 Summary

This dissertation has described several research projects relating to the development of a wearable μGC intended for routine personal monitoring of exposures to VOCs in the workplace. The broad goals were 1) to examine the improvement in identification and quantification of overlapping VOC peaks, detected by a chemiresistor sensor array used as a GC detector, achievable by multivariate curve resolution, specifically an algorithm employing evolving factor analysis and alternating least squares (EFA-ALS) to, 2) to optimize the performance of a Si-microfabricated preconcentrator/focuser device for selective preconcentration of VOCs with vapor pressures from 0.03-13 kPa at concentrations bracketing their occupational exposure limits, and 3) to design, assemble and characterize the Gen-1.5 personal exposure monitoring microsystem (PEMM) for quantitative analysis of moderately complex mixtures of VOCs.

5.2 Chemometrics for μCR arrays

In Chapter 2, the results of the EFA-ALS chemometric algorithm application were presented, and the methodology and performance were critically assessed. Chromatograms of three pairs of vapors, ranging in array response pattern similarity, were generated at different values of chromatographic resolution, R_s, and relative response ratio, *RRR*. One key finding of this study was that the composite responses were equivalent to the sums of the responses to the individual components, verifying that responses form the chemiresistor array were, in fact, additive. However, differences in peak asymmetry among the sensors in the array led to pattern distortions across the spans of all peaks. With data pre-processing to account for the latter, EFA correctly determined the chemical ranks of the binary composite peaks in 57 of the 63 cases (90%), with most errors observed for the most highly correlated pair. By using calibrated response patterns as inputs for the ALS refinements of EFA-extracted responses, the fidelity of recovered response patterns and elution profiles was sufficiently high to differentiate the composite peak components in 124 of 126 cases (98%) and to quantify them to within ±30% of actual values in 95 of 126 (75%) cases. Without such inputs, the corresponding rates were 112 of 126 (89%) and 68 of 126 (54%), respectively. In general, the *RRR* value was a more important determinant of performance than was the R_s value

Although the EFA-ALS algorithm was capable of determining the number of components, i.e. rank, in a composite peak in most cases in informed mode, the accuracy of extracted response patterns and quantification was poor in many cases. This suggested that the diversity afforded by the sensor array was only sufficient to differentiate compounds under certain circumstances, i.e. when the response patterns between two analytes differ greatly, the resolution, R_s, is moderate to high, or the relative response ratio close to unity. Errors in the rank determination were attributable to inability to distinguish a second chemical component from noise using eigenvector plots. Since the number of eigenvectors used for EFA in either direction, i.e. forward or backward, is equivalent to the number of sensors used, it is difficult to establish a clear noise threshold using a four channel detector. The identification of elution regions was not straightforward in part due to the tenuously established noise threshold, but also the differential tailing among sensors in the array, which exacerbated the problem by effectively changing the response patterns during elution. Including more sensors in the analysis, regardless of signal redundancy, would improve the ability to differentiate between noise and chemical components, provided peak asymmetry was consistent. By establishing a more robust variance threshold, chemical components would be easier to identify.

One of the limitations of this study was that all of the analyses considered were performed using a constrained library comprising only the two vapors of the given pair, i.e. each extracted pattern was compared to only the library patterns for the two vapors in that mixture. In cases where the composition of the binary mixture is not known a priori, limiting the library is not necessarily appropriate. Unfortunately, given the larger number of matching options and the generally poor quality of pattern extraction in blind mode, where extracted patterns are used for ALS instead of library patterns, errors in assigning identities are expected to increase.

Using EFA-ALS in informed mode, which entailed inputting calibration response patterns in lieu of EFA-extracted patterns for the ALS step, led to significant improvements in performance in both extracted pattern fidelity and quantification accuracy. To the extent feasible, this mode is highly recommended, however it necessarily requires *a priori* information on the composition of the mixture. Situations in which the identity of one vapor of a composite peak is known but the interfering vapor is unknown were not investigated; this does however represent the mostly likely scenario in which a chemometric method of this type would be used. Ultimately, constraining the library is an essential step in chemometric analysis, and is not unique this particular example.

Comparing the performance of the full 4 CR array with a 3 CR array, i.e. after removing the HME sensor signal from the data set, is was evident that omitting the data from tailing sensors improves the quality and accuracy of the EFA-ALS method. When analyzed by the full 4 sensor array, the tailing HME signal from NME was attributed to CHX, resulting in an extracted CHX pattern with high HME sensitivity. In contrast however, when using the 3 sensor array, CHX pattern recovery as quite good. This highlights the importance of examining the chromatographic data prior to chemometric analysis in order to identify and remove tailing traces. One alternative to eliminating tailing traces would be to include a 3rd component to the EFA-ALS analysis. The hypothesis here is that the first and second mathematical components would account for a single chemical component with the pattern drift, while the third mathematical component would account for the second chemical component. Unfortunately, due to the limited number of degrees of freedom inherent with a 4 sensor array, this approach is not feasible. The second alternative, and likely the best option, would be to include as many non-tailing sensors in the data set as possible.

One difficulty with sorptive transducer arrays was that the response patterns were not always consistent across multiple arrays, due to variations in the deposited film thickness and lack of film uniformity. These variations in pattern are likely attributable to the difficulty in generating reproducible drop-coated MPN films. Thus, unlike the known (and transferable) mass spectral libraries and thermal conductivities, libraries of CR array response patterns must be created individually for each new sensor array prior to use. This added step requires that operators be familiar with and capable of conducting instrument calibrations on a routine basis.

Ongoing work is aimed at further understanding, and attempting to resolve, some of the factors found to degrade performance, notably pattern drift, as well as incorporating more sophisticated constraints into the ALS algorithm so that the full value of microsensor array detection in μGC systems can be realized. Unfortunately, because pattern drift is quite possibly an inherent part of absorption-based transducers, a fixed-size moving window EFA (FSMW-EFA) algorithm, similar to that described in reference #1, may provide more accurate initial estimates of response patterns. In FSMW-EFA, the singular values are calculated from discrete portions, i.e. small time windows, of the chromatogram sequentially instead of building to include the entire chromatogram window. The rationale here is that the pattern drift, while significant over the course of an entire peak, occurs relatively slowly, and thus may be not be as problematic. Furthermore, including a unimodality constraint in the ALS algorithm for the concentration profiles would force all concentration profiles into peak-like shapes. This is an obvious constraint to apply to chromatographic applications since, under typical circumstances, all analytes will elute as single bands or zones, yielding unimodal peaks. Further constraining the concentration profiles to Gaussians could improve performance even further; however this would only be appropriate for sensors with relatively little peak asymmetry or tailing.

5.3 A microfabricated preconcentrator/focuser for a wearable μGC

In Chapter 3, a dual-adsorbent microfabricated preconcentrator/focuser (μPCF) device for selective exhaustive preconcentration and rapid thermal desorption (necessary for GC injectors) was developed. The approach entailed careful consideration of device-level and system-level factors, fluidic and thermal factors, and numerous application-specific variables in resolving the trade-offs in selectivity, capacity, desorption efficiency, and desorption bandwidth, which are the critical performance metrics. This study complemented others from our group on this topic by further elucidating and addressing the details of μPCF design and implementation in high-performance micro-analytical systems for VOC mixture determinations.

Here, delimiting the range of target compounds on the basis of volatility (i.e., p_v values from 0.03 to 13 kPa) was rationalized on practical and fundamental grounds. IT is a common, if not requisite, feature of fieldable μGC instrumentation; inherent constraints on the complexity of mixtures that can be analyzed by such instrumentation demand such concessions. Delimiting the concentration range for any specific VOC in terms of its ACGIH TLV value (i.e., 0.1 to 2×TLV) was also rationalized on practical grounds, though proved difficult to implement because it translated into a concentration range > 10^4 when all target compounds were considered collectively. Increasing the complexity of a mixture, i.e. analyzing samples with a greater numer of analytes, has a similar effect on the total mass loading of the μPCF. These scenarios will likely demand the designation of two operating modes for the μGC, which would differ in sample volume and by the split ratio of the injection. This compromise points to an inherent limitation in this technology. For example, a mixture with high complexity would require the use of the split injection mode in order maximize separation performance. On the other hand, a mixture with low concentrations would be better analyzed with splitless injection, i.e. without bleeding off captured vapors, so as to maintain low LODs. However, for a mixture with both high complexity and low concentrations, a compromise is required as neither operational mode can, by design, provide both the best separation performance and lowest LODs in a single analysis. Similarly, one can envision a mixture where the target vapor is at low concentration but interfering vapors are at high concentration, a situation that would require a similar compromise. Ultimately, since certain possible exposure scenarios may not fall within either of the two aforementioned categories, a compromise that emphasizes either separation performance or LODs must be made.

Results from this study were used to establish bed volumes for the second generation μPCF devices used in Chapter 4. These Gen-2 devices will be incorporated into both the Gen-2 PEMM as well as another 2 dimensional gas chromatograph microsystem currently under development in our laboratory. Both of these instruments rely on sharp injection bands for performance, as such future work will seek to evaluate and optimize their injection performance specifically.

5.4 Development of the personal exposure monitoring microsystem μGC

Chapter 4 of this thesis presented the development of the Gen-1.5 laboratory prototype personal exposure monitoring microsystem (PEMM) μGC. Each of the fluidic components was characterized individually, after which performance of the full prototype was demonstrated. Injection bands from the μPCF devices with patterned heaters were sharper and more symmetric than those from the bulk heated μPCF presented in Chapter 3, despite being 24% larger. This is likely due to the design of the heater, which was optimized by members of the Kurabayashi research group to reduce thermal gradients (cold spots) on the chip and maximum the rate of heating during initial ramping. Capacity was not evaluated for this new component, however adsorbent masses and chamber designs are larger than those evaluated in Chapter 3, as such it was expected that results would be very similar.

The separation performance of the μcolumns was evaluated with respect to carrier gas (He vs. N2) by comparing the resolution of critical pairs of vapors analyzed under the same conditions (flow rate, temperature program). Using the μPCF highlighted that incorporating He yielded a significant improvement over N_2 for TCE and benzene. Early eluting compounds were used here as they are more sensitive to injection bandwidth and carrier gas selection due to short residence times on column.

The effect of injected mass on chromatographic performance was also evaluated. The dynamic range of the separation columns was evaluated to identify the point at which chromatographic performance decreased due to overloading of the stationary phase. Here, FWHM was shown to be independent of injected mass up to 2-3 μg, beyond which peak areas broaden significantly. For high-concentration samples, it is imperative that single analyte mass loadings do not exceed this threshold, or chromatographic performance will drop sharply.

When considering the PEMM system, reconciling the dynamic ranges of each fluidic component was identified early on as one of the most significant challenges. Each fluidic component has a limited range of analyte masses/concentrations over which performance is optimized. At a basic level, injected masses of each target should ideally lie above the μCR array LOD and below the 2-3 μg chromatographic resolution threshold in order to maintain accurate identification and quantification, and permit chemometric analysis. In practice, however, the effective dynamic range hinges on several other factors. Firstly, it is important to consider the dynamic range of the sensors comprising the μCR array, which was not sufficiently characterized in Chapter 4, however remains an important topic of discussion here. Optimizing the preparation of these sensor devices is necessary prior to this evaluations of this kind, however, as inter- and intra- device variations remain large (as discussed above). Furthermore, considering that the dynamic ranges of each sensor spans roughly the same fold-range just at different lower and upper bounds, it is possible to widen the effective array range if an abbreviated sensor is used, i.e. discarding the least or most sensitive sensor in the array. This would, however, eliminate some of the potential for vapor recognition by MCR analysis.

Secondly, the capacity of each of the two adsorbent beds of the μPCF must be considered with respect to vapor pressure and mass loading. In Chapter 3, limits were empirically determined under mixture conditions, yielding conservative maximum sampling volumes of 10 mL for benzene and toluene at worst case scenario high concentration conditions, i.e. 200 ppm each of four vapors. Benzene and toluene are, of course, the sentinel vapors. Targets with lower vapor pressures, e.g. n-nonane, n-decane, or compounds of similar volatility, are expected to have greater permissible sampled volumes given their affinity for Carbopack B.

Ultimately, it is crucial that the exposure scenario mixture be thoroughly characterized prior to investigation with the PEMM system (as is the case for nearly all similar instruments) so that conditions of analysis can be optimized. The composition of any mixture and the initial estimates of the concentrations of all analytes must be known a priori, or quantitative analysis by the PEMM system may not be possible. This information as it allows the sensor arrays to be calibrated and response pattern libraries must be constructed, and also for injection and chromatographic conditions to be set to optimize performance, emphasizing resolution or LOD, or a specific compromise of both. Exposure dynamics can be captured provided that the concentration of each analyte does not fall below or exceed the established limits, including breaking through the μPCF and/or falling outside the dynamic range of the sensors. Thus, while relatively simple to operate, the PEMM would still require a dedicated well-trained operator, as development and implementation of such novel methods requires a great deal of intuition and experience.

5.5 References

[1] A. de Juan, M. Maeder, T. Hencewics, R. Tauler, Local rank analysis for exploratory spectroscopic image analysis fixed size image window-evolving factor analysis, *Chemometrics and Intelligent Laboratory Systems*, 77, 64-74, 2005.